TÉCNICO LISBOA

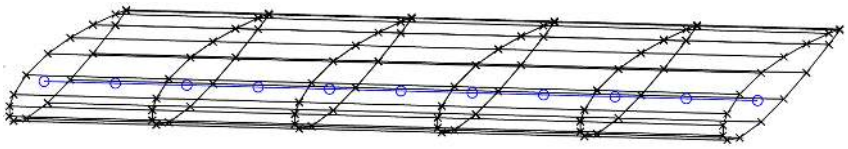

Structural Dynamics for Aeroelastic Analysis

João Daniel dos Santos Almeida

Thesis to obtain the Master of Science Degree in

Aerospace Engineering

Supervisor: Prof. André Calado Marta

Examination Committee

Chairperson: Prof. Filipe Szolnoky Ramos Pinto Cunha
Supervisor: Prof. André Calado Marta
Member of the Committee: Dr. Frederico José Prata Rente Reis Afonso

November 2015

Dedicated to my family

Acknowledgments

I would like to thank my supervisor, Professor André Marta, for his dedication and willingness to help and guide me through this task. His counsel and knowledge were crucial factors to finish this project and he was an overall excellent supervisor. I want to thank my colleagues, especially my closest friends who accompanied me throughout the last five years of completing my degree for their true friendship. I would also like to thank my family for their love and unconditional support, which have sustained and encouraged me during the elaboration of this thesis.

Resumo

Aeroelasticidade é um fenómeno físico que resulta da interacção entre forças aerodinâmicas, elásticas e inerciais. Torna-se importante estudá-la em estruturas aeroespaciais, devido ao seu design leve e flexível.

O presente trabalho tem como objectivo estudar o comportamento aeroelástico de uma asa 3D. Para isso, esta é modelada como viga usando o método dos elementos finitos. A viga unidimensional coincide com o eixo elástico da asa e contém toda a sua rigidez ao longo do seu comprimento. Assim, uma nova rotina computacional é criada utilizando o modelo estrutural desenvolvido e integrando um programa disponível de análise aerodinâmica, que faz uso do método dos panéis. Ambos os modelos computacionais são validados através de resultados publicados. O acoplamento dos dois domínios é feito usando um esquema de discretização temporal adequado, que é escolhido após serem realizadas uma série de análises computacionais com esquemas temporais diferentes. A rotina computacional é comparada com resultados estáticos provenientes de um modelo de asa.

Os resultados apresentam-se para uma asa denominada o caso referência. É conduzido um estudo paramétrico, cujos resultados são comparados com os valores de referência. Conclui-se que a rotina revela bons resultados, tendo em conta as espectativas teóricas. Além disso, uma rotina de optimização aero-estrutural foi desenvolvida com o objectivo de minimizar a massa total da asa e mantendo constante o coeficiente de sustentação. Apesar das muitas simplificações efectuadas, tanto a nível estrutural como aerodinâmico, a rotina computacional criada revela ser útil na previsão do desempenho aeroelástico de uma asa nas etapas iniciais de projecto de aeronaves.

Palavras-chave: Aeroelasticidade, Método dos panéis, Método dos elementos finitos, Interacção fluído-estrutura, Métodos de acoplamento, Flutter

Abstract

Aeroelasticity is a physical phenomenon resulting from the interaction of aerodynamic, elastic and inertial forces. It is very important to study aeroelasticity in aircraft structures, due to their lightweight and flexible design.

The present work aims to study the aeroelastic behavior of a 3D aircraft wing. For that, a beam representation of the wing structure is developed using the finite-element method. The one-dimensional beam coincides with the wing elastic axis with the whole rigidity of the wing concentrated along it. Therefore, a new computational aeroelasticity framework was created using the structural model developed and integrating an available fluid solver, which uses a panel method to solve the fluid flow. Both the fluid and structural solvers are validated with published results. The coupling of the two domains is made using an adequate time discretization scheme, which is chosen after performing several analyses using different temporal schemes. The framework is validated with available trim results from a wing model.

The results are then presented for a wing denoted as reference case. A parametric study is conducted and its results compared with the reference values. It is concluded that the results show very good agreement with the theoretical expectations. Moreover, an aero-structural optimization of a wing is tackled aiming to minimize its total mass while fixing the lift coefficient. Despite the many simplifications implemented in both the fluid and structural solvers, this framework proves to be useful to predict the aeroelastic performance of a wing in the early stages of aircraft design.

Keywords: Aeroelasticity, Panel method, Finite element method, Fluid-structure interaction, Coupling schemes, Flutter

Contents

List of Tables

List of Figures

Nomenclature

Greek symbols

α	Angle of attack, Newmark integration parameter.
Δ	Variation.
δ	Newmark integration parameter, Logarithmic decrement.
ϵ	Elastic strain vector.
Γ	Dihedral angle.
κ	Thermal conductivity coefficient.
Λ	Sweep angle.
λ	Taper ratio.
μ	Doublet strength.
ν	Poisson ratio.
ω	Natural frequency.
Φ	Velocity potential.
ρ	Density.
σ	Stress vector.
τ	Stress tensor.
θ	Structural torsional angle.
ζ	Damping ratio.

Roman symbols

B	Strain-displacement matrix.
c	Airfoil‘s chord.
C_D	Coefficient of drag.

C_L	Coefficient of lift.
$C_{L,0}$	Coefficient of lift at zero angle of attack.
C_M	Coefficient of pitching moment.
C_p	Pressure coefficient.
$\vec{d}$	Nodal displacements vector.
D	Elastic stiffness matrix.
E	Young‘s modulus, Potential function.
EA	Axial stiffness.
ec	Distance between aerodynamic and elastic center.
EI_{yy}	Flapwise bending stiffness.
EI_{zz}	Chordwise bending stiffness.
$\vec{F}$	Nodal forces vector.
G	Shear modulus.
GJ	Torsional stiffness.
K	Structural stiffness matrix.
L	Lift force.
M	Structural mass matrix.
M_0	Wing pitching moment.
N	Shape functions matrix.
p	Pressure.
$\dot{q}$	Rate of volumetric heat addition per unit mass.
Q_i	Generalized applied forces.
R	Specific gas constant.
S	Area of cross-section.
Δt	Time step size.
T	Kinetic energy, Temperature.
t	Time, Thickness
T_R	Transformation matrix.

u, v, w Velocity Cartesian components.

$\vec{u}$ Structural displacement vector.

$\dot{\vec{u}}$ Structural velocity vector.

$\ddot{\vec{u}}$ Structural acceleration vector.

$\vec{V}$ Fluid velocity vector.

V Potential energy.

$\vec{W}$ Fluid state vector.

Subscripts

∞ Free-stream condition.

av Average value.

k Panel number.

L Lower side.

n Normal component, Vibration cycle.

$pretwist$ Refers to pretwist angle.

$skin$ Refers to wing skin.

$spar$ Refers to wing spar.

tip Refers to wing tip.

U Upper side.

w Wake.

x, y, z Cartesian components.

ref Reference condition.

Superscripts

T Transpose.

t Time step.

Glossary

BSFT Bredt-Batho Shear Flow Theory is a mathematical method used to compute stresses and deformations in structures with closed thin-walled cross-section under torsion.

CFD Computational Fluid Dynamics is a branch of fluid mechanics that uses numerical methods to solve problems that involve fluid flows.

CSD Computational Structural Dynamics is a branch of structure mechanics that uses numerical methods to perform the analysis of structures in time.

CSS/ISS Conventional/Improved Serial Staggered schemes are two procedures for fluid-structure coupling.

FEM Finite Element Method is a numerical technique for finding approximate solutions to boundary value problems for partial differential equations.

HALE High-altitude long-endurance unmanned aerial vehicle, an UAV with a high-aspect ratio wing with the purpose of providing in flight data about aeroelasticity.

NACA National Advisory Committee for Aeronautics, under which series of airfoil shapes are developed.

NASA National Aeronautics and Space Administration is the United States government body responsible for the aeronautics and astronautics research programs.

NS Navier-Stokes flow governing equations.

UAV Unmanned Aerial Vehicle, commonly known as a drone and also referred to as RPV, is an aircraft without a human pilot aboard.

Chapter 1

Introduction

1.1 Motivation

The science of aeroelasticity is of the most importance in aircraft design. As it will be explained later, aeroelasticity comprises physical phenomena, occurring on aircraft structures, resulting from the interaction of aerodynamic, elastic and inertial forces acting on them.

These effects occur in many types of structures, such as bridges and buildings in free airflow. For aircraft though, it is extremely important to achieve aeroelastic stability due to its extremely lightweight design resulting in flexible structures. As a consequence, aeroelastic oscillations and deformations, if not controlled, can cause severe damage to the aircraft, possibly resulting in catastrophic accidents.

Nowadays, in order to prevent the negative consequences of aeroelasticity and to better understand and control it, several computational aeroelastic tests can be performed in early stages of aircraft design, posing as efficient and accurate methods and thus lowering the number of experimental tests needed.

1.2 Historical Perspective

In the early days of aviation, even before the Wright brothers‘ first flight, Professor Samuel Langley, at the Smithsonian Institute, unsuccessfully attempted powered flight in his monoplane, which crashed into the Potomac river, as shown in Figure 1.1(a). This has become one of the first known aeroelastic problems that occurred in aviation. According to Garrick and Reed III [1], the wing collapsed because of the excessive wing twist caused by high wing camber coupled with low torsional stiffness, which resulted in structural failure. This problem was mitigated with the development of biplanes over the next years. The success of the Wright Flyer in late 1903, for example, is due to a consideration of aeroelastic effects. The Wright brothers developed a wing warping mechanism for lateral control [2], allowing controllability without the need to alter the local wing camber. Moreover, the brothers corrected the efficiency of the propeller blades with backward sweep after recognizing an adverse aeroelastic effect [3]. Biplane designs were dominant for 30 years until the advent of semi-monocoque structures [2].

As stated by Kehoe [4], the first recorded flutter incident was achieved when troubleshooting violent

oscillations occurred on the horizontal tail of the Handley Page 0/400 bomber, as shown in Figure 1.1(b), at the beginning of World War I. Also, control surface flutter began to appear during that time. The plane experienced violent in-flight asymmetric torsional oscillation of the fuselage and pitch oscillation due to a lack of torsional stiffness [1, 2]. It was discovered that the oscillations were self-excited by an interaction with airflow, and not due to any resonance of vibration sources [1].

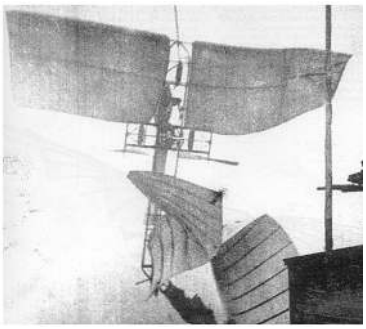

(a) Langley Flyer

(b) Handley Page 0/400 bomber

Figure 1.1: Early aircraft aeroelastic incidents [1].

These two historical failure cases are indicative of the two main aeroelastic problems: *static aeroelasticity* and *dynamic aeroelasticity*. These problems will be presented in the next chapter.

New flutter incidences emerged when aircraft could fly with transonic speeds. According to Kehoe [4], from 1947 to 1956, there were 21 incidences of flutter involving transonic aircraft. Nowadays, supersonic speeds produced a new type of flutter known as panel flutter, which involves constant amplitude standing in aircraft skin coverings that can lead to fatigue failure [4].

In order to study and prevent flutter, flight flutter test techniques were developed including structural excitation systems, instrumentation systems and signal preprocessing. The first formal flight flutter test was conducted in Germany in 1935, by Von Schlippe [4]. It consisted of structural excitation using a rotating unbalanced weight, measuring the response amplitude and recording it as a function of airspeed.

Over the next years, there were advances in the aerodynamic and structural fields and several computational aeroelastic models were developed. The computer revolution brought new numerical methods such as panel methods and finite element analysis. The latter has become an important method in design and optimization of structures in the field of aeroelasticity.

With the development of Unmanned Aerial Vehicles (UAVs) in the recent years, some of them were built with the purpose of collecting data of the aeroelastic response in-flight. NASA‘s Helios prototype, which is shown in Figure 1.2, and the X-HALE from the University of Michigan are two examples [5]. These are modern High-Altitude Long-Endurance (HALE) aircraft with a very lightweight and flexible design whose wings may undergo large deformations during normal operating loads.

1.3 Objectives

The initial purpose of this thesis is to study the governing equations of aeroelasticity and review some of the models and methods currently used in aeroelastic calculations. Two main objectives support this

Figure 1.2: Helios aircraft showing large wing deflection [6].

thesis. The first main objective is to develop a dynamic structural model for the wing, representing it as an equivalent beam, in order to be used in an aeroelastic framework, applying the finite-element method and taking into account the mass and stiffness matrices of the system. Moreover, an existing computational fluid solver will be adapted and integrated in this work. Therefore, a finite element code was developed to describe an equivalent wing beam model, which can be used in the early stages of aircraft design.

The second main objective is to benchmark and study several implemented coupling methods, which are used to couple the fluid and structural domains, concluding about the accuracy, stability and efficiency of those methods.

In general, Figure 1.3 illustrates the major steps conducted in this thesis. The dashed boxes represent work already done, which was used here. On the other hand, the solid boxes are related to code developed from scratch, which constitutes the bulk of this work.

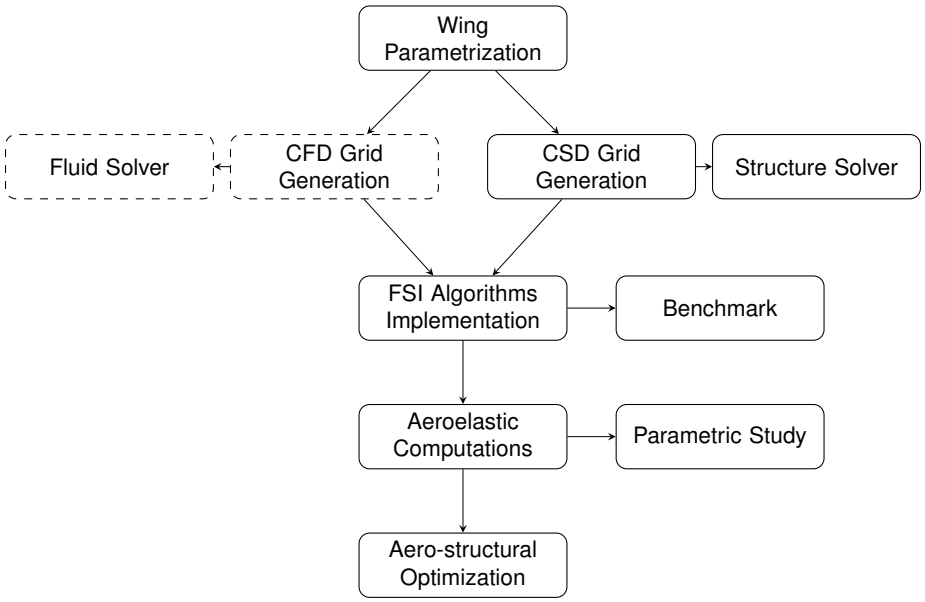

Figure 1.3: Flowchart illustrating the steps undertaken in this thesis. Dashed boxes represent work already available. Solid boxes constitute the bulk of this work and are related to code developed from scratch.

1.4 Thesis Outline

This work is divided into chapters, with a logical sequence ranging from the basic principles of aeroelasticity, through the development and implementation of the computational tool, including an overview and application of several coupling methods and concluding with the application of the aeroelastic framework developed to several case studies, including a parametric study and a aero-structural optimization problem.

Chapter 2 presents the subject of aeroelasticity, including definitions of static and dynamic aeroelasticity as well as the mathematical formulation.

In Chapter 3, the computational aerodynamic tool will be selected and explained. The chapter begins with a theoretical introduction on the basics of fluid dynamics and the potential fluid flow theory, applied in the computational model. Furthermore, the numerical method applied is presented and its numerical implementation is summarized.

Chapter 4 presents the theory of the finite-element method using beam elements, which is the basis of the dynamic structural model. Moreover, the development stages before arriving at the final model are addressed, as one will enter into the practical development of the program with a description of each step that was carried out. The chapter ends with a verification and validation of the code, through several analysis conducted both with the developed program and with a commercial software.

In Chapter 5, the input parameters are specified in order to parametrize the aircraft wing, namely, the coordinate systems, the wing geometry, the material properties and the internal structure. Furthermore, the mathematical method used to compute structural properties of a plane section of the wing is reviewed.

Chapter 6 results from a literature review about fluid-structure coupling methods, presenting several coupling methods with possible enhancements. Moreover, the spatial discretization of the aircraft wing is detailed, giving special attention to the transferring of the aerodynamic forces into the structural nodes and the procedure to move the fluid and structural grids is also explained and validated.

The numerical results start in Chapter 7, where several tests are performed with a reference case wing in order to test the influence of the coupling procedures presented in the previous chapter on the results. Chapter 8 continues this trend with a parametric study, where several additional analysis are performed having chosen the best coupling procedure and varying the input parameters from Chapter 5, comparing the results with the reference case.

Finally, Chapter 9 deals with a simple aero-structural optimization of a subsonic wing. A brief explanation is made about the optimization problem and a commercial tool is selected, ending with a description of the final results.

The thesis ends with a summary of achievements and suggestions of future work in Chapter 10.

Chapter 2

Static and Dynamic Aeroelasticity

In this chapter, special cases of aeroelastic problems will be presented, namely static and dynamic problems. According to Megson [7], the first may exhibit divergent tendencies leading to failure or, in a sufficient stiff structure, convergence until a condition of stable equilibrium is achieved. Those aeroelastic phenomena are known as *static divergence* and *control reversal*. On the other hand, dynamic aeroelastic problems occur due to dynamic loading systems that induce oscillations of structural members, which may end up causing failure. In this group are, for example, *flutter*, *buffeting* and *dynamic response*.

2.1 Aeroelasticity Background

According to Clark *et al.* [8], aeroelasticity can be defined in the following manner:

"Aeroelasticity is concerned with those physical phenomena which involve significant mutual interaction among inertial, elastic and aerodynamic forces".

To better understand and visualize the context of aeroelasticity, Collar [9] proposed a triangle of those disciplines, presented in Figure 2.1.

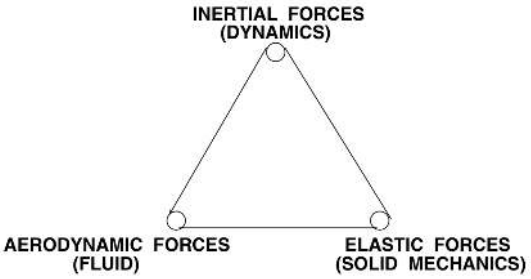

Figure 2.1: Collar diagram, adapted from [8].

This triangle represents the three main disciplines directly related to dynamic aeroelasticity. By pairing two corners of the triangle, one can identify other important technical fields posing as special aspects of aeroelasticity. For instance:

- *Stability and control (flight mechanics)* = inertial forces + aerodynamic forces;

- *Structural vibrations* = inertial forces + elastic forces;
- *Static aeroelasticity* = aerodynamic forces + elastic forces.

2.2 Static Aeroelastic Problems

Static or steady state aeroelastic problems involve the interaction of aerodynamic and elastic forces. In fact, as the wing is flexible, loads cause distortion. Consequently, as the wing incidence angle is being changed, a redistribution of aerodynamic loads is also occurring. Assuming the centre of twist is behind the aerodynamic centre, the moment caused by lift force in relation to the twist center gradually increases as long as the wing incidence also increases, because a change in lift is proportional to a change in wing incidence. Figure 2.2 illustrates this phenomena.

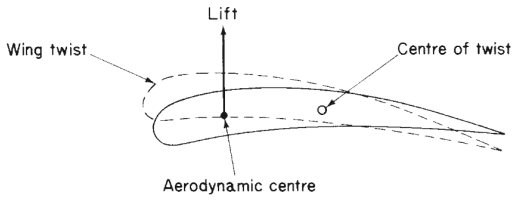

Figure 2.2: Aerodynamic loads causing wing twist, increasing wing incidence [7].

If a condition of stable equilibrium is achieved, the torsional moment of aerodynamic forces balances the torsional rigidity of the wing. That state is reached if the air speed does not surpass a critical value, that is, the *divergence speed* [7].

Other important aeroelastic static problem is the *control effectiveness and reversal*. Like the wing, vertical and horizontal tails are flexible structures, which can adversely affect the effectiveness of their control surfaces. Taking in the example of an aileron, the downward deflection causes a change in lift distribution which makes the wing twist nose down. This phenomena reduces the incidence of the aileron, thus reducing the increase in lift produced by the aileron deflection and, consequently, the rolling moment of the aircraft. There is a critical airspeed, the *aileron reversal speed* [7], at which the effectiveness of the control surface is completely nullified and does not produce any rolling moment. Because of this, above this critical speed, to have a positive increment of lift, an upward aileron deflection is necessary.

The most common divergence problem is the torsional divergence of a wing [7]. Therefore, in the following section, the mathematical formulation of this problem will be presented. The simplest case of a 2D wing is considered. As illustrated in Figure 2.3, one will consider a 2D wing with cross-section area *S*, chord *c* and torsional stiffness *K* who is subject to aerodynamic loads as lift *L* and wing pitching moment M_0 relative to the aerodynamic center [7].

For the wing to be in equilibrium, the moment produced by aerodynamic loads about the elastic center shall be balanced by the torsional moment of the wing. Therefore, the moment equilibrium equation is then

$$M_0 + Lec = K\theta\,, \tag{2.1}$$

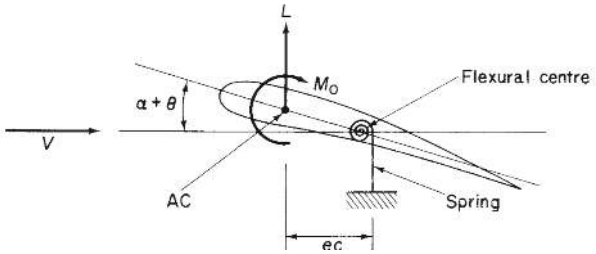

Figure 2.3: Representative system of a 2D wing in torsion [7].

where *ec* is the distance between the aerodynamic and elastic centers of the wing and θ is the elastic twist of the wing. From steady aerodynamics,

$$L = \frac{1}{2}\rho V^2 S C_L \,, \tag{2.2}$$

$$M_0 = \frac{1}{2}\rho V^2 S c C_{M,0} \,, \tag{2.3}$$

$$C_L = C_{L,0} + \frac{\partial C_L}{\partial \alpha}(\alpha + \theta) \,. \tag{2.4}$$

In which α is the initial angle of attack of the wing, $C_{L,0}$ is the wing lift coefficient at zero angle of attack and $\frac{\partial C_L}{\partial \alpha}$ is the wing lift curve slope. Substituting in Eq. (2.1), one obtains

$$\frac{1}{2}\rho V^2 S[cC_{M,0} + ecC_{L,0} + ec\frac{\partial C_L}{\partial \alpha}(\alpha + \theta)] = K\theta \,. \tag{2.5}$$

The angle of twist is then given by

$$\theta = \frac{\frac{1}{2}\rho V^2 Sc(C_{M,0} + eC_{L,0} + e\frac{\partial C_L}{\partial \alpha}\alpha)}{K - \frac{1}{2}\rho V^2 Sec\frac{\partial C_L}{\partial \alpha}} \,. \tag{2.6}$$

The divergence occurs when θ becomes infinite, with

$$K = \frac{1}{2}\rho V^2 Sec\frac{\partial C_L}{\partial \alpha} \,. \tag{2.7}$$

Finally, one can obtain the equation of the divergence speed, given by

$$V_d = \sqrt{\frac{2K}{\rho Sec\frac{\partial C_L}{\partial \alpha}}} \,. \tag{2.8}$$

One can conclude that the divergence speed can be increased by stiffening the wing or decreasing the distance between the aerodynamic and flexural centers. According to [7], the latter constitutes a penalty to weight and cost so designers opt to not choose that approach.

2.3 Dynamic Aeroelastic Problems

Dynamic aeroelasticity concerns the interaction between inertia, elastic, and unsteady aerodynamic forces. This dynamic problem differs from static aeroelasticity, since vibration is also involved. The most

important dynamic problems are *buffeting* and *flutter*. The latter is considered to be the most dangerous so its understanding and prevention is a crucial step in structural design.

According to Megson [7], *buffeting* is a dynamic phenomena that mostly occurs in a tailplane caused by the airflow coming from the wing wake, which strikes the airplane with a frequency equal to its natural frequency. Due to that, a resonant oscillation can occur. However, this problem can be alleviated by proper positioning of the tail and having a clean aerodynamic design.

A formal definition of *flutter* is the one from Hodges and Pierce [2]:

A dynamic instability of a flight vehicle associated with the interaction of aerodynamic, elastic, and inertial forces.

In fact, *flutter* is a self-excited oscillatory instability in which aerodynamic forces couple with the natural modes of vibration of a elastic body, producing vibrations with increasing amplitude. This phenomenon occurs at a critical or flutter speed, which is the lowest airspeed at which a given structure oscillates with sustained simple harmonic motion [7].

Above the flutter speed, the vibrations can be potentially destructive depending on how much they increase. As stated in [2], of the various phenomena categorized as aeroelastic flutter, lifting-surface flutter is the most usual and most likely to result in structural failure. In this type of flutter, known as *classical flutter*, flexural and torsional modes are coupled, as shown in Figure 2.4, and it is associated with potential flow. Next, the fundamental equations of motion of a linear aerodynamic system will be presented, as described in Hodges and Pierce [2].

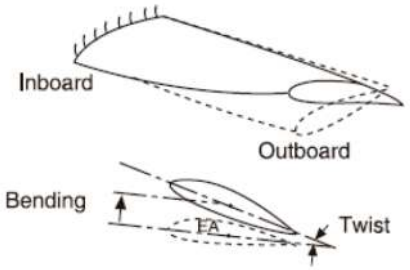

Figure 2.4: Coupling of bending and torsional oscillations [10].

2.3.1 Equations of Motion of a Linear Aeroelastic System

Consider the rigid and spring-restrained wing model, as shown in Figure 2.5. The plunge displacement *h* is measured in point P, while points C, Q and T refer, respectively, to the center of mass, the aerodynamic center and the three-quarter-chord. The spring constants k_h and k_θ represent, respectively, the plunge and torsional rigidity of the model. The dimensionless parameters *e* and *a* determine the locations of points C and P. The semi-chord is represented by the parameter *b*.

In order to formulate the equations of motion, one will use the Lagrange's equations [11], as

$$\frac{d}{dt}\left(\frac{\partial K}{\partial \dot{q}_i}\right) + \frac{\partial P}{\partial q_i} = Q_i, \qquad (i = 1, 2)\,, \tag{2.9}$$

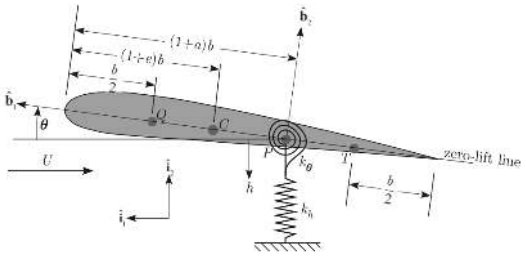

Figure 2.5: Representation of wing section with pitch and plunge movements [2].

where *K* is the kinetic energy, *P* is the potential energy, q_i is the displacement vector with $q_1 = h$, $q_2 = \theta$ and Q_i stands for the applied forces, namely,

$$Q_h = -L\,, \tag{2.10}$$

$$Q_\theta = M_{\frac{1}{4}} + b\Big(\frac{1}{2} + a\Big)L\,. \tag{2.11}$$

The deduction of the potential and kinetic energy equations can be found in [2]. Therefore, only the final form of these equations are presented, respectively, as

$$P = \frac{1}{2}k_h h^2 + \frac{1}{2}k_\theta \theta^2\,, \tag{2.12}$$

$$K = \frac{1}{2}m(\dot{h}^2 + 2bx_\theta \dot{h}\dot{\theta}) + \frac{1}{2}I_P\dot{\theta}^2\,, \tag{2.13}$$

where $I_P = I_C + mb^2x_\theta^2$, I_C is the moment of inertia about point C, *m* is the mass of the system and $x_\theta = e - a$ is the distance between the reference point and the center of mass. Finally, substituting in Eq. (2.9), the equations of motion become

$$\begin{aligned} &m(\ddot{h} + bx_\theta\ddot{\theta}) + k_h h = -L\,,\\ &I_P\ddot{\theta} + mbx_\theta\ddot{h} + k_\theta\theta = M_{\frac{1}{4}} + b\left(\frac{1}{2} + a\right)L\,. \end{aligned} \tag{2.14}$$

In the following section, some methods to predict the flutter speed of an aircraft wing will be reviewed, taking into account the equations of motion derived here.

2.3.2 Flutter Boundary Prediction

The Doublet Lattice Method [12] and the Strip-Theory [8] are common methodologies within the field of linear methods to predict the aeroelastic flutter. These methods are formulated in the frequency domain and, with the aid of computational techniques, such as the p-k method [13], it is possible to extract the aeroelastic system eigenvalues and infer about its dynamic stability.

Therefore, the p-k method is an iterative process for solving the non-linear eigenvalue problem which arises from aeroelastic problems. Equation (2.14), which describes the motion of an aeroelastic system

in its simplest form, can be transformed into matrix form

$$M\ddot{q} + Kq + \frac{1}{2}\rho V^2 Q(k, Mach)q = 0\,, \tag{2.15}$$

where *M* is the mass matrix, *K* is the stiffness matrix and *Q* is the generalized aerodynamic forces matrix, which is complex. The real part is denoted by Q_R and is in phase with the vibration displacement; the imaginary part is denoted by Q_I and is in phase with the vibration velocity [13]. *q* is a vector with the displacement variables *h* and θ, as described in the previous section. The aerodynamic generalized forces matrix *Q* is a function of reduced frequency $k = \omega b/V$, where ω is the natural frequency, *b* is the wing semi-chord and *V* is the airspeed.

The fundamental equation for flutter analysis by the p-k method is [14]

$$\left[p^2 M - p(\rho b V/4)Q_I/k + K - (\rho V^2/2)Q_R\right] q = 0\,, \tag{2.16}$$

being p_i the complex eigenvalue $\Gamma_i \pm j\Omega_i$, where Γ_i represents the transient decay rate coefficient and Ω_i represents the frequency. In state-space form, Eq. (2.16) becomes

$$(A - pI)q = 0, \quad where \quad A = \begin{bmatrix} 0 & I \\ -M^{-1}(K - \frac{1}{2}\rho V^2 Q_R) & \frac{1}{4}\rho V b Q_I M^{-1}/k \end{bmatrix}, \tag{2.17}$$

where I is the identity matrix. The flutter speed and frequency can be estimated using the eigenvalues of matrix A. The flutter speed is reached iteratively, increasing it until the real part Γ_i of one of the eigenvalues of A becomes positive. Typical response behavior is illustrated in Fig. 2.6, for positive, zero and negative values of Γ_i and $\Omega_i \neq 0$.

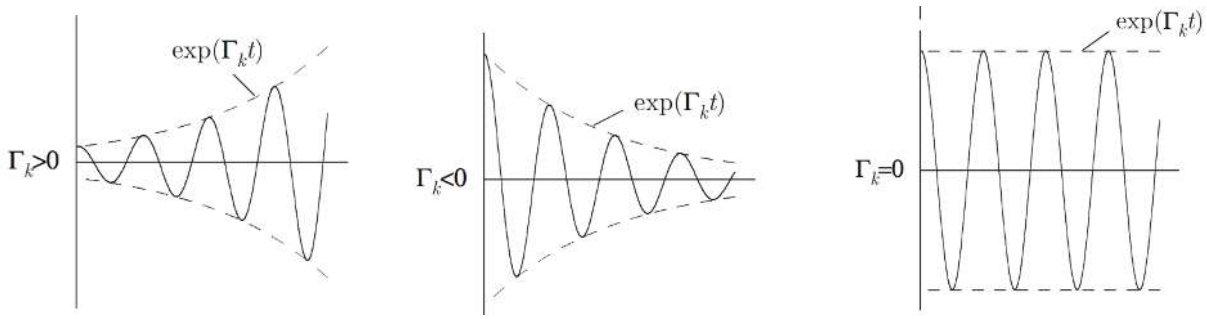

Figure 2.6: Response behavior when $\Omega_i \neq 0$, from [2].

More complex methodologies include the Panel Methods, which are based on potential aerodynamic theory and allow more complex 3D geometries and surface discretization schemes. However, they are formulated in the time domain and they are seldom used to perform flutter analysis. Nevertheless, the purpose of this work is to study the behavior of an aircraft wing under subsonic conditions in the time domain. Therefore, it requires a compatible aerodynamic model based on a panel method, which is presented in the following chapter.

Chapter 3

Computational Fluid Dynamics Model

In chapter 2, the fundamental equations of static and dynamic aeroelasticity were derived. All these equations present a term with the applied forces on the system, which are aerodynamic forces due to circulation of air around the wing.

The governing equations of fluid dynamics, as it will be seen in the following section, are complex and impracticable to solve entirely. That means approximations and assumptions must be made in order to compute the aerodynamic forces. One of these approximations is assuming the flow is incompressible and potential, as it will be discussed later in this chapter.

To compute the aerodynamic forces, a numerical method based on the level of approximation chosen will be used, due to the complexity of the geometry. Thereby, in this chapter, the fundamentals of fluid dynamics are presented alongside the possible levels of approximation, focusing on incompressible potential flow. Finally, an available computation aerodynamic model will be selected, explaining the numerical method on which it is based, how it works and validating it with existing experimental data.

3.1 Governing Equations of Fluid Dynamics

The fundamental governing equations of fluid dynamics are, essentially, the continuity, momentum and energy equations. According to Anderson *et al.* [15], *"these equations speak physics"*. In fact, they are based on the following physical principles:

- Mass conservation;
- Momentum conservation ($F = ma$);
- Energy conservation.

In order to apply these principles, a suitable model of the flow is needed. Therefore, consider the control volume presented in Figure 3.1. With this approach, the control volume is fixed in space while the flow moves through it. Consequently, the fluid flow equations obtained by applying the above principles to this control volume are called the *conservation* form of the governing equations [15].

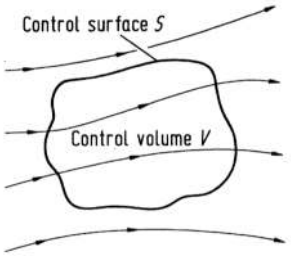

Figure 3.1: Control volume model [15].

In this work, the derivation of these equations is not pertinent, so only the final form will be presented. More details can be found in Anderson *et al.* [15]. Thereby, the following equations represent, respectively, the mathematical form of mass, momentum and energy conservation, and are known as the *Navier-Stokes* (NS) equations for viscous fluids:

$$\frac{\partial \rho}{\partial t} + \frac{\partial}{\partial x_j}\left(\rho u_j\right) = 0\,, \tag{3.1a}$$

$$\frac{\partial}{\partial t}\left(\rho u_i\right) + \frac{\partial}{\partial x_j}\left(\rho u_i u_j + p\delta_{ij} - \tau_{ji}\right) - \rho f_i = 0\,, \tag{3.1b}$$

$$\frac{\partial}{\partial t}\left(\rho E\right) + \frac{\partial}{\partial x_j}\left(\rho E u_j + p u_j - u_i \tau_{ij} + q_j\right) - \rho\left(\dot{q} + \vec{f_j}\cdot\vec{u}_j\right) = 0\,, \tag{3.1c}$$

where

- *E* is the total energy, $(e + V^2/2)$, *e* being the internal energy per unit mass and *V* the total velocity;
- ρ and *p* are, respectively, the density and pressure;
- $\vec{V} = (u_1, u_2, u_3) = (u, v, w)$, *u*, *v* and *w* being, respectively, the components of velocity in the *x*, *y* and *z* directions;
- $q_j = k\frac{\partial T}{\partial x_j}$, in which *k* is the thermal conductivity and *T* is the temperature;
- $\dot{q}$ is the rate of internal heat dissipation per unit mass;
- $\vec{f_j}$ is the vector of external applied forces on the system;
- τ_{ij} is the stress tensor, denoting a stress in the j-direction exerted on a plane perpendicular to the i-direction. Then,

$$\tau_{ij} = \begin{bmatrix} \lambda\nabla\cdot\vec{V} + 2\mu\frac{\partial u}{\partial x} & \mu\left(\frac{\partial v}{\partial x} + \frac{\partial u}{\partial y}\right) & \mu\left(\frac{\partial u}{\partial z} + \frac{\partial w}{\partial x}\right) \\ -- & \lambda\nabla\cdot\vec{V} + 2\mu\frac{\partial v}{\partial y} & \mu\left(\frac{\partial w}{\partial y} + \frac{\partial v}{\partial z}\right) \\ -- & -- & \lambda\nabla\cdot\vec{V} + 2\mu\frac{\partial w}{\partial z} \end{bmatrix} \tag{3.2}$$

  in which λ and μ are, respectively, the bulk viscosity coefficient and the molecular viscosity coefficient.

Anderson *et al.* [15] made some comments regarding the above equations, such as:

- The governing equations constitute a system of non-linear differential equations, and hence are very difficult to solve analytically;
- The system contains five equations with six variables, ρ, *p*, *u*, *v*, *w* and *e*. That means another equation is necessary, namely the equation of state for a perfect gas ($p = \rho RT$);
- The equation of state introduces a seventh variable, *T*, leading to the introduction of another equation, e.g., the thermodynamic relation for a calorically perfect gas ($e = c_v T$).

Due to the complexity of these equations, a numerical description of the flow field is necessary. Therefore, a *Computational Fluid Dynamics* (CFD) simulation is needed to obtain an approximated solution. The first step is to select the mathematical model, with an adequate approximation level. In the literature, there are several possible approximations for the fluid flow. Figure 3.2 presents a pyramid with the most important. Note that as one steps down, not only the computational costs decrease but also the complexity and accuracy of the approximation.

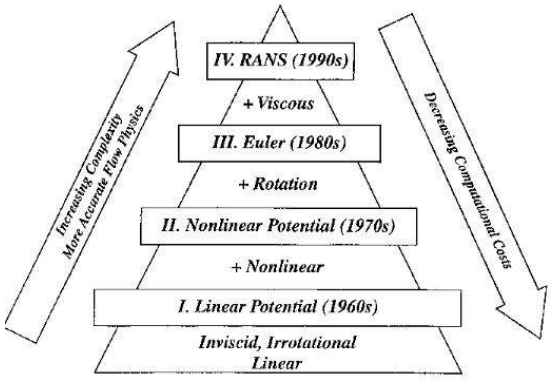

Figure 3.2: Levels of approximation for the fluid flow [16].

However, since this work is about aeroelastic analysis in the subsonic domain, at low Reynolds number, it makes sense to neglect the viscosity effects confined to thin boundary layers and the rotation of the fluid. Also, for simplicity, a linear analysis will be performed. For these reasons, the linear potential flow approximation, shown in the next section, will be the basis of the CFD model utilized in the aeroelastic analysis, presented at the end of this chapter.

3.2 Incompressible Potential Flow

The *Potential Flow Model* is a formulation in which the flow is assumed to be inviscid, irrotational and isentropic. In fact, this model can not compute shock waves nor the shear stresses and heat transfer terms from the Navier-Stokes equations (3.1). However, as it was explained before, it is found acceptable for this analysis because the airspeed is in the subsonic domain and no shocks nor separation effects are expected.

Thereby, based on the work by Katz and Plotkin [17], this model formulation will be presented including its basic solutions, in which some of them will be used in the numerical method to compute the pressure along the surface of the wing.

3.2.1 Basis of Potential Flow Problem

Since the flow is considered to be incompressible, $\frac{\partial \rho}{\partial t} = 0$, the continuity equation (Eq. 3.1a) becomes

$$\nabla \cdot \vec{V} = 0\,. \tag{3.3}$$

Moreover, since the fluid is irrotational, the velocity $\vec{V}$ can be defined as

$$\vec{V} = \nabla \phi\,, \tag{3.4}$$

where $\phi(x, y, z)$ is the velocity potential. Substituting in Equation (3.3), one obtains the *Laplace equation*

$$\nabla^2 \phi = 0\,. \tag{3.5}$$

According to [17], two conditions must be met in order to solve the previous equation:

- The impermeability condition, $\nabla\phi \cdot \vec{n} = 0$, where the normal component of velocity in relation to the fixed body surface must be zero;
- The disturbance created by the motion should decay far from the body, $\lim_{r\to\infty}(\nabla\phi - \vec{V}_\infty) = 0$, where $r = (x, y, z)$ and $\vec{V}_\infty$ is the velocity of the undisturbed fluid.

3.2.2 Elementary Solutions

One very important property of Eq. (3.5), a linear differential equation with many possible solutions, is the *Principle of Superposition*. This means that if $\phi_1, \phi_2, ..., \phi_n$ are solutions of the equation, then

$$\phi = \sum_{k=1}^{n} c_k \phi_k \tag{3.6}$$

is also a solution and $c_1, c_2, ..., c_n$ are arbitrary constants.

This principle plays an important role in formulating the potential model of the fluid around the wing, as it will be explained later in this chapter. Here, some solutions with physical interest using Cartesian coordinates will be presented.

Source/Sink

One possible solution for the Laplace equation is the source/sink element. The potential of this point element, located at (x_0, y_0, z_0) in the Cartesian system, is

$$\phi(x, y, z) = -\frac{\sigma}{4\pi\sqrt{(x - x_0)^2 + (y - y_0)^2 + (z - z_0)^2}}\,, \tag{3.7}$$

where σ is the strength of the source/sink, that is, the volumetric rate the fluid comes from the source ($\sigma > 0$) or goes into the sink ($\sigma < 0$).

According to equation (3.4), the velocity vector is given by

$$\vec{V} = \begin{Bmatrix} u \\ v \\ w \end{Bmatrix} = \nabla\phi = \frac{\sigma}{4\pi\left[(x-x_0)^2+(y-y_0)^2+(z-z_0)^2\right]^{3/2}} \begin{Bmatrix} (x-x_0) \\ (y-y_0) \\ (z-z_0) \end{Bmatrix} . \tag{3.8}$$

Doublet

The next basic solution of the Laplace equation is the doublet, which happens when one sink and one source with the same strength σ are present and the distance between them becomes zero. In this case, the potential function due doublet elements located at (x_0, y_0, z_0), in the x, y and z directions yields

$$\phi(x,y,z) = \frac{\mu}{4\pi} \begin{Bmatrix} \frac{\partial}{\partial x} \\ \frac{\partial}{\partial y} \\ \frac{\partial}{\partial z} \end{Bmatrix} \frac{1}{\sqrt{(x-x_0)^2+(y-y_0)^2+(z-z_0)^2}} . \tag{3.9}$$

The velocity components can be obtained, once again, applying equation (3.4), as follows:

$$\vec{V} = \begin{Bmatrix} u \\ v \\ w \end{Bmatrix} = \frac{\mu}{4\pi\left[(x-x_0)^2+(y-y_0)^2+(z-z_0)^2\right]^{5/2}} \begin{Bmatrix} -(y-y_0)^2+(z-z_0)^2-2(x-x_0)^2 \\ 3(x-x_0)(y-y_0) \\ 3(x-x_0)(z-z_0) \end{Bmatrix} . \tag{3.10}$$

Polynomials

The Laplace equation is a second-order differential equation and so, a linear function is also a solution. Hence, the potential function due to a constant free-stream flow is, in general

$$\phi(x,y,z) = U_\infty x + V_\infty y + W_\infty z\,, \tag{3.11}$$

where $(U_\infty, V_\infty, W_\infty)$ are the components of stream velocity, respectively, in the x, y and z directions. A second-order polynomial can also be a solution with many constants satisfying certain conditions, e.g., for a fluid around a corner or against a plate.

Vortex

The vortex is another possible solution for the Laplace equation. It consists of a vortex flow, irrotational everywhere except at the core [17]. The potential function, for a vortex located at (x_0, z_0) is

$$\phi(x,z) = -\frac{\Gamma}{2\pi} tan^{-1}\frac{z-z_0}{x-x_0}\,, \tag{3.12}$$

where Γ is the circulation. The respective velocity components are

$$\vec{V} = \begin{Bmatrix} u \\ w \end{Bmatrix} = \frac{\Gamma}{2\pi\left[(z-z_0)^2+(x-x_0)^2\right]} \begin{Bmatrix} z-z_0 \\ -(x-x_0) \end{Bmatrix} . \tag{3.13}$$

In the next section, some of these basic solutions will be used to characterize the fluid flow together with a numerical approach based on panel methods. Its basic formulation will be presented alongside some physical concepts necessary to understand it.

3.3 Panel Method

The panel method presented here is based on the surface distribution of singularity elements, which were presented in the previous section. Its solutions resides on finding the strength of the singularity elements distributed on the body surface and, consequently, computing the velocity and pressure distribution. The major advantage of this method, comparing to widely used finite-difference methods, is that it is more efficient and economical from the computational point of view. However, this comparison holds for incompressible flows only as the effects of viscosity are being neglected, whereas finite-difference methods are usually used to solve more complex geometries. Once again, the following presentation is based on the work of Katz and Plotkin [17].

3.3.1 General Formulation

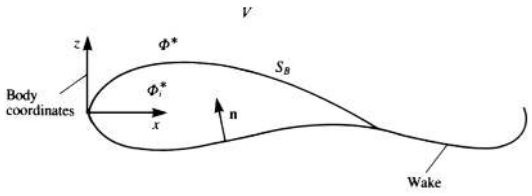

Figure 3.3: Potential flow around a body [17].

Consider the body illustrated in Figure 3.3, submerged in a potential flow. The total potential is given by the Laplace equation (Eq. (3.5)). This equation, however, has multiple solutions as described in the previous section. In this case, according to [17], the effect of thickness can be simulated using source elements whereas for lifting problems doublet elements can be used. There are some considerations to be made regarding the wake, such as the initial orientation and geometry but it is likely that it can be modeled with doublet elements.

Based on Green's identity [17], Eq. (3.5) can be developed by a sum of source σ and doublet μ distributions placed on the boundary of the body and the wake, as

$$\phi(x,y,z) = \frac{1}{4\pi}\int_{body+wake} \mu\vec{n}\cdot\frac{\partial}{\partial n}\left(\frac{1}{r}\right)dS - \frac{1}{4\pi}\int_{body}\sigma\left(\frac{1}{r}\right)dS + \phi_\infty\,, \tag{3.14}$$

where $\vec{n}$ is a vector normal to the surface S_B (Figure 3.3), *r* is the distance between the element and the point of reference and ϕ_∞ is the free-stream potential (Eq. (3.11)).

Of course, in order to solve Eq. (3.14) for the whole body, some boundary conditions need to be specified. In order to do that, there are two possibilities:

Neumann boudady condition

In this case, the boundary condition is specified for every point on the surface of the body, as follows:

$$\nabla(\phi + \phi_\infty) \cdot \vec{n} = 0\,. \tag{3.15}$$

Substitution of Eq. (3.14) into the boundary condition in Eq. (3.15) results in

$$\left\{ \frac{1}{4\pi} \int_{body+wake} \mu \nabla \left[\frac{\partial}{\partial n} \left(\frac{1}{r} \right) \right] dS - \frac{1}{4\pi} \int_{body} \sigma \nabla \left(\frac{1}{r} \right) dS + \nabla \phi_\infty \right\} \cdot \vec{n} = 0\,. \tag{3.16}$$

Dirichlet boundary condition

In this case, the boundary condition (Eq. (3.15)) is specified in terms of the potential inside the body, ϕ_i, that is,

$$\phi_i = (\phi + \phi_\infty)_i = const.\,, \tag{3.17}$$

and Eq. (3.14) becomes

$$\phi_i(x, y, z) = \frac{1}{4\pi} \int_{body+wake} \mu \vec{n} \cdot \frac{\partial}{\partial n} \left(\frac{1}{r} \right) dS - \frac{1}{4\pi} \int_{body} \sigma \left(\frac{1}{r} \right) dS + \phi_\infty = const.\,. \tag{3.18}$$

The constant can be set to ϕ_∞ (the justification can be consulted in [17]) and Eq. (3.18) reduces to:

$$\frac{1}{4\pi} \int_{body+wake} \mu \vec{n} \cdot \frac{\partial}{\partial n} \left(\frac{1}{r} \right) dS - \frac{1}{4\pi} \int_{body} \sigma \left(\frac{1}{r} \right) dS = 0\,. \tag{3.19}$$

The source strength is required to be

$$\sigma = \vec{n} \cdot \vec{Q}_\infty\,, \tag{3.20}$$

where Q_∞ is the free-stream velocity.

Finally, to completely define this problem, the wake doublet strength needs to be known. One possible formulation is to apply the Kutta condition in terms of the doublet strength at the trailing edge. In this case, μ is constant in the wake (μ_w) and is equal to the value at the trailing-edge (μ_{TE}) [17], yielding

$$\mu_w = const. = \mu_{TE} \leftrightarrow \mu_U - \mu_L = \mu_w\,, \tag{3.21}$$

where μ_U and μ_L are, respectively, the upper and lower surface doublet strengths at the trailing edge.

3.3.2 Reduction to a Set of Linear Algebraic Equations

To obtain a solution for the problem, the body surface is divided into *N* surface panels and N_W additional wake rectilinear panels, each one assumed to have constant strength. Dirichlet and Kutta boundary conditions are selected. Each panel has, in its center, a *collocation point P*. For each point P, the contribution of the influences of all *k* body panels and *l* wake panels is needed. Therefore, Eq. (3.19)

for each of the N collocation points, transforms into:

$$\sum_{k=1}^{N} \frac{1}{4\pi} \int_{bodypanel} \mu \vec{n} \cdot \nabla \left(\frac{1}{r}\right) dS + \sum_{l=1}^{N_W} \frac{1}{4\pi} \int_{wakepanel} \mu \vec{n} \cdot \nabla \left(\frac{1}{r}\right) dS - \sum_{k=1}^{N} \frac{1}{4\pi} \int_{bodypanel} \sigma \left(\frac{1}{r}\right) dS = 0\,. \tag{3.22}$$

The influence of a panel on a collocation point depends only on the panel geometry. The influence of a panel k at point P (Figure 3.4), with constant μ or σ is, respectively,

$$C_k = \frac{1}{4\pi} \int_{1,2,3,4} \frac{\partial}{\partial n} \left(\frac{1}{r}\right) dS|_k\,, \tag{3.23a}$$

$$B_k = \frac{-1}{4\pi} \int_{1,2,3,4} \left(\frac{1}{r}\right) dS|_k\,. \tag{3.23b}$$

Applying Kutta condition (Eq. 3.21), the influence of the wake element becomes

$$C_w \mu_w = C_w(\mu_U - \mu_L)\,. \tag{3.24}$$

A new coefficient can be created adding the influence of the wake element into the C_k coefficients, such that

- $A_k = C_k$ if panel is not at trailing-edge.
- $A_k = C_k \pm C_w$ if panel is at trailing-edge.

In the end, for each collocation point P, Eq. (3.22) becomes

$$\sum_{k=1}^{N} A_k \mu_k = -\sum_{k=1}^{N} B_k \sigma_k \tag{3.25}$$

This results in a system of N linear equations with the N unknown variables μ_k. The information of the source strengths σ_k comes from Eq. (3.20).

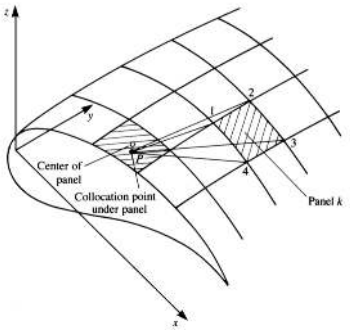

Figure 3.4: Influence of panel k at point P [17].

Once the strengths of each panel are calculated, the two tangential and normal velocity components are, respectively,

$$V_l = -\frac{\partial \mu}{\partial l}, \quad V_m = -\frac{\partial \mu}{\partial m}, \quad V_n = -\sigma\,, \tag{3.26}$$

where (l, m, n) are the local coordinates of the panel being n normal to the panel. The total velocity on panel *k* becomes

$$\vec{V}_k = (V_{\infty l}, V_{\infty m}, V_{\infty n})_k + (V_l, V_m, V_n)_k \,. \tag{3.27}$$

3.3.3 Unsteady Case

The continuity equation, as seen before, does not include time-dependent terms for the incompressible potential flow. That means one has to include special boundary conditions in the problem to achieve time dependency. In fact, the methods of solution presented for the steady case can be used here with only small modifications. As stated in Katz and Plotkin [17], these modifications will include the application of the "*zero normal flow on a solid surface*" boundary conditions.

In order to apply those conditions, it is useful to describe the unsteady motion of the surface in a body-fixed coordinate system *(x,y,z)*, whose location $\vec{R}_0(t)$ and orientation $\vec{\Theta}(t)$ in relation to a stationary, inertial frame of reference *(X,Y,Z)* are, respectively,

$$\vec{R}_0(t) = (X_0, Y_0, Z_0) \,, \tag{3.28a}$$

$$\vec{\Theta}(t) = (\phi, \theta, \psi) \,. \tag{3.28b}$$

For example, the position of the body-fixed coordinate system in the case of a constant-velocity flow speed U_∞ in the positive x direction (in the inertial system) would be $\vec{R}_0(t) = (X_0, Y_0, Z_0) = (-U_\infty t, 0, 0)$, meaning it is the wing that is being translated.

Since the Laplace Equation (Eq. (3.5)) is still valid in the body-fixed coordinate system (demonstrated in [17]), the zero-velocity condition, in the body frame, becomes

$$(\nabla\phi + \vec{v}) \cdot \vec{n} = 0 \Leftrightarrow (\nabla\phi - \vec{V}_0 - \vec{v}_{rel} - \vec{\Omega} \times \vec{r}) \cdot \vec{n} = 0 \,, \tag{3.29}$$

where $\vec{V}_0 = (\dot{X}_0, \dot{Y}_0, \dot{Z}_0)$ and $\vec{\Omega}$ are, respectively, the velocity and rate of rotation of the body-fixed frame, and $\vec{v}_{rel}$ represents additional relative motion in the case of small oscillations.

Finally, applying this change to the Neumann boundary condition, Eq. (3.16) becomes

$$\left\{ \frac{1}{4\pi} \int_{body+wake} \mu \nabla \left[\frac{\partial}{\partial n} \left(\frac{1}{r} \right) \right] dS - \frac{1}{4\pi} \int_{body} \sigma \nabla \left(\frac{1}{r} \right) dS - \vec{V}_0 - \vec{v}_{rel} - \vec{\Omega} \times \vec{r} \right\} \cdot \vec{n} = 0 \,. \tag{3.30}$$

The source strength σ, defined in Eq. (3.20), becomes

$$\sigma = -\vec{n} \cdot (\vec{V}_0 + \vec{v}_{rel} + \vec{\Omega} \times \vec{r}) \,. \tag{3.31}$$

3.3.4 Wake Shape

In the steady case, the initial wake geometry is specified by the programmer and then several wake grid panels are established. In order to achieve convergence, a process called *wake relaxation* [17] is employed. In this process, the first calculation is normally performed and the velocity induced by the

wing and wake on each wake point is obtained. Next, the wake points are moved by the local velocity times an artificial time parameter until convergence is achieved.

In the unsteady case, this process is clearly inadequate, because of the need of wake stabilization. Therefore, a *time-marching method* is employed. The main difference between this process and the relaxation is that now the time step is directly related to the motion. During the computations, the number of wake panels increase with time, as follows:

- Assuming velocity remains constant, the whole wake is moved by a distance which is equal to the free stream velocity times the time step size. The doublet strength of the moved panels remain unchanged;
- The trailing edge is linked to the last wake row;
- The new flow state is calculated, adding all the wake influences to the body panels. The doublet strengths of the new row of wake panels are obtained with the Kutta condition (Eq. 3.21).

3.3.5 Pressure Computation

The purpose of the computational aerodynamic analysis is to compute the aeodynamic forces applied in the body, derived from the pressure distribution. To do so, the velocity field $\vec{V}$ is calculated according to the steps described in this chapter, followed by the calculation of the pressure field. Since the pressure derivation is slightly different for the unsteady case, the formulation will be presented for two cases: steady and unsteady flow.

Steady Flow

To compute the pressure distribution, the *Bernoulli equation* for inviscid, incompressible and irrotational flow will be used,

$$E + \frac{p}{\rho} + \frac{V^2}{2} + \frac{\partial \phi}{\partial t} = F(t)\,, \tag{3.32}$$

where *E* is a potential so that $\vec{f} = -\nabla E$, $\vec{f}$ representing conservative external body forces. This equation is a function of time only and its left-hand side is constant at a certain time t_1.

Comparing a generic point on the field with a reference point, such as infinity, results

$$\left[E + \frac{p}{\rho} + \frac{V^2}{2} + \frac{\partial \phi}{\partial t}\right] = \left[E + \frac{p}{\rho} + \frac{V^2}{2} + \frac{\partial \phi}{\partial t}\right]_\infty . \tag{3.33}$$

When the reference point is chosen as infinity, $E_\infty = 0$ and $\phi_\infty = const.$. Furthermore, in the case of a steady problem with no external forces, Eq. (3.33) holds

$$p_\infty + \frac{1}{2}\rho V_\infty^2 = p + \frac{1}{2}\rho V^2 \tag{3.34}$$

In the end, the pressure coefficient is defined as

$$C_p = \frac{p - p_\infty}{0.5\rho V_\infty^2} = 1 - \left(\frac{V}{V_\infty}\right)^2 . \tag{3.35}$$

Unsteady Flow

According to [17], for the unsteady case, the Bernoulli equation (3.32) becomes

$$\frac{p_{ref} - p}{\rho} = \frac{V^2}{2} - \frac{v_{ref}^2}{2} + \frac{\partial \phi}{\partial t} . \tag{3.36}$$

Once again, considering the infinity as the point of reference, the pressure coefficient is

$$C_p = \frac{p - p_\infty}{0.5\rho V_\infty^2} = 1 - \left(\frac{V}{V_\infty}\right)^2 - \frac{2}{V_\infty^2}\frac{\partial \phi}{\partial t} . \tag{3.37}$$

In order to solve Eq. (3.37) in time, a time discretization method is needed. An implicit method is required, as the objective is to obtain the pressure coefficient at time $t + \Delta t$. Several methods are presented by Hirsch [18]. The largely used option is the *Backward Euler Method*, which applied to Eq. (3.37) yields

$$C_p^{t+\Delta t} = 1 - \frac{(V^{t+\Delta t})^2}{V_\infty^2} - \frac{2}{V_\infty^2}\left(\frac{\phi^{t+\Delta t} - \phi^t}{\Delta t}\right) . \tag{3.38}$$

3.4 Selection and Validation of CFD Program

In order to obtain the pressure distribution of an aircraft wing, using the panel methods described in this chapter, a CFD program developed by Cardeira [19], as part of his Master's thesis, was chosen. It was developed in Matlab® [20] language and it is only valid for potential flows, which is within the scope of this thesis.

3.4.1 Steps to Reach a Numerical Solution

The sequence that follows represents the steps necessary to establish a numerical solution.

Selection of singularity elements and boundary conditions

The program uses first order source and doublet singularity elements as solutions for the Laplace equation (3.5) over the wing. The Dirichlet boundary condition (Eq. (3.19)) is also implemented in the code. Cardeira [19] justifies these choices with some studies made about their effect on the accuracy of results and computational time. It was proven that, for aircraft wings, these choices are adequate to get good results without compromising the computational time.

Discretization of geometry and grid generation

In this step, the element corner and collocation points are defined, the latter being where the boundary conditions are enforced. Figure 3.5 represents a wing discretized with 16x10 panels, chord and spanwise directions respectively.

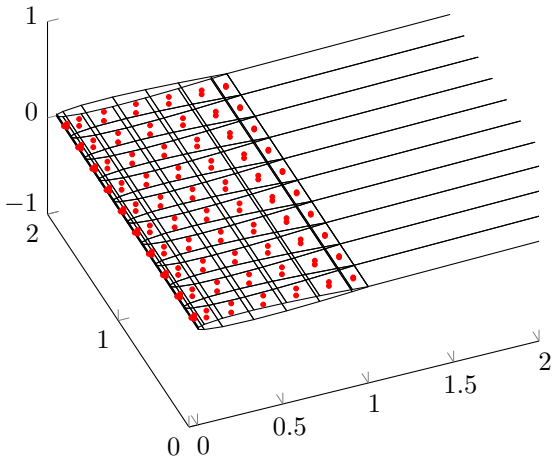

Figure 3.5: Discretization of aircraft wing and wake, with 16x10 panels (collocation points in red).

Influence Coefficients Computation

In this phase, for each collocation point, the influence coefficients are derived based on Eq. (3.23). This is generated in an automatic manner, through a loop implemented in Matlab®.

Solving Linear Set of Equations

Having computed the influence coefficients as well as the right-hand side of Eq. (3.25), the solution is obtained for all collocation points, resulting in the singularity strengths and the velocity field.

Post-Processing

Finally, pressures are computed using Bernoulli's equation. Aerodynamic loads and coefficients are derived by adding up the contributions of each panel.

3.4.2 Steady Aerodynamic Analysis

In order to validate the results obtained by this program, a steady aerodynamic analysis of a rectangular wing is employed. The results are compared with numerical and experimental results of a similar panel method developed by Baltazar [21]. To have the same conditions, a mesh of 64x32 panels is used. The plots in Figures 3.6 and 3.7 represent the pressure distributions in specific spanwise sections of the wing, with an aspect-ratio $AR = 4$ and NACA 0015 airfoil, for angles of attack of $2.5°$ and $8.5°$, respectively.

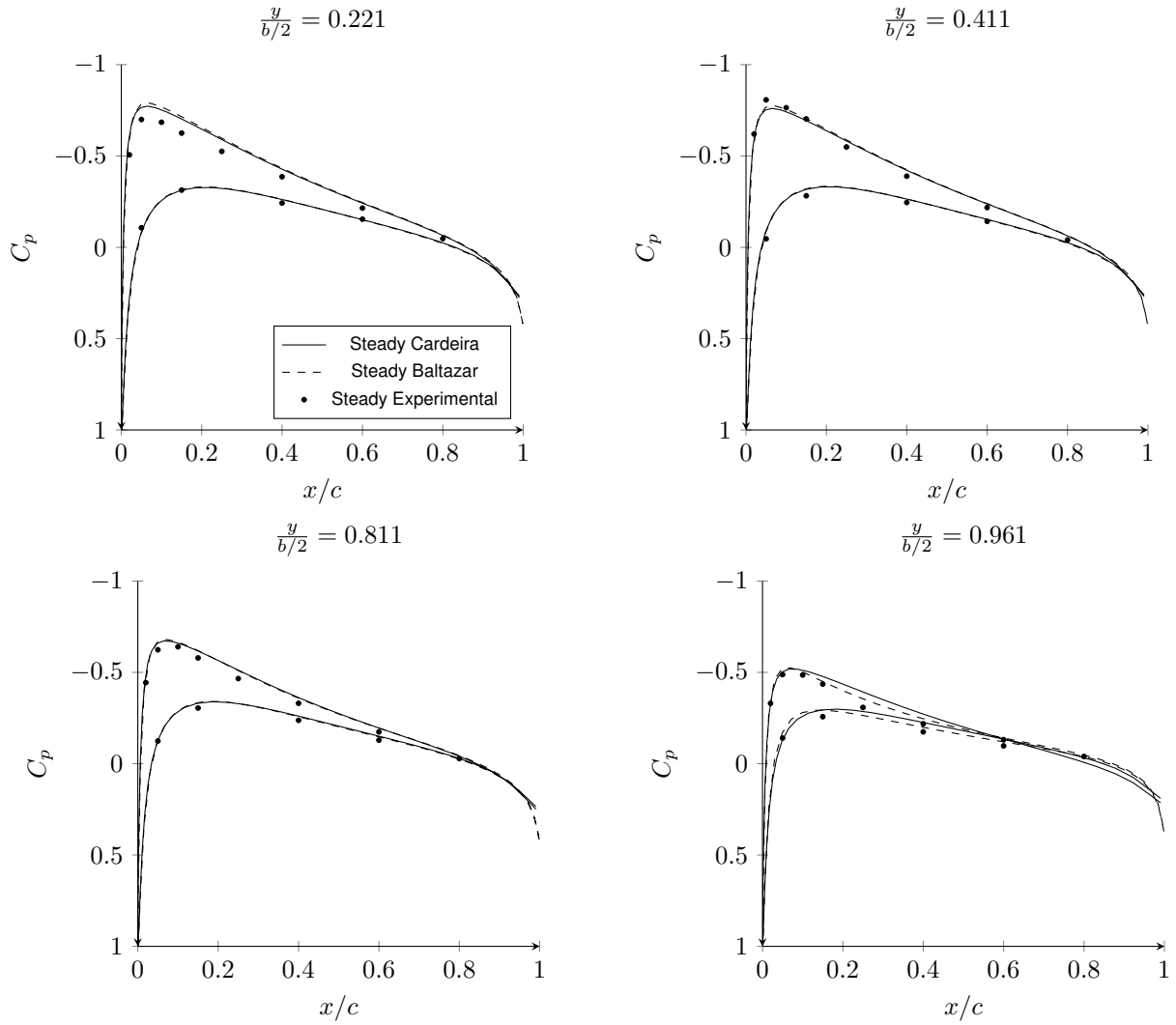

Figure 3.6: Pressure distributions for specific spanwise locations, with 64x32 panels and $\alpha = 2.5°$.

In order to evaluate the results with the mesh refinement, a rectangular wing with NACA 0010 airfoil, $AR = 4$, $b/2 = 2m$ and $c = 1m$ is evaluated at $\alpha = 6°$. Table 3.1 presents the values of lift and drag coefficients for different meshes, which are compared between the two programs.

Mesh	Steady Cardeira		Steady Baltazar	
	C_L	C_D	C_L	C_D
16x10	0.0884	0.0038	0.1082	0.0039
32x18	0.0940	0.0064	0.1024	0.0034
64x34	0.0959	0.0074	0.1002	0.0032
128x66	0.0965	0.0079	0.0993	0.0031

Table 3.1: Steady lift and drag coefficient results comparison for different mesh sizes.

Analyzing Figures 3.6 and 3.7, it can be concluded that the results from both programs are very similar. Moreover, these figures show a good approximation between the numerical and experimental

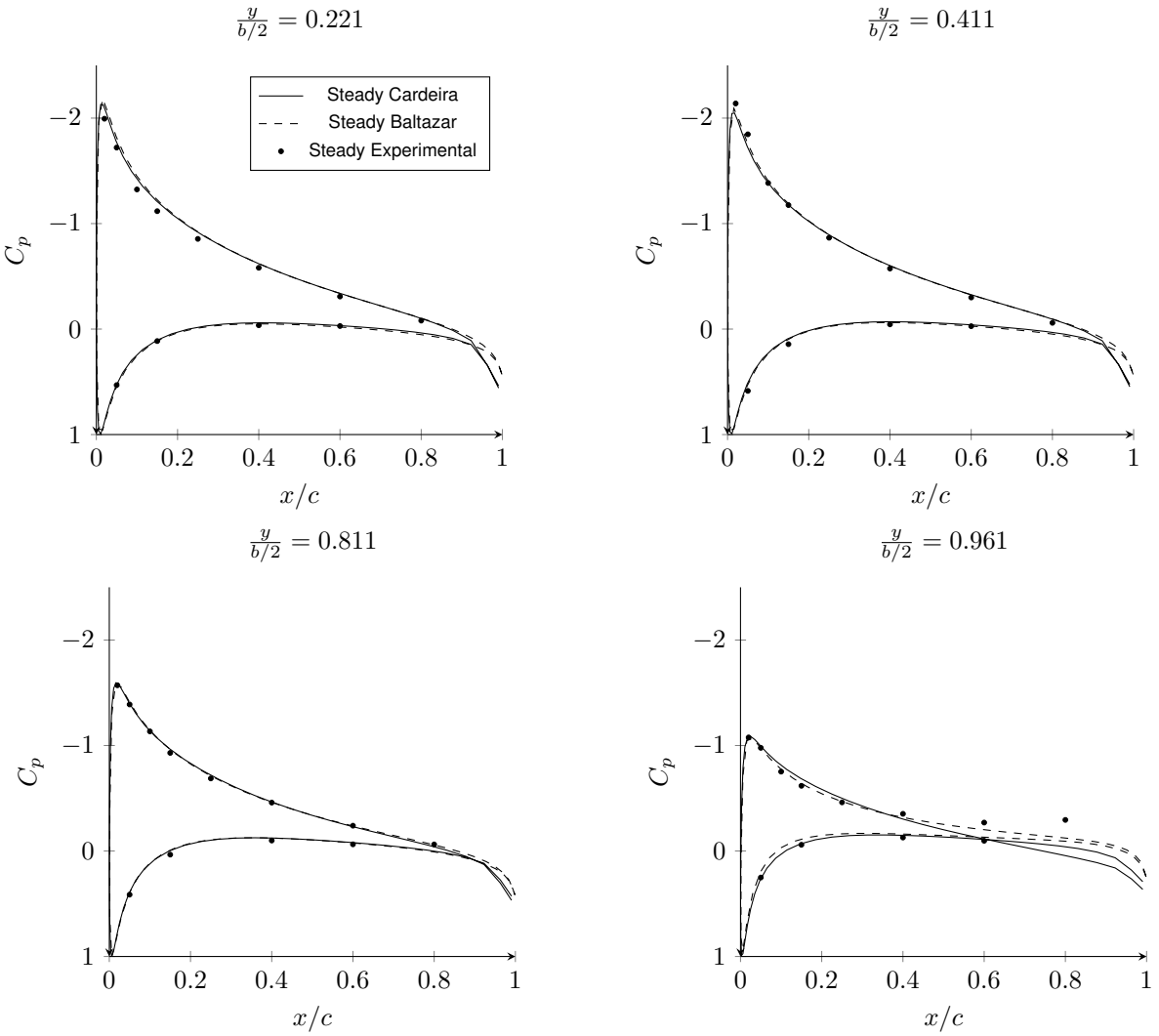

Figure 3.7: Pressure distributions for specific spanwise locations, with 64x32 panels and $\alpha = 8.5°$.

results, even at the wing tip.

Table 3.1 shows that, with an increasing mesh refinement, the values of C_L are approximated from *Steady Cardeira* to *Steady Baltazar*, while the opposite occurs regarding C_D. However, the values of drag are not so relevant for aeroelastic analysis as the lift, not only because they are much lower but also due to the pitching movement of the wing being mainly caused by the action of the lift forces.

3.4.3 Unsteady Aerodynamic Analysis

In this analysis, the same wing from the previous section, with NACA 0010 airfoil, $AR = 4$, $b/2 = 2m$, $c = 1m$, $\alpha = 6°$ and 16x10 panels, which revealed to be in agreement with *Steady Baltazar* code (see Table 3.1), is used to perform unsteady analysis. The main difference resides in the time discretization, which has also influence on the results.

An example of application of the unsteady program is shown in Figure 3.8. Here, 10 steps of 1 second were used to discretize the time. The wake panels are moved with the instantaneous flow velocity.

Figure 3.9 represents the variation with time of the three-dimensional lift and drag coefficients. It

is concluded that both values tend towards a stable position, in which the variation is not significant. This is natural since the wake is stabilized as well. Another significant conclusion is that the values obtained in this analysis are lower than those obtained in the steady case. This is due to the temporal term present in Eq. (3.37), that is, $\frac{\partial \phi}{\partial t}$, which changes the value of C_p in comparison with the steady case.

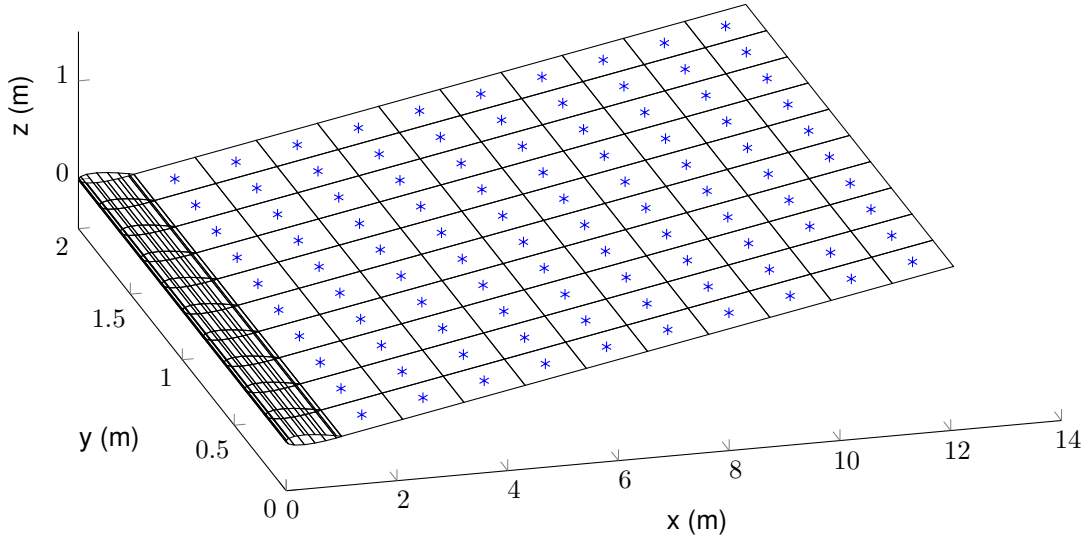

Figure 3.8: Wake movement in an unsteady analysis, with a time discretization of 10 steps each one with 1 second (blue marks are collocation points).

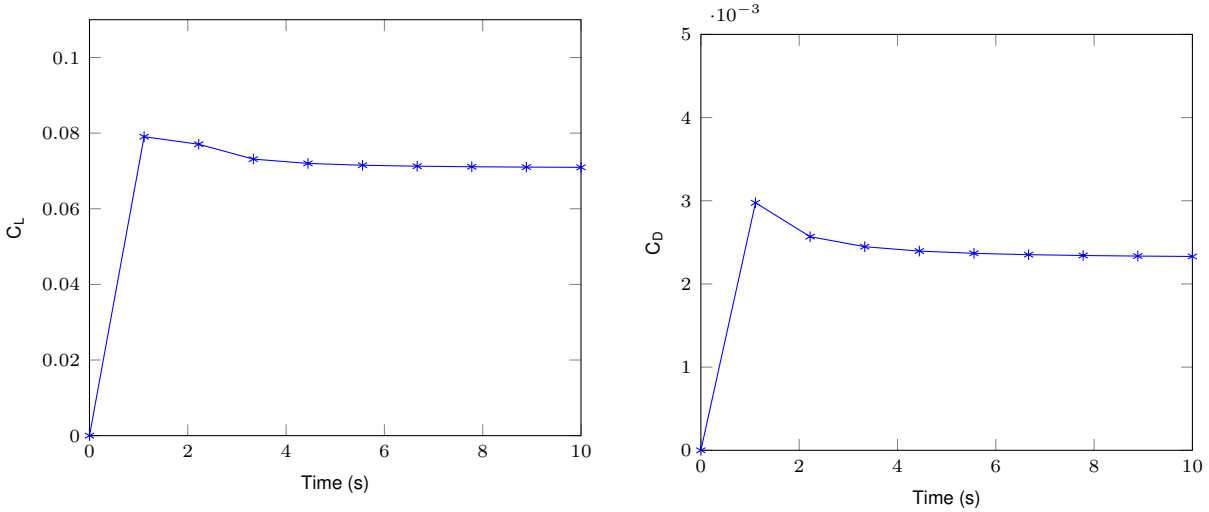

Figure 3.9: Unsteady 3D lift coefficient (C_L) and 3D drag coefficient (C_D).

Chapter 4

Computational Structural Dynamics Model

In Chapter 3, the numerical method used to compute the aerodynamic forces was explained and demonstrated. In order to have an aeroelastic framework, capable of predicting the displacement of the wing caused by the aerodynamic forces, a structural dynamic tool needs to be developed. This chapter deals with the development of the Finite Element Method (FEM) code, which is used to discretize the aircraft wing and compute the structural solution. In the end, the steps to reach the Computational Structural Dynamics (CSD) model are presented alongside three different analyses, namely, static, transient and modal, to verify and validate the structural model.

4.1 FEM: 3D Beam Element Formulation

The structural dynamics of an aircraft wing comprises a set of mathematical models which are difficult to solve for the desired variables of the system and for a variety of input parameters that characterizes its complex geometry. Therefore, it becomes necessary the use of numerical simulations of the phenomena.

In this work, the finite element method is employed to evaluate the response of an elastic wing due to aerodynamic loads varying in time. This method has three main features [22]:

- The geometry domain is discretized into a set of simple subdomains, called finite elements. Their collection is called the finite element mesh;
- The physical process is evaluated at each element and approximated by functions (e.g. polynomials) and algebraic equations are developed at each element corners, called nodes, relating physical quantities;
- The element equations are assembled using continuity and the solution is obtained for every node.

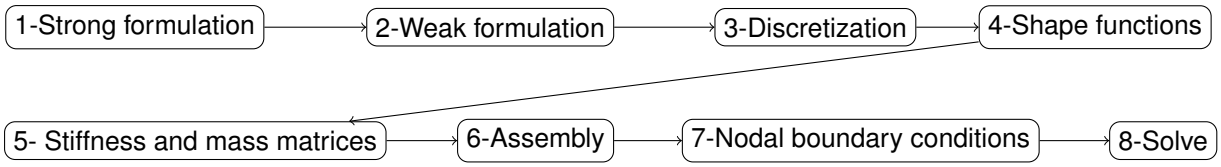

Figure 4.1: Basic steps of the FEM.

Figure 4.1 represents the basic steps of the FEM. It begins with the establishment of the *strong formulation* of the phenomena, *i.e.*, the partial differential equation, and the *weak formulation*, where the differential equation is multiplied by an arbitrary field and integrated over the element. A *discretization* of the geometry over space follows, resulting in a finite element mesh. Then, the *shape and weight functions* are selected, relating the nodal and global values of the primary variables. The element *stiffness and mass matrices* are computed and *assembled* and, finally, the global linear system of equations are *solved* to obtain the nodal values. With the solution obtained, several physical quantities can be computed within the element, such as, stresses and strains.

4.1.1 Constitutive Equations

In linear materials, Hooke's Law can be generalized and applied to three-dimensional bodies. Therefore, for an isotropic material, the stress can be related to the strain by [23]

$$\vec{\sigma} = D\vec{\varepsilon}, \tag{4.1}$$

where $\vec{\sigma} = (\sigma_x, \sigma_y, \sigma_z, \tau_{xy}, \tau_{xz}, \tau_{yz})$ and $\vec{\varepsilon} = (u_x, u_y, u_z, \theta_x, \theta_y, \theta_z)$ are, respectively, the stress and strain vectors and D is the elasticity or elastic stiffness matrix. Its inverse is defined by

$$D^{-1} = \begin{bmatrix} 1/E & -\nu/E & -\nu/E & 0 & 0 & 0 \\ -\nu/E & 1/E & -\nu/E & 0 & 0 & 0 \\ -\nu/E & -\nu/E & 1/E & 0 & 0 & 0 \\ 0 & 0 & 0 & 1/G & 0 & 0 \\ 0 & 0 & 0 & 0 & 1/G & 0 \\ 0 & 0 & 0 & 0 & 0 & 1/G \end{bmatrix}, \tag{4.2}$$

where E is the Young's modulus, ν is the Poisson ratio and G is the shear modulus. In cases of plane stress, the matrix D in Eq. (4.1) yields

$$D = \frac{E}{1-\nu^2} \begin{bmatrix} 1 & \nu & 0 \\ \nu & 1 & 0 \\ 0 & 0 & (1-\nu)/2 \end{bmatrix}, \tag{4.3}$$

where G has been replaced by the isotropic relation $G = E/2(1+\nu)$ and the stress and strain vectors reduce to $\vec{\sigma} = (\sigma_x, \sigma_y, \tau_{xy})$ and $\vec{\varepsilon} = (u_x, u_y, \theta_z)$ respectively.

4.1.2 3D Beam Element Description

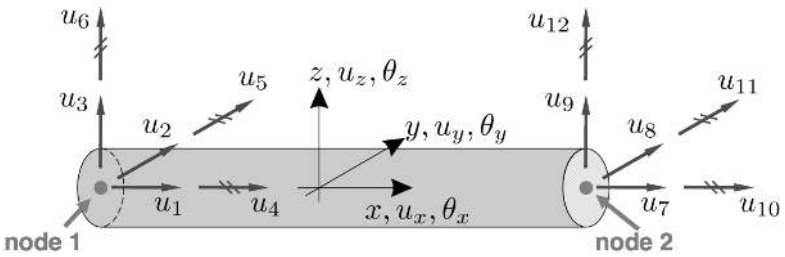

Figure 4.2: 3D beam element.

In this work, a fine element code was developed to describe an equivalent aircraft wing beam model. For this, the structure of the wing is modeled as a linear finite element structure that can undergo bending and torsion, with all rigidity concentrated at the nodes. This model has lower complexity and lower computational times than higher fidelity models. However, these factors are crucial in the preliminary design stages and optimization, increasing computational efficiency while capturing the most important structural responses.

To model the wing as an equivalent beam, a 3D beam element was selected, as illustrated in Figure 4.2. This element has 2 nodes and 6 degrees of freedom per node: 3 translational and 3 rotational degrees of freedom, measured in a Cartesian system. The element formulation is based on Euler-Bernoulli beam theory [24], which means the cross-sections remain rigid, thereby uncoupling the bending and torsional displacements.

Before presenting the element formulation, some assumptions must be made. This element considers only small deformations and has two planes of symmetry where axial deformation, bending and twist can be decoupled and looked at separately. Therefore, this element is composed of 4 elements: 1 bar element, with only axial displacements; 1 torsion element, with only rotation about the x axis and, finally, 2 beam elements with translational and rotational deformation in the xz and xy planes, respectively.

Over the next sections, the element formulation will be presented, as well as the stiffness and mass matrices, based on the work of Reddy [22] and Cook *et al.* [25].

4.1.3 Strong and Weak Formulation

Axial Deformation

The axial deformation equation of a beam subjected only to axial forces is given by

$$\frac{d}{dx}\left(EA\frac{du_x}{dx}\right) + b(x) = 0\,, \tag{4.4}$$

where A is the area of the beam cross-section, E is the Young's modulus of the material, u_x is the axial displacement along the x axis and $b(x)$ is the axial applied force per unit length.

Equation (4.4), a second order differential equation, needs two boundary conditions. Displacement and boundary applied force are possible boundary conditions, *e.g.*, $u(x_1) = u_1$ and $F(x_2) = AE\frac{du}{dx}|_{x_2} =$

F_2. This is the strong formulation of axial deformation.

To establish the weak formulation, Eq. (4.4) must be multiplied with an arbitrary function $v(x)$ (weight function) and integrated over the length L of the beam, that is

$$\int_0^L v\left(\frac{d}{dx}\left(AE\frac{du_x}{dx}\right)+b(x)\right)dx=0\,. \tag{4.5}$$

Using integration by parts of the first term, the weak formulation is obtained,

$$\left[vAE\frac{du_x}{dx}\right]_0^L-\int_0^L\left(\frac{dv}{dx}AE\frac{du_x}{dx}-vb\right)dx=0\,. \tag{4.6}$$

Bending Deformation

The bending equation of a beam in the xz plane subjected to shear forces and moments is given by

$$\frac{d^2}{dx}\left(EI_{yy}\frac{d^2u_z}{dx^2}\right)-q(x)=0\,, \tag{4.7}$$

where I_{yy} is the area moment of inertia about the y axis, u_Z is the vertical displacement and $q(x)$ is a distributed force in the z direction along the x axis. This equation also yields for bending in the xy plane, where only the direction which the inertia, displacements and forces are measured change to the y axis.

Equation (4.7) is a fourth order differential equation, thus needing four boundary conditions (two at each end), for example,

- Free end: shear force and moments are null, $V=M=0$;
- Simple support: moment and vertical displacement are null, $M=u_z(u_y)=0$;
- Fixed support: vertical displacement and rotation are null, $u_z(u_y)=\frac{du_z(u_y)}{dx}=0$.

Analogously to the previous case, Eq. (4.7) is multiplied with arbitrary field $v(x)$ and integrated over the element. Trough integration by parts, the weak formulation becomes

$$[vV]_0^L-\left[\frac{dv}{dx}M\right]_0^L-\int_0^L\left(\frac{d^2v}{dx^2}EI_{yy}\frac{d^2u_z}{dx^2}-vq\right)dx=0\,, \tag{4.8}$$

where $M=-EI_{yy}\frac{d^2u_z}{dx^2}$ and $V=\frac{dM}{dx}$ are, respectively, the applied moment and shear force. Once again, for the case of bending in the xy plane, the only necessary changes in Eq. (4.8) are I_{zz} and u_y instead of I_{yy} and u_z.

Free Torsion

The free torsion equation of a beam subjected to a twisting load is given by

$$\frac{d}{dx}\left(GJ\frac{d\theta_x}{dx}\right)+m_x=0\,, \tag{4.9}$$

where G is the shear modulus of the material, J is the torsional moment of inertia, θ_x is the torsion and m_x is the distributed twisting load. The strong formulation is complete with the introduction of the two necessary boundary conditions, *e.g.*, $\theta(x_1) = \theta_1$ and $T(x_2) = GJ\frac{d\theta_x}{dx}|_{x_2} = T_2$.

As in the axial deformation case, Eq. (4.9) is a second order differential equation. Therefore, its strong and weak formulations are identical. The latter becomes

$$\left[vGJ\frac{d\theta_x}{dx}\right]_0^L - \int_0^L \left(\frac{dv}{dx}GJ\frac{d\theta_x}{dx} - vm_x\right) dx = 0\,. \tag{4.10}$$

4.1.4 Shape Functions

The shape functions will be necessary to formulate the element stiffness and mass matrices. These functions relate the displacement field for the beam, *i.e.*, the axial displacement $u_x(x)$, deflections $u_y(x)$ and $u_z(x)$ and angle of twist $\theta_x(x)$, with the nodal values of these quantities.

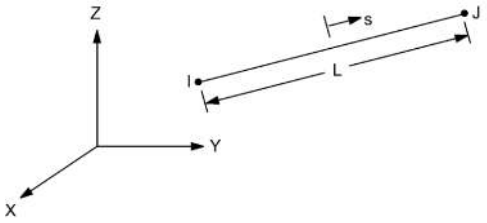

Figure 4.3: 3D beam element line, with local coordinate system [23].

Figure 4.3 represents the beam element with nodes I and J. The local coordinate s is related with the x direction in the global coordinate system by

$$s = \frac{2x - L}{L}\,. \tag{4.11}$$

The shape functions for this element are taken from the literature [23]. The axial displacement is linear in x while the transverse displacement is cubic in x. The shape functions can be disposed in matrix form as

$$\{u\} = [N]\{d\}\,, \tag{4.12}$$

where u is the vector of displacements, N is the matrix with the shape functions and d is the vector of nodal displacements. The full displacement field for the 3D beam element is given by the following

system of equations. The components of matrix N are listed in Table 4.1.

$$\begin{Bmatrix} u_x(x) \\ u_y(x) \\ u_z(x) \\ \theta_x(x) \end{Bmatrix} = \begin{bmatrix} N1_{u_x} & 0 & 0 & 0 & 0 & 0 & N2_{u_x} & 0 & 0 & 0 & 0 & 0 \\ 0 & N1_{u_y} & 0 & 0 & 0 & N3_{u_y} & 0 & N2_{u_y} & 0 & 0 & 0 & N4_{u_y} \\ 0 & 0 & N1_{u_z} & 0 & N3_{u_z} & 0 & 0 & 0 & N2_{u_z} & 0 & N4_{u_z} & 0 \\ 0 & 0 & 0 & N1_\theta & 0 & 0 & 0 & 0 & 0 & N2_\theta & 0 & 0 \end{bmatrix} \begin{Bmatrix} u_{x,I} \\ u_{y,I} \\ u_{z,I} \\ \theta_{x,I} \\ \theta_{y,I} \\ \theta_{z,I} \\ u_{x,J} \\ u_{y,J} \\ u_{z,J} \\ \theta_{x,J} \\ \theta_{y,J} \\ \theta_{z,J} \end{Bmatrix} \tag{4.13a}$$

$$\begin{Bmatrix} \theta_y(x) \\ \theta_z(x) \end{Bmatrix} = \begin{Bmatrix} \frac{du_z}{dx} \\ \frac{du_y}{dx} \end{Bmatrix} \tag{4.13b}$$

$N1_{u_x} = \frac{1}{2}(1-s)$	$N1_{u_y} = \frac{1}{2}\left(1 - \frac{s}{2}\left(3-s^2\right)\right)$	$N1_{u_z} = \frac{1}{2}\left(1 - \frac{s}{2}\left(3-s^2\right)\right)$	$N1_\theta = \frac{1}{2}(1-s)$
$N2_{u_x} = \frac{1}{2}(1+s)$	$N2_{u_y} = \frac{1}{2}\left(1 + \frac{s}{2}\left(3-s^2\right)\right)$	$N2_{u_z} = \frac{1}{2}\left(1 + \frac{s}{2}\left(3-s^2\right)\right)$	$N2_\theta = \frac{1}{2}(1+s)$
	$N3_{u_y} = \frac{L}{8}(1-s^2)(1-s)$	$N3_{u_z} = -\frac{L}{8}(1-s^2)(1-s)$	
	$N4_{u_y} = -\frac{L}{8}(1-s^2)(1+s)$	$N4_{u_z} = \frac{L}{8}(1-s^2)(1+s)$	

Table 4.1: Shape function matrix components.

4.1.5 Element Stiffness and Mass Matrices

A formal procedure will be followed to formulate the element stiffness and mass matrices, based on potential and kinetic energy.

The strain vector for this element includes axial strain, curvatures and twist angle which can be computed by

$$\begin{Bmatrix} \epsilon_x(x) \\ \kappa_z(x) \\ \kappa_y(x) \\ \theta_x(x) \end{Bmatrix} = \begin{bmatrix} \frac{\partial}{\partial x} & 0 & 0 & 0 \\ 0 & \frac{\partial^2}{\partial x^2} & 0 & 0 \\ 0 & 0 & \frac{\partial^2}{\partial x^2} & 0 \\ 0 & 0 & 0 & \frac{\partial}{\partial x} \end{bmatrix} [N]\{d\} = [B]\{d\}\,, \tag{4.14}$$

where B is the strain-displacement matrix. The stress vector is also slightly modified to include the axial force, bending moment in the two symmetric planes and torsional moment, *i.e.*,

$$\begin{Bmatrix} N_x \\ M_z \\ M_y \\ M_x \end{Bmatrix} = \begin{bmatrix} EA & 0 & 0 & 0 \\ 0 & EI_{zz} & 0 & 0 \\ 0 & 0 & EI_{yy} & 0 \\ 0 & 0 & 0 & GJ \end{bmatrix} \begin{Bmatrix} \epsilon_x(x) \\ \kappa_z(x) \\ \kappa_y(x) \\ \theta_x(x) \end{Bmatrix} = [D]\{\epsilon\}\,, \tag{4.15}$$

where N_x is the axial force along the x axis and (M_x, M_y, M_z) are the components of the (bending and torsion) moments.

The potential energy of the finite element is given by

$$V = \frac{1}{2}\int_\Omega \{\sigma\}^T\{\epsilon\}d\Omega - \int_\Omega \{F_v\}^T\{u\}d\Omega - \int_S \{F_s\}^T\{u\}dS\,, \tag{4.16}$$

where Ω and S are, respectively, the element domain and surface, while $\{F_v\}$ and $\{F_s\}$ represent the volume and surface forces, respectively. Equation (4.16) can be reformulated to account for the strain-displacement and shape function matrices as

$$V = \frac{1}{2}\{d\}^T\int_\Omega [B]^T[D][B]d\Omega\{d\} - \{d\}^T\int_\Omega [N]^T\{F_v\}d\Omega - \{d\}^T\int_S [N]^T\{F_s\}dS\,, \tag{4.17}$$

where $[K]_e$ is the stiffness matrix of the element, with the property of being symmetric, given by

$$[K]_e = \int_\Omega [B]^T[D][B]d\Omega \tag{4.18}$$

$$[K]_e = \begin{bmatrix} X & 0 & 0 & 0 & 0 & 0 & -X & 0 & 0 & 0 & 0 & 0 \\ & Y_1 & 0 & 0 & 0 & Y_2 & 0 & -Y_1 & 0 & 0 & 0 & Y_2 \\ & & Z_1 & 0 & -Z_2 & 0 & 0 & 0 & -Z_1 & 0 & -Z_2 & 0 \\ & & & S & 0 & 0 & 0 & 0 & 0 & -S & 0 & 0 \\ & & & & Z_3 & 0 & 0 & 0 & Z_2 & 0 & Z_4 & 0 \\ & & & & & Y_3 & 0 & -Y_2 & 0 & 0 & 0 & Y_4 \\ & & & & & & X & 0 & 0 & 0 & 0 & 0 \\ & & & & & & & Y_1 & 0 & 0 & 0 & -Y_2 \\ & & & & & & & & Z_1 & 0 & Z_2 & 0 \\ & & & & & & & & & S & 0 & 0 \\ & & & & & & & & & & Z_3 & 0 \\ & & & & & & & & & & & Y_3 \end{bmatrix}, \tag{4.19}$$

where

$$X = \frac{AE}{L}, \qquad Y_1 = \frac{12EI_z}{L^3}, \qquad Y_2 = \frac{6EI_z}{L^2}, \qquad Y_3 = \frac{4EI_z}{L}, \qquad Y_4 = \frac{2EI_z}{L},$$

$$S = \frac{GI_x}{L}, \qquad Z_1 = \frac{12EI_y}{L^3}, \qquad Z_2 = \frac{6EI_y}{L^2}, \qquad Z_3 = \frac{4EI_y}{L}, \qquad Z_4 = \frac{2EI_y}{L}\,.$$

While the stiffness matrix accounts for the elastic deformation, it is still necessary to consider the inertial properties of the element for a dynamic structural analysis. This is done by considering the kinetic energy of the finite element, given by

$$T = \frac{1}{2}\int_\Omega \rho\{\dot{u}\}^T\{\dot{u}\}d\Omega\,, \tag{4.20}$$

where ρ is the material density of the element. Once more, the kinetic energy equation can be rewritten as terms of the shape function matrix, *i.e.*,

$$\frac{1}{2}\{\dot{d}\}^T \int_\Omega \rho[N]^T[N]d\Omega\{\dot{d}\}\,, \tag{4.21}$$

where $[M]_e$ is the mass matrix of the element, which is a symmetric matrix, given by

$$[M]_e = \int_\Omega \rho[N]^T[N]d\Omega \tag{4.22}$$

$$[M]_e = \begin{bmatrix} X_1 & 0 & 0 & 0 & 0 & 0 & X_2 & 0 & 0 & 0 & 0 & 0 \\ & Y_1 & 0 & 0 & 0 & Y_2 & 0 & -Y_1 & 0 & 0 & 0 & Y_2 \\ & & Z_1 & 0 & -Z_2 & 0 & 0 & 0 & -Z_1 & 0 & -Z_2 & 0 \\ & & & S_1 & 0 & 0 & 0 & 0 & 0 & S_2 & 0 & 0 \\ & & & & Z_3 & 0 & 0 & 0 & Z_2 & 0 & Z_4 & 0 \\ & & & & & Y_3 & 0 & -Y_2 & 0 & 0 & 0 & Y_4 \\ & & & & & & X_1 & 0 & 0 & 0 & 0 & 0 \\ & & & & & & & Y_1 & 0 & 0 & 0 & -Y_2 \\ & & & & & & & & Z_1 & 0 & Z_2 & 0 \\ & & & & & & & & & S_1 & 0 & 0 \\ & & & & & & & & & & Z_3 & 0 \\ & & & & & & & & & & & Y_3 \end{bmatrix}, \tag{4.23}$$

where

$$X_1 = \frac{AL\rho}{3}, \quad X_2 = \frac{AL\rho}{6}, \quad Y_1 = \frac{13AL\rho}{35}, \quad Y_2 = \frac{11AL^2\rho}{210}, \quad Y_3 = \frac{AL^3\rho}{105}, \quad Y_4 = -\frac{AL^3\rho}{140},$$

$$S_1 = \frac{I_xL\rho}{3}, \quad S_2 = \frac{I_xL\rho}{6}, \quad Z_1 = \frac{13AL\rho}{35}, \quad Z_2 = -\frac{13AL^2\rho}{420}, \quad Z_3 = \frac{AL^3\rho}{105}, \quad Z_4 = -\frac{AL^3\rho}{140}.$$

The formulation for the mass matrix uses the same shape functions as the stiffness matrix and so it is called *Consistent Mass Matrix*. It also accounts for axial, flexural and torsional effects.

4.1.6 Structural Model Limitations

The variational method proves useful to compute the stiffness and mass matrices of the element. However, it has some limitations, particularly, the finite element model built of beam elements provides an exact solution when only force and/or moments are applied to its nodes. If a uniformly distributed load is also present, exact results are only approached as more elements are added in the finite element model [26]. Since in this work, the aerodynamic forces are computed in each node, this limitation can be overcome.

Moreover, this formulation is only valid for beams with constant cross-section properties. Since this model will be used to structurally represent a wing, some changes must be implemented in the code to

account for non-constant spanwise properties. In this case, ANSYS® [23] recommends using average values of area and moments of inertia as approximations. Therefore, the stiffness and mass matrices remain the same, except that an averaged area is used,

$$A_{av} = \left(A_1 + \sqrt{A_1 A_2} + A_2\right)/3\,, \tag{4.24}$$

and all three moments of inertia use averages of the form

$$I_{av} = \left(I_1 + \sqrt[4]{I_1^3 I_2} + \sqrt{I_1 I_2} + \sqrt[4]{I_1 I_2^3} + I_2\right)\Big/5\,, \tag{4.25}$$

where the subscripts refer to the element nodes as seen in Figure 4.2.

4.2 Program Development and Implementation

The CSD model was implemented in Matlab® language due to its strong matrix manipulation and useful plotting tools. The structure of the program was based on the procedures described in [27].

4.2.1 Input Data and Mesh Generation

The input parameters needed for the finite element analysis are:

- The number and coordinates of nodes in terms of the global coordinate system;
- The cross-section properties, *e.g.*, total area and moments of inertia;
- The material properties, *e.g.*, Young's modulus, shear modulus and density;
- Information for boundary conditions;
- The nodal forces relative to the global coordinate system.

The elements are computed with the coordinates of their nodes. A mesh with n elements has $n+1$ nodes. Figure 4.4 represents a mesh of a line with five beam elements, each one with a length of 0.2m.

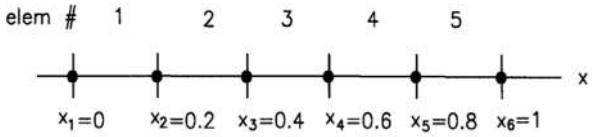

Figure 4.4: Mesh with 5 beam elements in the x direction.

4.2.2 Element Stiffness and Mass Matrices Computation and Assembly

The element stiffness and mass matrices are expressed in Eqs. (4.19) and (4.23), respectively. These expressions are function not only of the input parameters presented above but also the length of each element. Thereby, the length of each element is computed from the coordinate values of the nodes

associated with the element, stored in a 2D vector containing the coordinates in the global coordinate system.

Once the matrices are computed for each element, they need to be assembled in the global stiffness and mass matrices. In order to do this, the information where the element matrix is to be located in the global system matrix is needed. This is easily obtained from an array containing an index for each element with the information of the global position of its degrees of freedom (12 per element). In the end, a global matrix is obtained whose size is equal to the total number of degrees of freedom in the system (6 times the number of nodes).

4.2.3 Application of Boundary Conditions

Without applying constraints to the system of global equations, the matrices are singular and so they cannot be inverted in order to solve the static and dynamic problems. To overcome this problem, boundary conditions must be applied to one or more degrees of freedom in the stiffness and mass matrices.

The information for boundary conditions is provided in an array that contains the information of what degrees of freedom are to be constrained. For example, a beam with a fixed support at one of its ends, must have the first 6 degrees of freedom nullified. These constitute the primary boundary conditions.

The secondary boundary conditions are related to the loads applied on the structure, which must be located on its nodes in a finite element problem. Each node, in turn, has six degrees of freedom corresponding to three forces and three moments given in Cartesian coordinates. As a result, at each element the loads are inserted into a vector, given by

$$F_e = \begin{Bmatrix} F_{x,1} & F_{y,1} & F_{z,1} & M_{x,1} & M_{y,1} & M_{z,1} & F_{x,2} & F_{y,2} & F_{z,2} & M_{x,2} & M_{y,2} & M_{z,2} \end{Bmatrix}^T , \tag{4.26}$$

where F and M are, respectively, the applied forces and moments at each node and the subscripts refer to the axes of the local coordinate system and to the element nodes as seen in Figure 4.2.

In the end, each element load vector must be assembled into a global load vector in order to match the global stiffness and mass matrices ordering. For this, the same index array referred in the previous section is used.

4.2.4 Transformation from Local to Global Coordinate System

When analyzing the solution of a static or dynamic analysis, it is useful to obtain displacements and rotations in the global coordinate system whether the coordinate systems do not match. Figure 4.5 represents an element node with six degrees of freedom in local and global coordinate systems. The element coordinates are related to the global coordinates by

$$\{d_l\} = [T_R]\{d\} , \tag{4.27}$$

where d_l is the vector of displacements in element Cartesian coordinates and d is the vector of displacements in global Cartesian coordinates. The matrix T_R is called the *transformation or rotation matrix*,

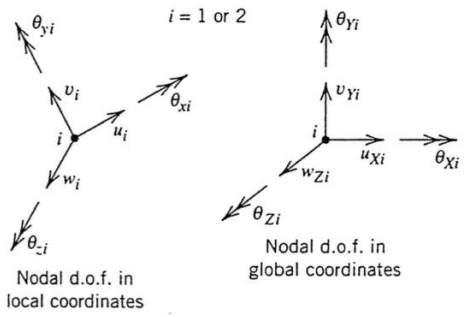

Figure 4.5: Node with degrees of freedom in local (left) and global (right) coordinate systems [26].

given by

$$[T_R] = \begin{bmatrix} T & 0 & 0 & 0 \\ 0 & T & 0 & 0 \\ 0 & 0 & T & 0 \\ 0 & 0 & 0 & T \end{bmatrix} . \tag{4.28}$$

According to [23], [T] is defined by

$$[T] = \begin{bmatrix} C_1C_2 & S_1C_2 & S_2 \\ (-C_1S_2S_3 - S_1C_3) & (-S_1S_2S_3 + C_1C_3) & S_3C_2 \\ (-C_1S_2C_3 + S_1S_3) & (-S_1S_2C_3 - C_1S_3) & C_3C_2 \end{bmatrix} , \tag{4.29}$$

where

$$S_1 = \frac{y_{i+1} - y_i}{L_{xy}} \qquad C_1 = \frac{x_{i+1} - x_i}{L_{xy}}$$

$$S_2 = \frac{z_{i+1} - z_i}{L} \qquad C_2 = \frac{L_{xy}}{L}$$

$$S_3 = sin(\theta_{pretwist}) \qquad C_3 = cos(\theta_{pretwist})$$

x_i, *etc.* = *x coordinate of node i, etc.*

$L_{xy} = \sqrt{(x_{i+1} - x_i)^2 + (y_{i+1} - y_i)^2}$, *projection of lenght onto x-y plane*

$\theta_{pretwist}$ = *orienation of element about x-axis, i.e., the pretwist angle*

In the end, the element stiffness and mass matrices in global coordinates become

$$[K] = [T_R]^T [K_l][T_R] , \tag{4.30}$$

$$[M] = [T_R]^T [M_l][T_R] , \tag{4.31}$$

where K_l and M_l are defined by Eq. (4.19) and (4.23), respectively.

4.3 Verification and Validation of CSD Program

The accuracy of the developed code will be verified with the aid of ANSYS® APDL [23], a program used to perform structural analysis. A cantilever beam with 10m in length, as shown in Figure 4.6, is selected to perform static and dynamic analyses. The cross-section and material properties of the beam are presented in Table 4.2, corresponding to a rectangular aluminium beam.

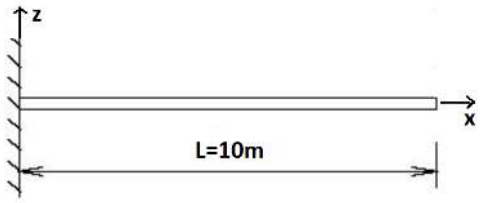

Figure 4.6: Cantilever beam.

Cross-section properties	Value
A	0.02 m^2
I_{yy}	1.6667E-05 m^4
I_{zz}	6.6667E-05 m^4
J	8.3E-05 m^4
Material properties	**Value**
E	70 GPa
G	27 GPa
ρ	2700 $Kg.m^{-3}$

Table 4.2: Beam cross-section and material properties.

The implemented code results will be compared with results from ANSYS® APDL, using BEAM4 elements [23] matching the beam element implemented as described in Section 4.1. BEAM4 is a legacy element still available for use in ANSYS®. It is uniaxial with tension, compression, torsion and bending capabilities, with six degrees of freedom at each node: translations in the nodal x, y and z directions and rotations about the same axis.

4.3.1 Static Linear Analysis

The static analysis of a beam solves the equilibrium equation, given in matrix form as

$$[K]\{d\} = \{F\}\,, \tag{4.32}$$

where K is the global assembled stiffness matrix, d is the vector of nodal displacements and rotations and F is the vector of applied nodal forces, all in global coordinates.

A first analysis was performed to study the convergence of the tip displacement of the cantilever beam with mesh refinement. The beam is subjected to an applied force $F_z = 1000N$ at the tip, in the positive z direction. The results obtained are present in Table 4.3 alongside a comparison with an identical analysis performed in ANSYS® APDL. The differences are relative to the obtained results from ANSYS® APDL.

As it can be seen in Table 4.3, the displacements converge very fast for both the implemented code and ANSYS® APDL. It can be concluded that, comparing with BEAM4, the results are the same except for a mesh with 2000 elements, where the relative difference is only 0.0035%. That is expected since the implemented code is based on this element. Figure 4.7 represents graphically the beam displacement

Elements	1	5	10	25	50	100	1000	2000
Matlab® Code	0.28571	0.28571	0.28571	0.28571	0.28571	0.28571	0.28571	0.28571
ANSYS® BEAM4	0.28571	0.28571	0.28571	0.28571	0.28571	0.28571	0.28571	0.28570
Relative Difference (%)	0.00000	0.00000	0.00000	0.00000	0.00000	0.00000	0.00000	0.00350

Table 4.3: Convergence study of beam tip vertical displacement and comparison with ANSYS® APDL.

with the same load case and a mesh with 100 elements.

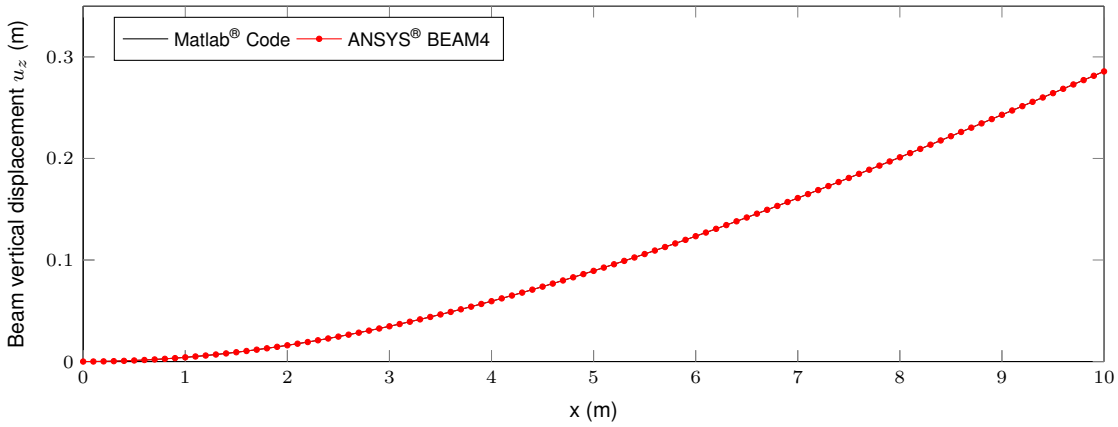

Figure 4.7: Beam displacement with applied force at the beam tip and comparison with ANSYS® APDL.

To verify the results of the implemented finite element code, different load cases were also tested. They are listed in Table 4.4, where all forces and moments are applied at the tip of the cantilever beam. A total of 100 finite elements were used for both analyses. As it can be seen in Table 4.5, the results obtained show differences which are very low for all tested load cases.

Case	**Load Type**	**Value**
1	F_x	1000 N
2	F_y	5000 N
3	$F_z; F_y$	1000 N; 1000 N
4	M_x	10000 N.m
5	M_y	-5000 N.m

Table 4.4: Load cases for static analysis.

4.3.2 Transient Linear Analysis

In the transient analysis, the equation of motion at time t is

$$[M]\{\ddot{d}\}^t + [K]\{d\}^t = \{F\}^t\,, \tag{4.33}$$

where the global assembled mass matrix M is added to account for inertial forces. To perform a time-dependent analysis, Eq. (4.33) needs to be discretized in the time domain.

There are many integration techniques that can be applied, which can be found in the literature [28]. In this work, the *Implicit Newmark Method* is selected, which is an implicit scheme. Here, time is

Displacements/Rotations	$\mathbf{u_x(m)}$	$\mathbf{u_y(m)}$	$\mathbf{u_z(m)}$	$\theta_\mathbf{x}\mathbf{(rad)}$	$\theta_\mathbf{y}\mathbf{(rad)}$	$\theta_\mathbf{z}\mathbf{(rad)}$
Case 1						
Matlab® Code	7.1429E-6	0.00000	0.00000	0.00000	0.00000	0.00000
ANSYS® BEAM4	7.1429E-6	0.00000	0.00000	0.00000	0.00000	0.00000
Relative Difference (%)	0.00000	0.00000	0.00000	0.00000	0.00000	0.00000
Case 2						
Matlab® Code	0.00000	0.35714	0.00000	0.00000	0.00000	0.05357
ANSYS® BEAM4	0.00000	0.35714	0.00000	0.00000	0.00000	0.05357
Relative Difference (%)	0.00000	0.00000	0.00000	0.00000	0.00000	0.00000
Case 3						
Matlab® Code	0.00000	0.07143	0.28571	0.00000	-0.04286	0.01071
ANSYS® BEAM4	0.00000	0.07143	0.28571	0.00000	-0.04286	0.01071
Relative Difference (%)	0.00000	0.00000	0.00000	0.00000	0.00000	0.00000
Case 4						
Matlab® Code	0.00000	0.00000	0.00000	0.04560	0.00000	0.00000
ANSYS® BEAM4	0.00000	0.00000	0.00000	0.04560	0.00000	0.00000
Relative Difference (%)	0.00000	0.00000	0.00000	0.00000	0.00000	0.00000
Case 5						
Matlab® Code	0.00000	0.00000	0.21429	0.00000	-0.04286	0.00000
ANSYS® BEAM4	0.00000	0.00000	0.21428	0.00000	-0.04286	0.00000
Relative Difference (%)	0.00000	0.00000	0.004667	0.00000	0.00000	0.00000

Table 4.5: Static linear analysis results and comparison with ANSYS® APDL.

discretized into small elements called time steps. The main difference between an explicit and implicit scheme resides in the time step used to calculate the quantities, *i.e*, based on current (implicit) or previous (explicit) time step. Therefore, for each iteration, an explicit scheme is more efficient compared to the implicit scheme. However, the first requires very small time steps (and so, many iterations) to be stable, whereas the latter does not. For long intervals of time, an implicit scheme may be more efficient overall than an explicit scheme.

The complete algorithm using the Newmark integration scheme is presented in Table 4.6. The parameters α and δ are used to obtain integration accuracy and stability and, in order to be stable, the scheme requires $\delta \geq 0.50$ and $\alpha \geq 0.25(0.5 + \delta)^2$.

In order to test the capabilities of the implemented code for the transient analysis, a load case is tested, with $F_z = 1000N$ and $M_x = 1000N.m$. A time step size of 0.001 s was chosen with time integration parameters $\alpha = 0.25$ and $\beta = 0.5$. For this analysis, 10 finite elements were chosen.

Figures 4.8(a) and 4.8(b) represent the transient response of the beam subjected to the load case chosen. A comparison with results from ANSYS® APDL, using element type BEAM4, was employed. It can be concluded that the vertical displacement results were perfectly matched in both cases.

On the other hand, the torsional rotation results present a slight deviation. Furthermore, it was spotted that the rotation movement had a very high frequency which made impossible a direct comparison within the interval of time of 5 s. As a result, the torsional rotation response is only plotted over 0.1 s. However, the frequency and mean value are identical when comparing the results from both analyses.

A. *Initial calculations*:

1. Input stiffness matrix K and mass matrix M.
2. Initialize vectors of displacement d^0, velocity $\dot{d}^0$ and acceleration $\ddot{d}^0$.
3. Select time step Δt and parameters α and β and compute integration constants: $a_0 = \frac{1}{\alpha \Delta t^2}$, $a_1 = \frac{1}{\alpha \Delta t}$, $a_2 = \frac{1}{2\alpha} - 1$, $a_3 = \Delta t(1-\delta)$ and $a_4 = \delta \Delta t$
4. Compute effective stiffness matrix $K_{eff} = K + a_0 M$.

B. *For each time step*:

1. Compute effective loads at time $t + \Delta t$: $F_{eff}^{t+\Delta t} = F^{t+\Delta t} + M(a_0 d^t + a_1 \dot{d}^t + a_2 \ddot{d}^t)$.
2. Solve for displacements at time $t + \Delta t$: $d^{t+\Delta t} = K_{eff}^{-1} F_{eff}^{t+\Delta t}$.
3. Solve for accelerations at time $t + \Delta t$: $\ddot{d}^{t+\Delta t} = a_0(d^{t+\Delta t} - d^t) - a_1 \dot{d}^t - a_2 \ddot{d}^t$
4. Solve for velocities at time $t + \Delta t$: $\dot{d}^{t+\Delta t} = \dot{d}^t + a_3 \ddot{d}^t + a_4 \ddot{d}^{t+\Delta t}$.

Table 4.6: Transient solution with steps using implicit Newmark method [28].

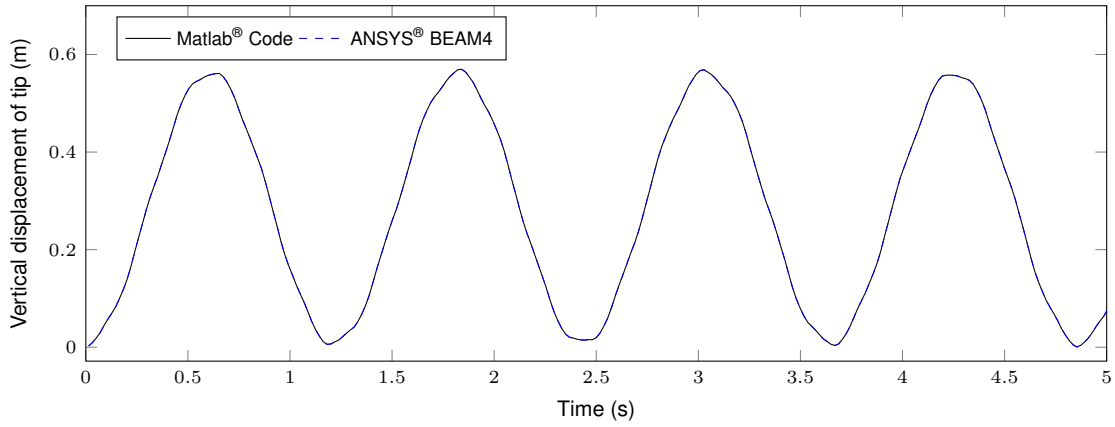

(a) Vertical displacement of beam tip node.

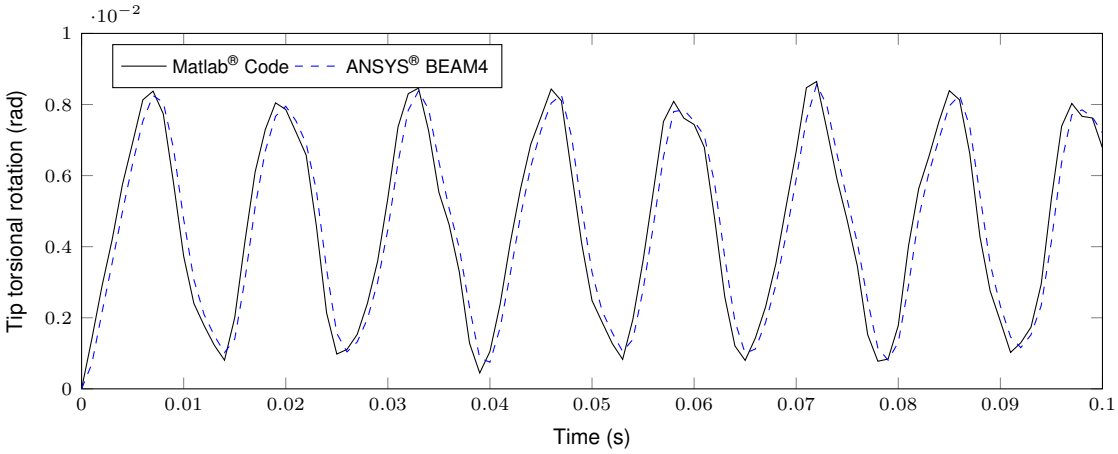

(b) Torsional rotation of beam tip node.

Figure 4.8: CSD transient numerical results and comparison with ANSYS® APDL.

4.3.3 Modal Linear Analysis

For the case of free-vibrations, there are no forces applied on the structure and Eq. (4.33) becomes

$$[M]\{\ddot{d}\} + [K]\{d\} = 0\,, \tag{4.34}$$

where $\{\ddot{d}\} = -\omega^2\{d\}$, with w being the natural frequency. Thereby, the equation of dynamic equilibrium results in an eigenvalue and eigenvector problem, yielding

$$[K]\{d\} = \omega^2[M]\{d\}\,. \tag{4.35}$$

A modal analysis was performed and the results were used to validate the structural model. For this, a prototype high aspect ratio wing that has been extensively reported in the literature, and is present in the paper from Patil *et al.* [29], is modeled. The structural model used is compatible with the one dimensional beam model used in this thesis and so it is considered suitable for validation of the results obtained by the developed program. Table 4.7 presents the input structural data.

Half span	16 m
Chord	1 m
Axial rigidity EA	3E7 N m^2
Bending rigidity EI_{yy} (flapwise)	2E4 N m^2
Bending rigidity EI_{zz} (chordwise)	4E6 N m^2
Torsional rigidity GJ	1E4 N m^2

Table 4.7: Wing equivalent beam model data [29] used to perform modal analysis.

In that paper, the authors present exact results for frequencies of an equivalent beam with torsion, flapwise bending and chordwise bending. Therefore, the first five natural frequencies were extracted and compared with the same ones obtained in [29]. In this analysis, the beam was discretized with 10 finite elements. The results are organized in Table 4.8.

	Matlab® Code	**Patil *et al.* [29]**	**Relative Difference (%)**
1st flapwise bending	2.243 rad/s	2.243 rad/s	0.000
2nd flapwise bending	14.057 rad/s	14.056 rad/s	0.007
3rd flapwise bending	39.369 rad/s	39.356 rad/s	0.033
1st torsion	31.081 rad/s	31.046 rad/s	0.113
1st chordwise bending	31.727 rad/s	31.718 rad/s	0.028

Table 4.8: Equivalent beam first five natural frequencies calculated with developed code and compared to results from [29].

All the frequencies are very similar with relative differences below 1%. Adding the good results from the previous analyses, it is concluded that the structural model developed is accurate enough to perform aeroelastic analyses.

Chapter 5

Wing Parametrization and Computation of Structural Properties

The aim of this work is to perform aeroelastic analysis and optimization of a subsonic wing. Therefore, the wing must be defined by parameters which, in turn, influence the numerical results. In this chapter, the necessary input parameters will be presented, as well as the mathematical model used to compute the cross-section structural properties of the equivalent beam model described in Chapter 4.

5.1 Input Parameters Description

The following data will need to be provided by the user to compute the wing geometric parameters and the beam structural properties and perform a complete aeroelastic analysis:

1. Description of wing external shape, defined by:
   (a) wing span;
   (b) chord, sweep angle, dihedral angle, twist angle along the span of the wing;
   (c) angle of attack;
   (d) section airfoil geometry distribution along the wing.
2. Description of wing internal structure, defined by:
   (a) thickness of the wing skin;
   (b) placement of shear webs within the wing;
   (c) thickness of the shear webs within the wing.
3. Description of material properties, which include:
   (a) elastic and shear modulus;
   (b) density.

In general, the wing shape is defined using parameters and a selected airfoil must be discretized with points in order to define the chordwise panels used by the fluid solver and to compute the structural properties of the wing. Moreover, the internal wing structure comprises the upper and lower surfaces of the wing and one or more shear webs (spars) across the sections. Finally, different materials can coexist within the wing. However, only isotropic materials are supported in this work. Tables A.1–A.4, found in Appendix A, describe in detail all the required inputs.

5.2 Coordinate Systems

Before advancing to the calculation of structural properties, it is advantageous to understand the different coordinate systems used by the developed program:

- *Global Coordinate System*: This is the global coordinate system, which does not ever move. The origin is located at the intersection of the wing elastic axis (shear center) and the wing root (see Figure 5.1). The positive *x* direction points in the downstream direction of the nominal free stream. The positive *y* direction is orthogonal to global *x*-*z* axes. The positive *z* direction points vertically upward, opposite to the direction of gravity.

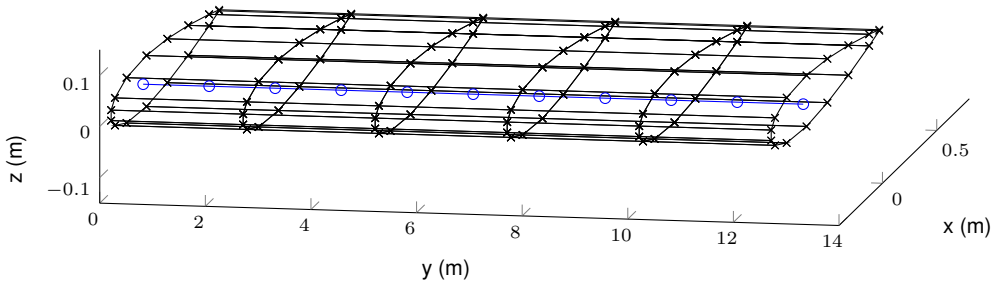

Figure 5.1: Global coordinate system.

- *Beam Coordinate System*: This system is local to the equivalent beam and moves with it. The origin is the same as the global coordinate system. The positive *x* direction points in the direction of the axial axis of the beam, which corresponds to the wing elastic axis (shear center of the airfoil). The positive *y* direction points in the direction of the airfoil trailing edge parallel with the chord line. The positive *z* direction is orthogonal to *x*-*y* axes. In a first stage, the solution (nodal displacements and rotations) is obtained in this local coordinate system, before being translated to the global coordinate system with the aid of the transformation matrix (Eq. (4.29)). This coordinate system is illustrated in Figure 5.2.

- *Airfoil Reference Coordinate System*: This coordinate system is used to discretize the airfoil, given a set of coordinates. The shear center and, consequently, the structural properties are computed in this coordinate system before being translated to the beam coordinate system. The origin is set at the leading edge of the airfoil. The positive *x* direction points in the direction of the airfoil trailing edge parallel with the chord line. The positive *y* direction makes a 90° angle with the positive *x*

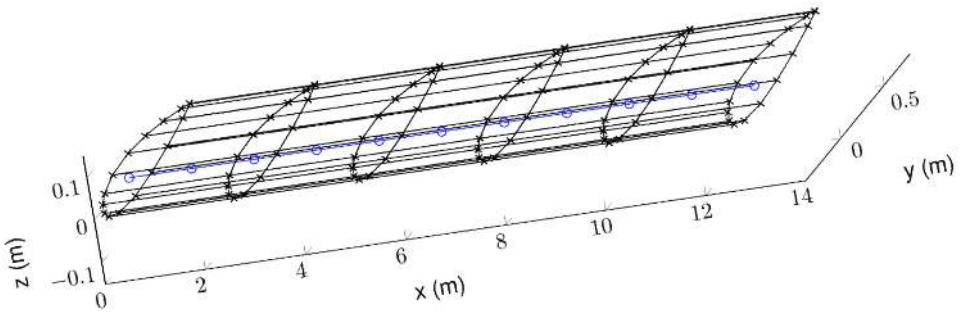

Figure 5.2: Beam coordinate system.

direction. The positive *z* direction is orthogonal to *x*-*y* axes. This coordinate system is illustrated in Figure 5.4.

5.3 Computation of Cross-Section Properties

In order to compute the cross-section properties of the wing, that is, the axial stiffness EA, the bending stiffness EI_{yy}, the bending stiffness EI_{zz} and the torsional stiffness GJ, applied in Eq. (4.19), a mathematical model was developed whose steps are present in Figure 5.3.

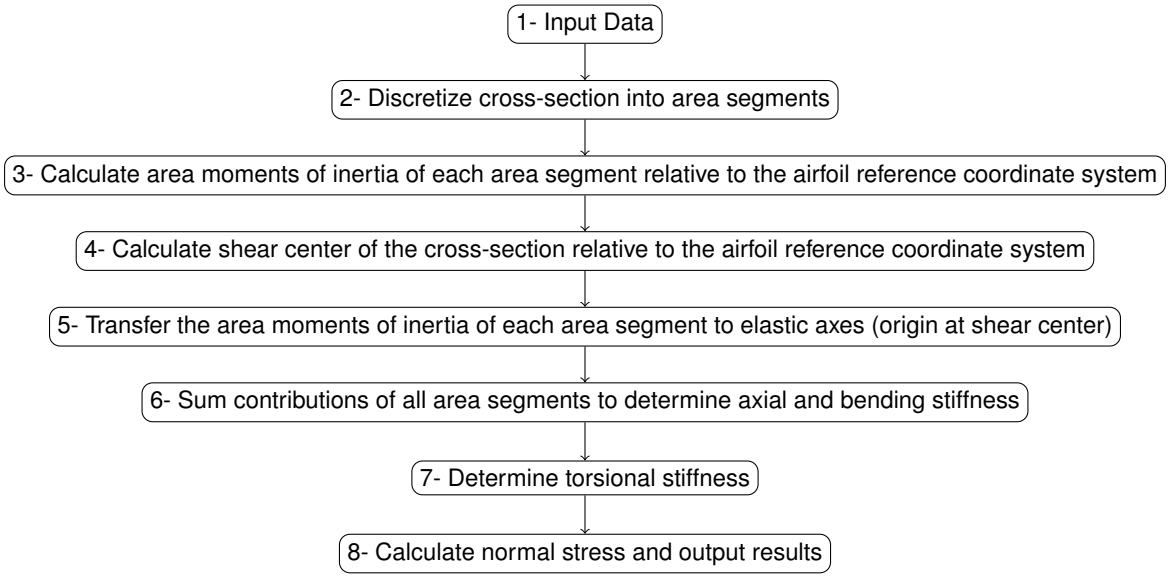

Figure 5.3: Flow chart of the mathematical model to compute structural properties.

The several steps shown in Figure 5.3 are briefly explained next.

1) Input Data

The model requires cross-sectional external shape (chord and airfoil coordinates), internal structure configuration (thickness and location of shear webs) and material engineering constants as inputs. This data has been reviewed and described in Section 5.1.

2) Discretize cross-section into area segments

In this step, the cross-section components (upper and lower surfaces and shear webs) are discretized into many area segments. Figure 5.4 illustrates a typical airfoil with the external surface discretized with 40 area segments and both shear webs discretized with 4 area segments.

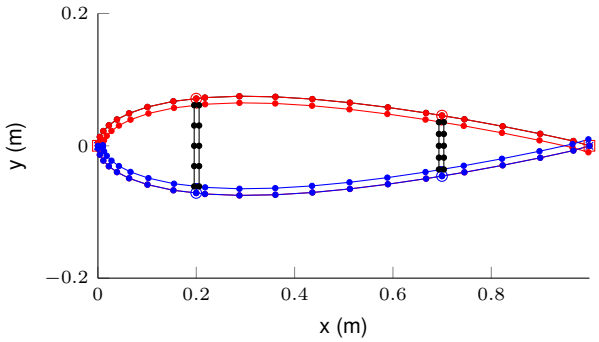

Figure 5.4: Discretization of a typical airfoil with two shear webs. Red: upper surface. Blue: lower surface. Black: shear webs.

3) Calculate area moments of inertia of each area segment relative to the airfoil reference coordinate system

The area moments of inertia of each area segment with respect to the airfoil reference coordinate system (the xy axes in Figure 5.4) can be calculated using an integration scheme [30]:

$$I_{xx}^{seg} = \int y^2 dxdy\,, \tag{5.1}$$

$$I_{yy}^{seg} = \int x^2 dxdy\,, \tag{5.2}$$

$$I_{xy}^{seg} = \int xydxdy\,, \tag{5.3}$$

where I_{xx}^{seg} and I_{yy}^{seg} are the area moment of inertia about x axis and y axis respectively, and I_{xy}^{seg} is the product of inertia.

4) Calculate shear center of the cross-section relative to the airfoil reference coordinate system

The shear center of a section is the point through which shear loads produce no twisting. Figure 5.5 illustrates the position of the shear center of a typical airfoil without shear webs. To determine the coordinates ξ and η (referred to the origin of the airfoil reference coordinate system) of the shear center S of a closed section, one applies arbitrary loads S_x and S_y through S, calculate the distribution of shear flow q_s due to the shear loads and equate internal and external moments.

In the case of a closed thin-walled cross-section, it is assumed that the shear stress τ evenly distributes across the thickness of the boundaries. The product of the shear stress τ and the thickness t refers to shear flow [7]:

$$q = \tau t\,. \tag{5.4}$$

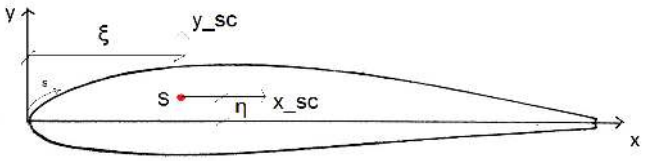

Figure 5.5: Shear center of a typical airfoil.

The shear flow distribution in a closed section loaded through its shear center is given by

$$q_s = q_b + q_{s,0}\,, \tag{5.5}$$

where q_b is the ”open” or ”basic” shear flow, supposing that the closed section is ”cut” at the origin point, hence producing an ”open” section and $q_{s,0}$ is the value of shear flow at the cut. As demonstrated in [7], the ”basic” shear flow q_b is given by

$$q_b = -\left(\frac{S_x I_{xx} - S_y I_{xy}}{I_{xx} I_{yy} - I_{xy}^2}\right)\int_0^s txds - \left(\frac{S_y I_{yy} - S_x I_{xy}}{I_{xx} I_{yy} - I_{xy}^2}\right)\int_0^s tyds\,, \tag{5.6}$$

where s is a reference coordinate system local to the section boundaries, originated at the same point where the section was ”cut”, S_x and S_y are the arbitrary applied shear loads, I_{xx}, I_{yy} and I_{xy} are the sum of area moments of inertia of each area segment of the section and t is the thickness of the section boundaries.

Assuming the shear loads are applied at the shear center, so that no twist is produced, the shear flow at the cut $q_{s,0}$ is given by

$$q_{s,0} = -\frac{\oint (q_b/Gt)ds}{\oint ds/Gt}\,, \tag{5.7}$$

where G is the shear modulus of the material of the section boundaries.

Finally, equating internal and external moments, the coordinates of the shear center ξ and η are calculated from

$$S_x\eta - S_y\xi = \oint pq_b ds + 2Aq_{s,0}\,, \tag{5.8}$$

where p is the normal distance between a tangent line with respect to a point in the section boundaries and the origin of the airfoil reference coordinate system, and A is the total area enclosed by the midline of the section, such that

$$\oint pds = 2A\,. \tag{5.9}$$

Generalizing for the case of an N-cell wing section, Eq. (5.8) becomes

$$S_x\eta - S_y\xi = \sum_{R=1}^{N}\oint_R pq_b ds + \sum_{R=1}^{N} 2A_R q_{s,0,R}\,. \tag{5.10}$$

5) Transfer the area moments of inertia of each area segment to elastic axes (origin at shear center)

With the calculation of the position of the shear center, the calculated area moments of inertia of each area segment with respect to the airfoil reference coordinate system (step 3) needs to be transferred to the elastic axes, with origin at the shear center (see Figure 5.5). The axes x_{sc} and y_{sc} correspond, respectively, to the axes y and z of the beam coordinate system, used to calculate the displacements and rotations at each time step, before being transferred to the global coordinate system.

Therefore, using the parallel-axis theorem, the calculated area moments of inertia can be transferred to shear center (elastic) axes (x_{sc},y_{sc}) of the section as

$$I^{seg}_{xx,sc} = I^{seg}_{xx} - A^{seg}\eta^2\,, \tag{5.11}$$

$$I^{seg}_{yy,sc} = I^{seg}_{yy} - A^{seg}\xi^2\,, \tag{5.12}$$

where A^{seg} is the area segment, as illustrated in Figure 5.4.

6) Sum contributions of all area segments to determine axial and bending stiffness

The overall cross-sectional properties including axial stiffness EA and bending stiffness EI_y and EI_z, with respect to the beam coordinate system, are obtained by summing the contributions of all N area segments:

$$EA = \sum_{i=1}^{N} E^{seg,i} A^{seg,i}\,, \tag{5.13}$$

$$EI_{yy} = \sum_{i=1}^{N} E^{seg,i} I^{seg,i}_{xx,sc}\,, \tag{5.14}$$

$$EI_{zz} = \sum_{i=1}^{N} E^{seg,i} I^{seg,i}_{yy,sc}\,. \tag{5.15}$$

7) Determine torsional stiffness

Based on Eq. (5.4), a shear flow theory called *Bradt-Batho Shear Flow Theory* (BSFT) [7] is used to evaluate stresses and deformations in structures with closed thin-walled cross-section under torsion. The torsional stiffness GJ of the wing's section can be obtained with the aid of BSFT.

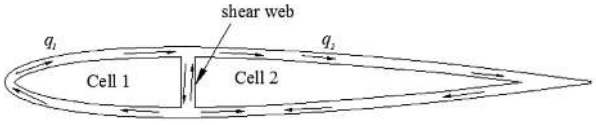

Figure 5.6: Typical airfoil with one shear web. When under torsion, a shear flow is produced [30].

Taking the cross-section with one shear web illustrated in Figure 5.6, the torsional moment M is expressed as [7]

$$M = 2(q_1 A^*_1 + q_2 A^*_2)\,, \tag{5.16}$$

where q_1 and q_2 are the shear flows of cells 1 and 2, respectively, and A_1^* and A_2^* are the area enclosed by the middle line of the wall boundaries of cells 1 and 2, respectively.

Assuming the twist angles of the two cells are the same, i.e., $\theta_1 = \theta_2 = \theta$, the twist angles of cells 1 and 2 are respectively expressed as

$$\delta_{11} q_1 + \delta_{12} q_2 - 2A_1^* \theta = 0\,, \tag{5.17}$$

$$\delta_{12} q_1 + \delta_{22} q_2 - 2A_2^* \theta = 0\,, \tag{5.18}$$

where δ is the warping flexibility given by

$$\delta_{11} = \oint_1 \frac{ds}{Gt}\,, \tag{5.19}$$

$$\delta_{22} = \oint_2 \frac{ds}{Gt}\,, \tag{5.20}$$

$$\delta_{12} = \delta_{21} = -\oint_{12} \frac{ds}{Gt}\,. \tag{5.21}$$

Writing Eqs. (5.16), (5.17) and (5.18) in matrix format, yields

$$M = 2 \begin{bmatrix} A_1^* & A_2^* \end{bmatrix} \begin{bmatrix} q_1 \\ q_2 \end{bmatrix}\,, \tag{5.22}$$

$$\begin{bmatrix} \delta_{11} & \delta_{12} \\ \delta_{21} & \delta_{22} \end{bmatrix} \begin{bmatrix} q_1 \\ q_2 \end{bmatrix} = 2\theta \begin{bmatrix} A_1^* \\ A_2^* \end{bmatrix}\,. \tag{5.23}$$

The torsional stiffness is given by

$$GJ = \frac{M}{\theta}\,. \tag{5.24}$$

Substituting Eqs. (5.22) and (5.23) into Eq. (5.24) yields

$$GJ = 4 \begin{bmatrix} A_1^* & A_2^* \end{bmatrix} \begin{bmatrix} \delta_{11} & \delta_{12} \\ \delta_{21} & \delta_{22} \end{bmatrix}^{-1} \begin{bmatrix} A_1^* \\ A_2^* \end{bmatrix}\,. \tag{5.25}$$

Equation (5.25) can be generalized for cross-sections with arbitrary shear webs. For example, for the cross-section represented in Figure 5.4, the matrices $[\delta]$ and $[A^*]$ become

$$[\delta] = \begin{bmatrix} \delta_{11} & \delta_{12} & 0 \\ \delta_{21} & \delta_{22} & \delta_{23} \\ 0 & \delta_{32} & \delta_{33} \end{bmatrix}\,, \tag{5.26}$$

$$[A^*] = \begin{bmatrix} A_1^* \\ A_2^* \\ A_3^* \end{bmatrix}\,. \tag{5.27}$$

8) Calculate equivalent stress and output results

Since the wing is approximated as a beam under axial tension/compression, biaxial bending and torsion at the same time, the equivalent stress can also be obtained. This property will be useful in the optimization problem studied in Chapter 9.

The stress vector can be calculated from Eq.(4.1) after the problem solution (displacements and rotations) is obtained. In the end, an equivalent stress can be computed taking into account the normal and shear stresses computed. One option is to use the *Von Mises equivalent stress* [31], given by

$$\sigma_{\text{VM}} = \sqrt{\frac{1}{2}\left[(\sigma_x - \sigma_y)^2 + (\sigma_y - \sigma_z)^2 + (\sigma_z - \sigma_x)^2\right] + 3\left(\tau_{xy}^2 + \tau_{yz}^2 + \tau_{zx}^2\right)}\,. \tag{5.28}$$

The stress vector components in Eq.(5.28) are calculated relative to the equivalent beam nodes, given the strains/displacements. However, it is possible to determine the location of the maximum stress in the actual wing cross-section at each node. In fact, the shear stress is easily calculated by Eq.(5.4) after the shear flow is obtained by Eq.(5.5) and knowing the thickness of the cross-section. On the other hand, the normal stress is the sum of each independent component from tension/compression and bending moments, which are determined by Eq.(4.15) relative to the nodal strains. Thus, the normal stress can be computed as

$$\sigma_x = \frac{N_x}{A} + \frac{M_z y}{I_{zz}} + \frac{M_y z}{I_{yy}}\,, \tag{5.29}$$

where x, y and z are the cross-section points coordinates given in the beam coordinate system. Therefore, it is concluded that the maximum and minimum stresses are located on the points whose distance from the shear center is larger, which is an important aspect for design projects.

After the calculations are done, the cross-sectional properties are output and used by the structural solver, including axial stiffness EA, bending stiffness EI_{yy} and EI_{zz} and torsional stiffness GJ. This properties are calculated with respect to the beam coordinate system.

Chapter 6

Fluid-Structure Interaction and Implementation

In Chapter 3, the governing equations for the fluid domain were presented alongside the computational method for the simulation of fluid dynamics. In Chapter 4, the structural computational model was developed, approximating the wing as a beam with its rigidity contained at the nodes. Now, to perform aeroelastic calculations, coupling both models is necessary. This chapter deals with the coupling and interaction between the two domains, also known as *Fluid-Structure Interaction* (FSI). Methods needed by the coupling phenomenon are introduced and possible enhancements are presented to achieve higher accuracy and less computational time during calculations.

6.1 Introduction to Numerical Coupling Methods

Bazilevs *et al.* [32] organized the range of FSI models in two classes: strongly-coupled (or monolithic) and loosely-coupled (or staggered).

In a monolithic model, the equations of fluid, structure and movement of the grid are solved simultaneously. This approach increases the accuracy of the solution but can be very difficult to perform for a large-scale problem. Farhat and Lesoinne [33] state that, when nonlinearity is present either in the fluid or structural equations (but mainly in the fluid), a monolithic scheme is in general computationally challenging, mathematically suboptimal and software-wise unmanageable.

Alternatively, the fluid and structural equations can be solved by a staggered procedure, which consists in the successive decoupled integrations of the structure and the fluid fields. Hence, each field is frozen during the time integration of the other field, which brings many advantages, such as the possibility of using existing schemes, programs and procedures for both separate fields. On the other hand, this kind of approach may not be stable and convergence issues may arise.

In this work, only staggered procedures will be considered, which are simpler and more common, and in Chapter 7 several aeroelastic tests will be performed on a 3D wing using the different coupling procedures presented in the current chapter for comparison.

A typical coupled fluid-structure analysis diagram is shown in Figure 6.1.

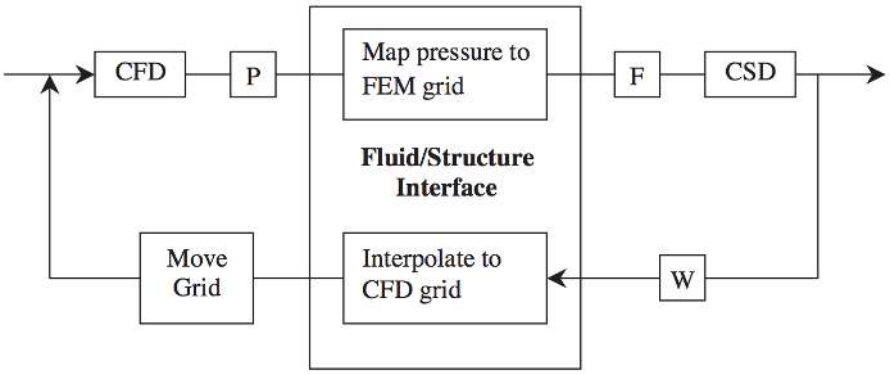

Figure 6.1: Coupled fluid-structure flow diagram [34].

As shown in the figure, due to the fluid flow pressures, forces appear on the wall boundaries of the fluid domain. All these forces are mapped to the structural nodes and the displacements are computed, which leads to the movement of the computational grid of the fluid. Hence, both the flow and structure act on each other.

The basic line of a staggered algorithm could be sketched as follows:

- For every time-step, the fluid pressures P are mapped to the structural nodes to obtain the aerodynamic forces F on the CSD grid;
- The structural displacements W due to the aerodynamic forces F are computed after time-integration of the structure field;
- The fluid grid after the current time-step is updated, which must satisfy the condition that both fluid and structural boundaries are matching along the interface;
- The fluid field is time-integrated and the aerodynamic forces at the beginning of the next time-step are computed.

6.2 FSI Coupling Methods

Piperno [35] classified the staggered coupling methods into two categories: *volume-continuous methods* and *volume-discontinuous methods*.

In the first kind of methods, both the fluid and structure boundaries are spatially matching, meaning near the interface, the whole volume is occupied either by the fluid or the structure. The algorithm can be understood as ”integrate the structure and then the fluid, and do it again...” [35]. However, as it will be demonstrated later, the stability of the global algorithm is limited because energy violations are induced.

The same author refers to the second methods as the symmetrical of the first, *i.e.*, the algorithm can be described as ”integrate the fluid and then the structure, and so on...”. The most significative difference between both methods is the matching condition on the interface between fluid and structure. While in

the first method, the fluid and structural boundaries are matched after each time-step, in the second there is no matching requirement. Consequently, in continuous methods, the information received by the fluid from the structure is *exact* (at a certain time one has the correct location of the structure) but *late*. On the other hand, in discontinuous methods, this information is only *predicted*, but at the *right time*. This can induce strong numerical errors at the interface in the second methodology. However, if the prediction of the next location of the structure is accurate, the matching of the interfaces will also be more accurate and the time-integration of the structure might be done with more accuracy because the pressure forces at the end of the time-step (t^{n+1}) are already known.

6.2.1 Volume-continuous Methods

In the following sections, two volume-continuous staggered algorithms will be described introducing possible enhancements to improve accuracy and efficiency.

Conventional Serial Staggered Algorithm

The most basic staggered method is referred to as the *Conventional Serial Staggered* (CSS) procedure by Farhat and Lesoinne [33] and it is outlined in Figure 6.2, where u denotes the structure state vector (nodal displacements), w is the fluid state vector, p denotes the fluid pressure, x represents the fluid grid position, the subscript n designates the n^{th} time step, and the equalities shown at the top hold on the fluid/structure interface boundary. This algorithm is a collocated scheme where at each cycle the fluid and structure solutions are evaluated at the same time-station.

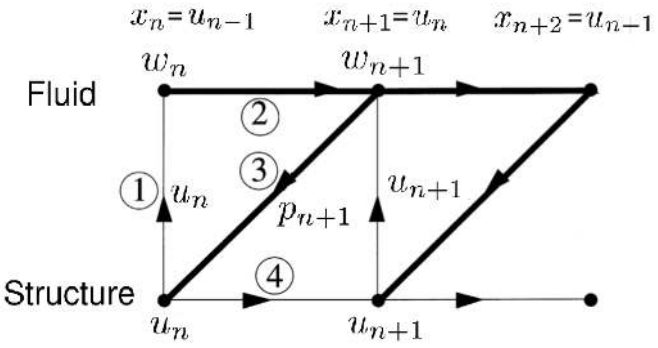

Figure 6.2: Conventional Serial Staggered (CSS) procedure [33].

The CSS algorithm, for one time integration from t^n to t^{n+1}, can be described as follows [33]:

- Assume one disposes of all computational values corresponding to the structure and fluid state vectors at the n^{th} time step, either by defining initial conditions at this time step or time-integrating the structure from t^{n-1} to $t^n = t^{n-1} + \Delta t_S$;
- Compute a new fluid grid x^{n+1} matching the structural boundaries by adding the structural displacements u^n to the current grid position $x^n = u^{n-1}$;
- Time-integrate the fluid from t^n to $t^{n+1} = t^n + \Delta t_S$ using a fluid time step $\Delta t_F = \Delta t_S$;

- Transfer the fluid pressure field P_F^{n+1} to the structure and compute the corresponding flow-induced structural load F^{n+1} with the method described in Section 6.5;
- Time-integrate the structure to advance it from t^n to $t^{n+1} = t^n + \Delta t_S$.

Usually, the fluid flow requires a finer temporal resolution than the structural vibration [33]. Therefore, the coupling time step Δt_S is dictated by the fluid solution accuracy, since this CSS procedure uses the same time step for both subsystems. In order to save CPU time in the overall simulation, this CSS procedure can be equipped with fluid subcycling, in which the next method consists.

Conventional Serial Staggered Algorithm with Fluid Subcycles

Subcycling the fluid computations can offer substantial computational advantages, including savings in the total simulation time because it reduces the overall number of structural integrations since the stability of the coupling method is dictated by the fluid time step. Thereby, one can still maintain a small enough time step for the fluid integration and, taking advantage of the subcycling, perform as many time steps as required to make up the total time step Δt_S. The CSS method equipped with fluid subcycling is illustrated in Figure 6.3.

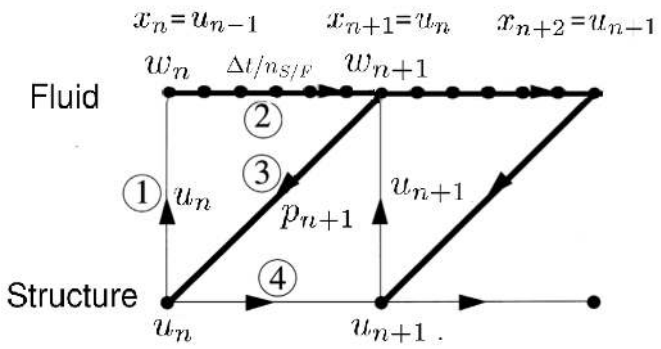

Figure 6.3: Conventional Serial Staggered (CSS) procedure with fluid subcycling [33].

The algorithm is identical to the CSS without fluid subcycling. The difference is in the fluid time-integration, where the number of fluid subcycles is given by

$$n_{S/F} = \frac{\Delta t_S}{\Delta t_F} \tag{6.1}$$

and the pressure field P_F^{n+1} is the average of the pressure fields computed at each subcycle as

$$P_F^{n+1} = \frac{1}{n_{S/F}} \sum_{k=1}^{n_{S/F}} P_{Fk} \,. \tag{6.2}$$

The algorithm for updating the fluid dynamic mesh when the fluid is subcycled requires special attention. The velocity of the fluid moving grid must remain constant and equal to $\dot{x} = (x^{n+1} - x^n)/\Delta t_S$, to satisfy the geometric conservation law (GCL) [36]. This requirement will be detailed later in this chapter, where the consistency and energy conservation are discussed.

6.2.2 Volume-discontinuous Methods

With the volume-continuous methods, important energy violations may be induced, limiting the stability of the global algorithm. One possible solution for this problem is the use of volume-discontinuous methods, introduced before. In the following subsections, some algorithms are presented with possible enhancements to improve accuracy and save computational time.

Serial Staggered Algorithm with Structural Predictor

This methodology, unlike the CSS, does not require that the fluid and the structural boundaries are matching after each time step. Therefore, a prediction for the global state of the structure after a time step is introduced and the fluid is time-integrated, assuming the fluid grid is matching the location of the structure that was predicted. A more precise sketch of this method is as follows:

- Assume one disposes of all computational values corresponding to the structure and fluid state vectors at the n^{th} time step, either by defining initial conditions at this time step or time-integrating the structure from t^{n-1} to $t^n = t^{n-1} + \Delta t_S$;
- Make a prediction for the global state of the structure at time t^{n+1};
- Compute a possible fluid grid x^{n+1} matching the location of the fluid/structure interface just predicted at time t^{n+1};
- Time-integrate the fluid from t^n to $t^{n+1} = t^n + \Delta t_S$ using a fluid time step $\Delta t_F = \Delta t_S$. Subcycling the fluid is an option;
- Transfer the fluid pressure field P_F^{n+1} to the structure and compute the corresponding flow-induced structural load F^{n+1} with the method described in Section 6.5;
- Time-integrate the structure to advance it from t^n to $t^{n+1} = t^n + \Delta t_S$.

At the end of a time step, continuity of the structural and fluid grid displacements at the interface is *a priori* not satisfied unless the structural predictor is perfect. Piperno [35] identifies two types of predictors:

$$\tilde{u}^{n+1} = u^n + \Delta t_S \dot{u}^n \,, \tag{6.3}$$

$$\tilde{u}^{n+1} = u^n + \Delta t_S (1.5\dot{u}^n - 0.5\dot{u}^{n-1}) \,. \tag{6.4}$$

Equation (6.3) is a linear and first-order predictor, while Eq. (6.4) is second-order accurate. These predictors will be used for comparison in the next chapter.

Serial Staggered Algorithm with Structural Predictor and Subiterations

The predictors in Eqs. (6.3) and (6.4) may present limited stability as a consequence of their uncoupled nature because the average acceleration during the previous time step has the same value in the current

time step. Thereby, this is equivalent to an assumption on the fluid pressure during the current time step. In order to eliminate this aspect, Piperno [35] suggests the use of subiterations (or coupled predictions), as follows:

1. At time t^n store the fluid state, the fluid grid and the structural state. Set *ipc*=0;
2. Compute a prediction of the structural displacement at time t^{n+1} according to (6.3) or (6.4);
3. Update the fluid mesh at time t^{n+1} matching the predicted displacement. Advance the fluid in time and compute the time-averaged fluid pressure and forces on the structure according to Eq. (6.2);
4. Time-integrate the structure until t^{n+1};
5. If $ipc < IPC$, use the structural displacement at time t^{n+1} as a prediction and reset all computational values to the values stored at step 1. Update $ipc = ipc + 1$ and go to step 3.

Here, *ipc* denotes the current subiteration while *IPC* represents the total number of subiterations used. The big disadvantage of this method is the higher computational cost inherent. In fact, the computation cost is *IPC* times bigger, since *IPC* steps of the regular volume-discontinuous method are done.

Improved Serial Staggered Algorithm

Another alternative volume-discontinuous method is proposed and studied by Farhat and Lesoinne [33], which is a subiteration-free staggered algorithm, that is as computationally complex as the CSS procedure but has a superior accuracy similar to those of a monolithic scheme or a staggered method using subiterations. This method is labeled as the *Improved Serial Staggered* (ISS) procedure and it is illustrated in Figure 6.4.

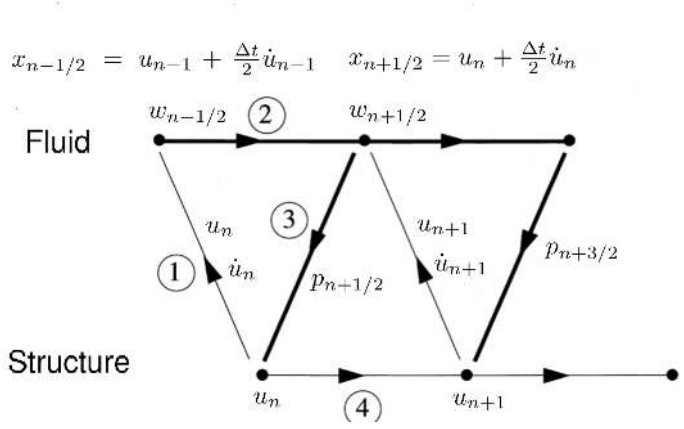

Figure 6.4: Improved Serial Staggered (CSS) procedure [33].

The ISS procedure can be described as follows [37]:

- Assume one disposes of all computational values corresponding to the structure state vector at the n^{th} time step, either by defining initial conditions at this time step or time-integrating the structure from t^{n-1} to $t^n = t^{n-1} + \Delta t_S$;

- Predict the structural displacement at time $t^{n+1/2}$ by

$$\tilde{u}^{n+1/2} = u^n + \frac{\Delta t}{2}\dot{u}^n \,; \tag{6.5}$$

- Update the fluid grid position $x^{n+1/2}$ to match the position that the structure would have if it were advanced by the predicted displacement $\tilde{u}^{n+1/2}$;
- Time-integrate the fluid subsystem from $t^{n-1/2}$ to $t^{n+1/2} = t^{n-1/2} + \Delta t_S$. Subcycling the fluid is an option;
- Transfer the fluid pressure field $P_F^{n+1/2}$ to the structure and compute the corresponding flow-induced structural load $F^{n+1/2}$ with the method described in Section 6.5;
- Time-integrate the structure to advance it from t^n to $t^{n+1} = t^n + \Delta t_S$.

This algorithm is noncollocated as it is constructed as a leap-frog scheme [33] where the fluid subsystem is always computed at half time-stations, while the structure subsystem is always computed at full time-stations, as shown in Figure 6.4.

6.3 Consistency and Energy Transfer Analysis

In this section, the requirements in terms of mathematical consistency are presented as well as an energy transfer analysis during the time-integration of both the structure and fluid subsystems, with application to the FSI models presented in this work.

6.3.1 Geometric Conservation Law

A sufficient condition for a numerical method for the solution of fluid problems on moving grids to be mathematically consistent is that it predicts exactly a uniform flow. Lesoinne and Farhat [36] demonstrated that this condition is only satisfied if the numerical scheme chosen for solving the fluid problem in time satisfy a discrete *Geometric Conservation Law* (GCL). In order to satisfy the GCL, it was proven that the velocity of the dynamic mesh must be computed as

$$\dot{x} = \frac{x^{n+1} - x^n}{\Delta t} \,. \tag{6.6}$$

6.3.2 Energy Conservation of Volume-continuous Methods

In this work, the fluid subsystem is time-integrated with the implicit backward-Euler scheme in Eq. (3.38). Therefore, the energy transferred during the time-interval $[t^n, t^{n+1}]$ from the fluid to the structure, as viewed by the fluid, can be evaluated as [38]

$$\Delta E_F^{n+1} = -\int_{t^n}^{t^{n+1}} f_F(t)\dot{x}(t)dt = -P_F^{n+1}(x^{n+1} - x^n) \,. \tag{6.7}$$

On the other hand, the structure subsystem employs the Newmark method presented in Chapter 4. Therefore, if the structural energy is defined as

$$E_S = \frac{1}{2}\dot{u}^T M \dot{u} + \frac{1}{2} u^T K u \,, \tag{6.8}$$

it follows from the Newmark scheme that the variation of the structural energy E_S, as viewed by the structure, during a time step Δt_S, assuming no external forces are applied on the structure, and according to [38], is given by

$$\Delta E_S^{n+1} = P_F^{n+1}(u^{n+1} - u^n) \,. \tag{6.9}$$

From Eqs. (6.7) and (6.9), it follows that the total energy variation using the volume-continuous methods presented in this chapter, namely, the CSS staggered procedure, is given by

$$\Delta E^{n+1} = P_F^{n+1}[(u^{n+1} - u^n) - (x^{n+1} - x^n)] \,. \tag{6.10}$$

Since the information received by the fluid from the structure is late, $x^{n+1} = u^n$, and u^{n+1} is computed only after P_F^{n+1} has been evaluated, it can be concluded that the volume-continuous methods do not conserve energy.

6.3.3 Energy Conservation of Volume-discontinuous Methods

In this case, the fluid grid position is updated with the predicted structural displacements at each time step. Hence, Eq. (6.7) becomes

$$\Delta E_F^{n+1} = -P_F^{n+1}(\tilde{u}^{n+1} - \tilde{u}^n) \,. \tag{6.11}$$

The structural energy variation, however, remains the same as in Eq. (6.9) because the structure is time-integrated in the same way, $\Delta E_S^{n+1} = P_F^{n+1}(u^{n+1} - u^n)$. If one writes ϵ^n for the mismatching error at time t^n,

$$\epsilon^n = u^n - \tilde{u}^n \,, \tag{6.12}$$

where u^n and $\tilde{u}^n$ stand for the exact and predicted displacement, respectively. The system total energy variation through one time step of this method is given by

$$\Delta E^{n+1} = P_F^{n+1}(\epsilon^{n+1} - \epsilon^n) \,. \tag{6.13}$$

If the matching error is small, then the global energy of the system will be conserved with a good accuracy. In fact, the order of magnitude of the energy error depends on the quality of the prediction. This characteristic induces the great flexibility of the method.

In the next sections some important methods needed for the coupling of the fluid and structure fields will be presented. This includes spacial discretization, mapping the fluid pressures/forces to the structural mesh and an extrapolation to update the fluid grid position at each time-step.

6.4 Spacial Discretization

As discussed in Chapter 4, the structural computational model in this work consists in modeling the wing as one dimensional straight beam which coincides with the wing elastic axis. It is assumed that the whole rigidity of the wing is concentrated along the beam. This beam model is suitable for bodies whose natural frequencies are close to those of beams with equivalent bending stiffness, *e.g.*, high aspect ratio wings with uniform material properties.

The structural nodes are located at the middle and at the limits of each ring of panels of the fluid grid, as shown in Figures 6.5 and 6.6. This option is justified with the necessity of mapping the fluid forces computed at the middle of the panels to the structural nodes, hence the position of the nodes at the middle of the ring, and the necessity of extrapolating the structural displacements to the CFD grid points, which corresponds to the panel corner points, hence the position of the nodes at the sides of each ring. Concerning these last nodes, their only role is to transfer the displacement to the CFD grid points. Thereby, no nodal forces are applied on them.

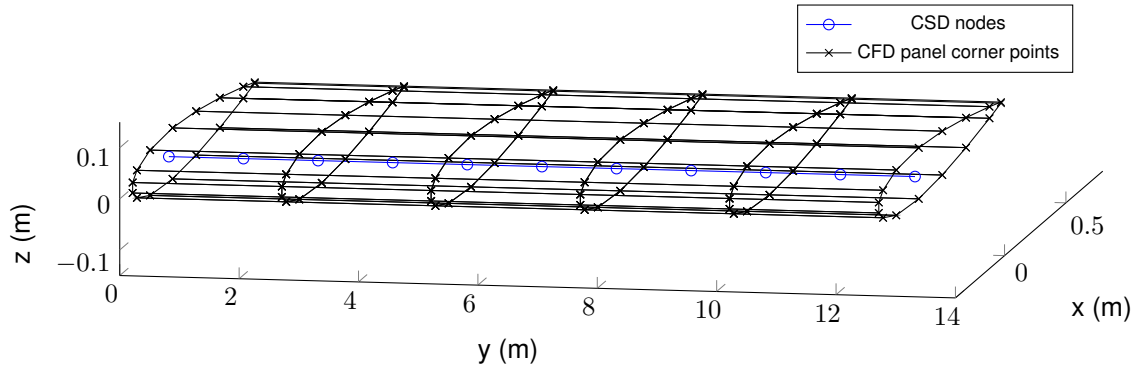

Figure 6.5: CFD grid: 16x5 panels, with representation of panel's corner points. CSD grid: beam with 10 elements and 11 nodes. The blue line is the elastic axis and corresponds to the equivalent 3D beam model.

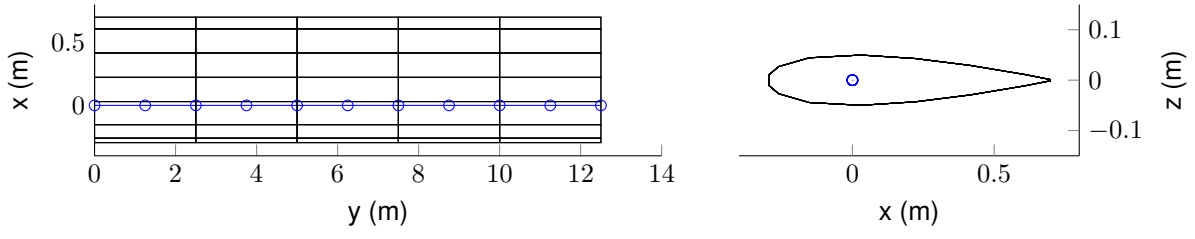

Figure 6.6: CFD grid and CSD grid. Left: Top view. Right: Side view. The structural nodes are placed on the mean surface (camber line) along the elastic axis.

The first node located at the wing root defines the zero displacement and rotation boundary condition, assuming the wing is perfectly attached to the fuselage and representing the intersection of the wing with the fuselage, also known as cantilever wing.

6.5 Fluid Forces at the Fluid-Structure Interface

The fluid dimensionless pressures in Eq. (3.38) need to be changed into forces and transferred to the structural nodes at the interface for solving the structural problem. As the pressures are collocated in the fluid model, the forces are assumed to be applied at the panels collocation points. Assuming the pressure is constant in a panel, multiplying it by the area and the dynamic pressure $0.5\rho V_\infty^2$ gives the total force in a panel. In Figure 6.7, a sketch of a structural node placed in the same vertical plane (corresponding to a arbitrary cross-section of the wing) as the collocation points of a certain ring of panels is shown, alongside the force vectors applied at each collocation point.

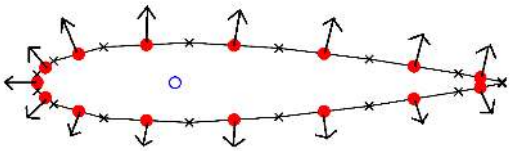

Figure 6.7: Fluid forces applied at each collocation point. The force vectors are not represented by their real orientation.

An orientation vector is computed for each panel to seek the components of the force vector in the global reference system (see Figure 6.5). Therefore, knowing the values of the force components at each collocation point, one needs to map them to the structural nodes. To do this, the equivalent force system is obtained as *D'Alembert's Principle* requires [39], *i.e.*, the pressure forces are mapped to the structural nodes and their respective moments are calculated, as shown in Figure 6.8.

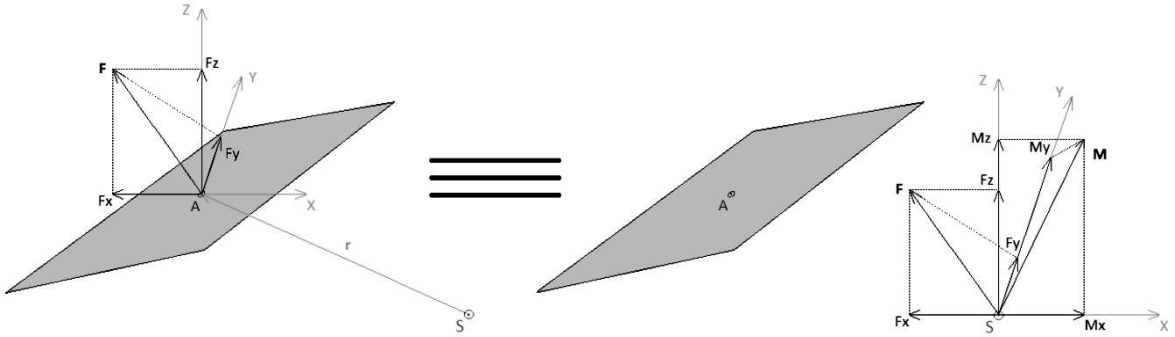

Figure 6.8: Schematics of the aerodynamic force applied on a panel (collocation point) and its equivalent force system on the nearby structural node.

Since Euler-Bernoulli beam theory was assumed, the beam cross-section remains constant and perpendicular to the axial axis. Hence, in this procedure, only the structural nodes that are in the same plane as the collocation points of one ring of panels receive the pressure forces. The remaining structural nodes (the ones located on the same plane as the panel corner points) are needed exclusively to extrapolate the displacements to the CFD grid points to move them. This approach will be presented in detail in the next section.

6.6 Moving Grid Extrapolation

In order to update the CFD grid at every time step, a linear extrapolation procedure was employed to transfer the displacements of the beam model to the original CFD grid, resulting in the new CFD surface mesh.

As explained before, since Euler-Bernoulli theory was assumed, the cross-sections of the beam remain unchanged. Therefore, the new positions of the CFD grid were obtained assuming a rigid link connection between the structural nodes positioned at the limits of each ring of panels and the respective panel corner points. The links are assumed to be perpendicular to the elastic axis of the wing.

Kamakoti and Shyy [34] used a similar approach to move the CFD grid during the aeroelastic analysis, using beam finite elements in the structural solver. To do this, a linear extrapolation procedure was employed to transfer the displacements from the beam model. Recalling Chapter 4, the displacements of the beam at any time step along the spanwise direction are given by

$$\{d\} = \begin{Bmatrix} u_x & u_y & u_z & \theta_x & \theta_y & \theta_z \end{Bmatrix}^T . \tag{6.14}$$

The displacement of a CFD panel corner point can be separated into three components: a translation component u_z, a translation component u_x and a rotation component θ_y. Figure 6.9 demonstrates this procedure.

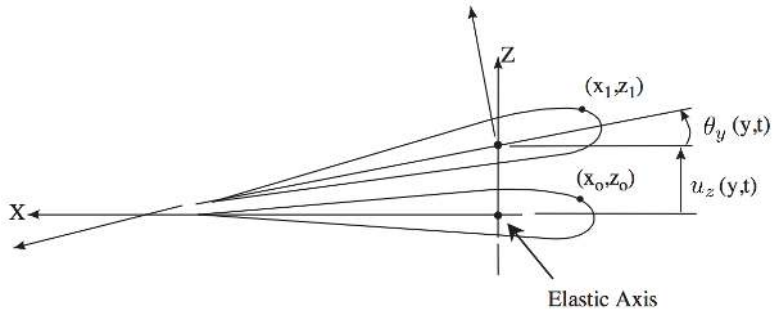

Figure 6.9: Extrapolation procedure to obtain the new location of the CFD grid points [34].

In Figure 6.9, the subscript 0 denotes the original location of the CFD grid panel corner points while the subscript 1 denotes the new location. Obtaining the structural solution and knowing the values of u_z and θ_y at each location on the spanwise direction and at each time step, the new location is obtained by

$$x_1 = x_0 cos(\theta_y) + z_0 sin(\theta_y) + u_x \,, \tag{6.15}$$

$$z_1 = z_0 cos(\theta_y) - x_0 sin(\theta_y) + u_z \,. \tag{6.16}$$

6.7 Code Validation

To validate the moving grid extrapolation and loads transferring algorithms, the paper by Patil and Hodges [40] was used as a case study. In this work, the authors study the effects of geometrical non-

linearities on the aeroelastic behavior of high-aspect ratio wings. Despite the focus being the nonlinear characterization, linear results are also presented in order to compare the two formulations.

As a result, the study involves a flexible wing with a speed of 25 m/s at an angle of attack of 10°. The structural properties of the wing are given in Table 6.1.

Wing Properties	
Half span	16 m
Chord	1 m
Spanwise elastic axis	50% chord
Mass per unit length	0.75 kg/m
Axial rigidity EA	3E7 N m^2
Bending rigidity EI_{yy} (flapwise)	2E4 N m^2
Bending rigidity EI_{zz} (chordwise)	5E6 N m^2
Torsional rigidity GJ	1E4 N m^2
Flight Condition	
Altitude	20 km
Air density	0.0889 kg/m^3

Table 6.1: Wing model input data required for performing aeroelastic static computations.

Figure 6.10 shows the steady state equilibrium solution obtained using the linear theory presented in [40] and the one obtained using the developed code. It is seen that the bending deformation is quite close between the two methods. The difference may be attributed mostly to the different aerodynamic models used, namely, the panel method employed in this framework and the doublet-lattice method used in the paper. Moreover, the data points regarding the published results were extracted from a plot image using proper software. Therefore, some misreads may be inherent to this process.

Overall, it is concluded that the transfer of the fluid loads into the structural mesh as well as the extrapolation to move the CFD grid points implemented in the code are working correctly.

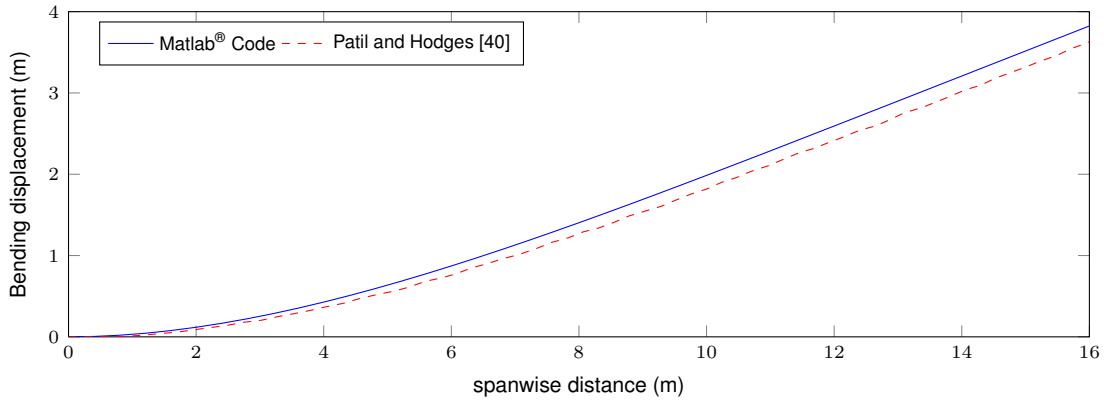

Figure 6.10: Wing static bending displacement at 25 m/s and angle of attack 10°.

Chapter 7

Benchmark of FSI Staggered Algorithms

In Chapter 6, two types of methods used to couple the fluid and structure domains were presented, namely, the *volume-continuous* and *volume-discontinuous* methods. In general, the main difference between the two methods resides in the matching condition of the two domains. In fact, while in the first method the information received by the fluid from the structure is exact but late, in the second the information is only predicted but at the right time.

This difference may prove crucial when performing aeroelastic analysis of a wing. Therefore, in this chapter, the aeroelastic response of a subsonic wing is computed using different staggered algorithms and possible enhancements are tested to study their influence on stability, accuracy and efficiency. The algorithms used for comparison are: CSS1: *Conventional Serial Staggered Algorithm*; CSS2: *Serial Staggered Algorithm with First Order Structural Predictor*; CSS3: *Serial Staggered Algorithm with Second Order Structural Predictor* and CSS4: *Improved Serial Staggered Algorithm*, as described in Section 6.2.

7.1 Aeroelastic Framework

The overall procedure for carrying out computational aeroelastic analyses, which is illustrated in Figure 7.1, can be divided into the following major steps:

1. Given a set of input parameters, described in Chapter 5, construct the geometry for aeroelastic computations and also supply appropriate boundary conditions and initial conditions;

2. Perform a steady-state CFD computation to obtain the initial aerodynamic forces for starting coupled computations;

3. Perform unsteady CFD computations, mapping the new aerodynamic forces onto the structural mesh;

4. Perform CSD computation to obtain the deformation of the geometry;

5. Update the position of the CFD mesh based on the displacements from the CSD computation. This step may vary with the chosen FSI method as described in Chapter 6;

6. Repeat steps 3-5 using current solution as the initial conditions for the subsequent steps until the stopping criterion is achieved.

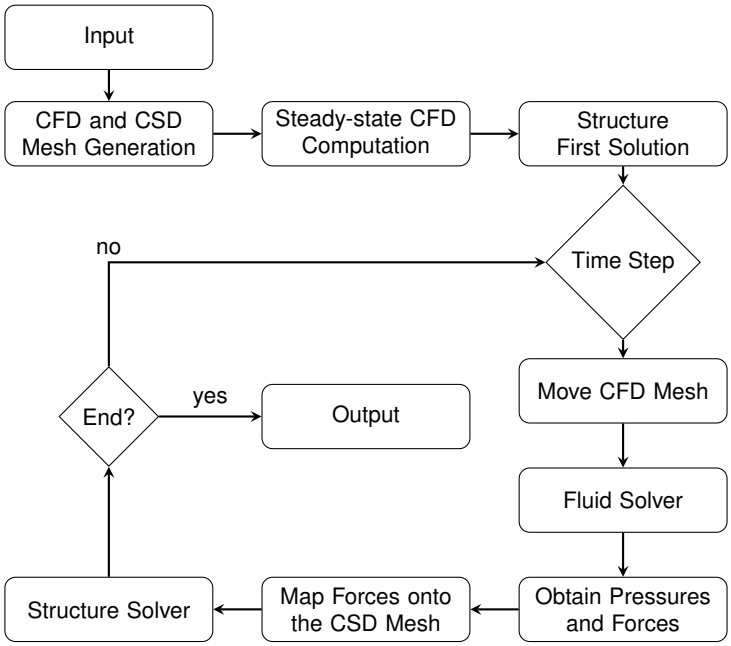

Figure 7.1: Flowchart illustrating the program‘s calculation process during aeroelastic analysis.

7.2 Reference Input Data

A rectangular wing with a NACA0015 airfoil was selected as the reference case. Table 7.3 summarizes the wing structural properties and the flight condition. Figure 7.2 shows an illustration of the wing. Finally, the root of the wing is fixed, simulating the place where it is attached to the fuselage of the aircraft. For the sake of efficiency, a coarse grid of 20x10 panels is chosen and a time step size of 0.1 s for the structural solver is selected.

7.3 Numerical Results

The first tests aim to study the influence of subiterating the CSS2 and CSS3 algorithms. In Section 6.2.2, the procedure was summarized and its purpose explained. When the structural displacement is predicted at each time step, the real displacement obtained through time integration might not correspond exactly to the predicted value, which induces an error. Using subiterations is an option that aims to remedy this aspect. Different analyses were conducted in order to study the behavior of the aeroelastic response of the wing, as shown in Figure 7.4.

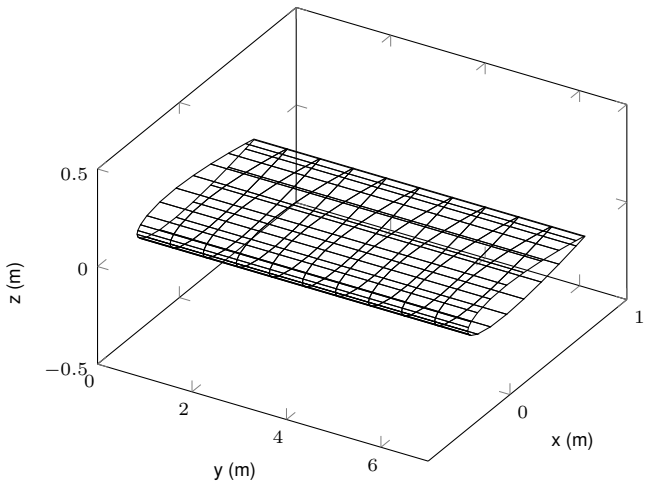

Figure 7.2: Reference case wing.

Wing Geometric Properties	
Half span	7 m
Chord	1 m
Angle of attack	2°
Spars location	30% and 70% of chord
Spars thickness	1 cm
Skin thickness	5 mm
Material Properties	
Young Modulus	75 GPa
Shear Modulus	30 GPa
Density	2800 kg/m^3
Flight Condition	
Altitude	1371 m
Air density	1 kg/m^3
Free-stream velocity	75 m/s

Figure 7.3: Reference case wing data.

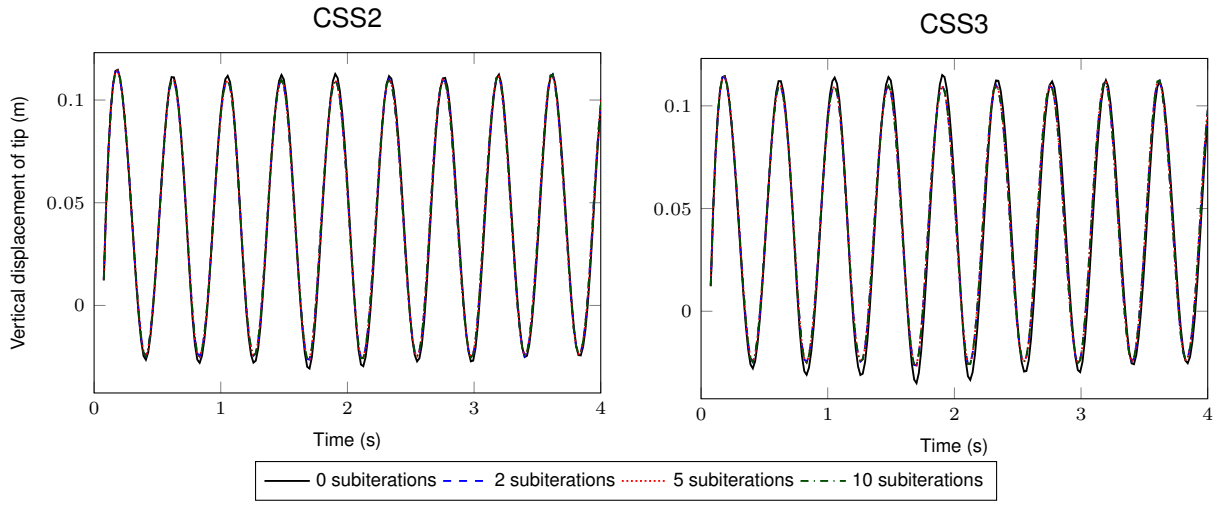

Figure 7.4: Influence of subiterating in the aeroelastic wing behavior.

It can be seen that, for both algorithms, the results are practically not affected by the use of subiterations, which suggests the predictors give a good approximation of the displacement at the end of each time step. Since the computational time increases linearly with the amount of subiterations used, it is not advantageous to use them.

The following tests are relative to the influence of subcycling the fluid solver. The main advantage of using subcycles is the possibility of having a small enough time step size for the fluid solver, while having a larger time step for the structural solver. This way, efficiency is obtained while preserving accuracy. The different analyses conducted are shown in Figure 7.5.

It can be concluded that increasing the number of subcycles also increase the maximum displacement in the negative direction while slightly decreasing the maximum displacement in the positive direction. This aspect is valid for every staggered algorithm tested. However, the stability of the movement remains unchanged while varying the number of subcycles. For example, in every analysis performed, the behavior from CSS1 is stable while the behavior from CSS3 is divergent, being already beyond the

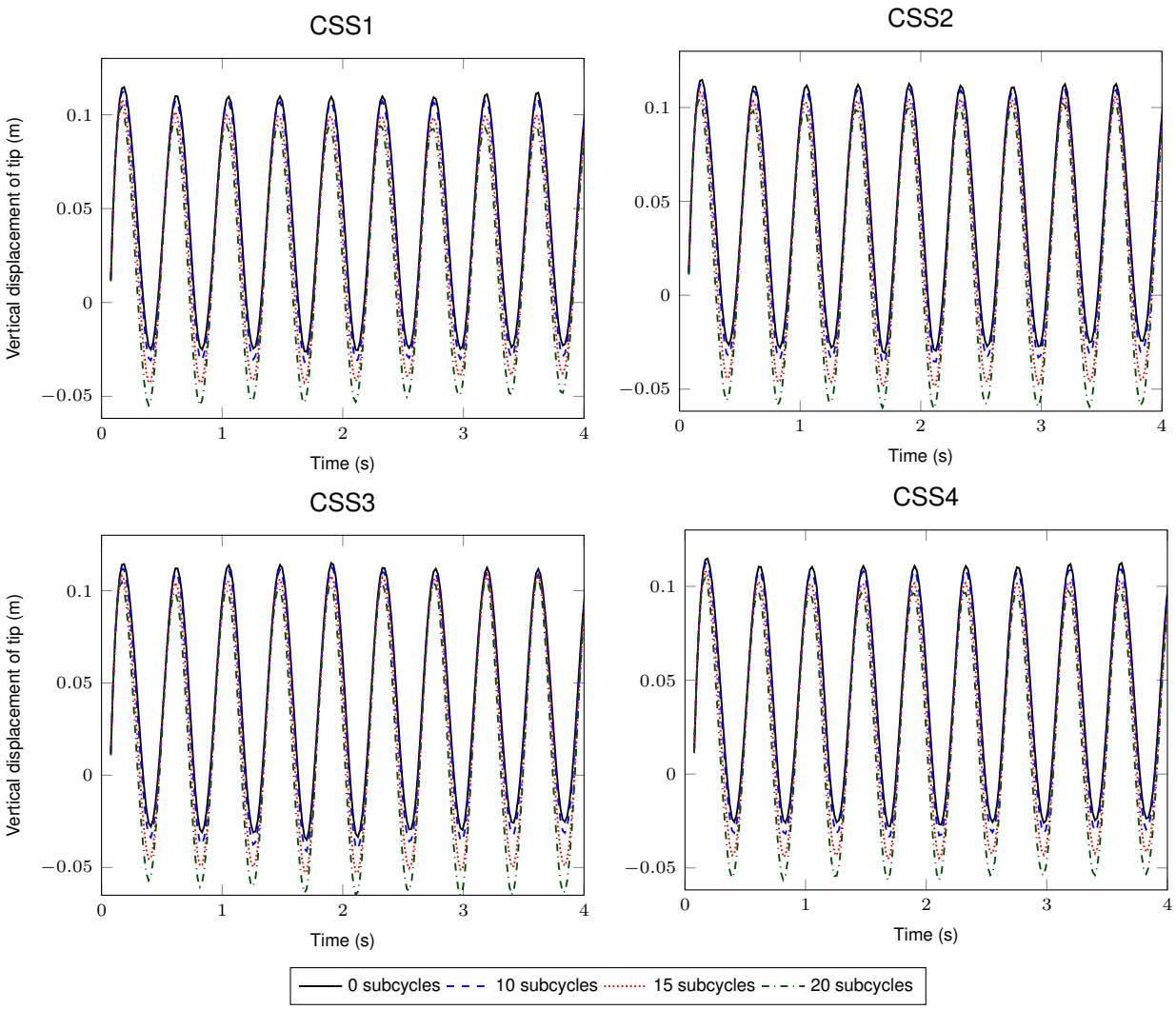

Figure 7.5: Influence of subcycling in the aeroelastic wing behavior.

flutter velocity. Figure 7.6 makes this aspect more clear. Both the CSS1 and CSS4 algorithms predict a stable behavior of the wing unlike the CSS2 and CSS3 algorithms. The most divergent movement occurs when employing the CSS3 algorithm, which uses a second-order predictor in contrast to the first-order predictor used by the CSS2 algorithm.

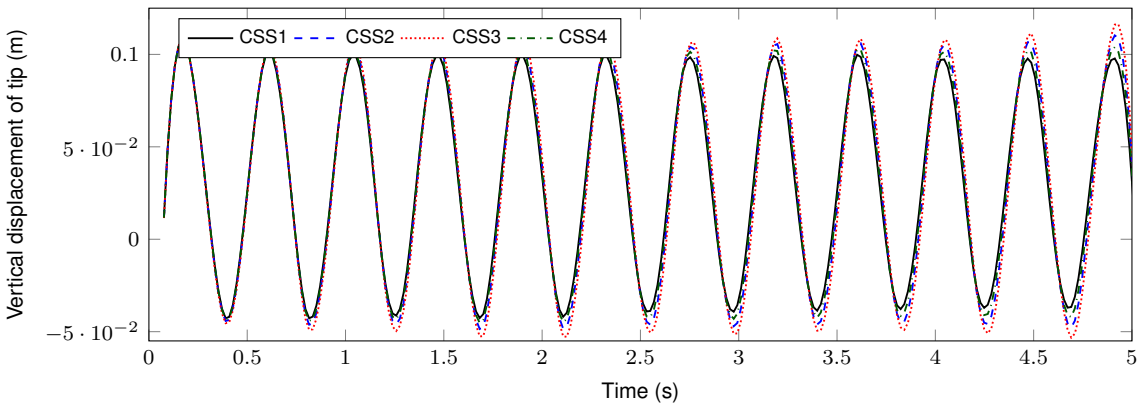

Figure 7.6: Comparison of the tip velocity displacement, using 15 subcycles and no subiterations.

Chapter 8

Aeroelastic Parametric Study

In Chapters 3 and 4, the two main domains of a FSI problem were presented and their application demonstrated, namely, the CFD and CSD models, respectively. Furthermore, Chapter 6 concerned the several methods and solutions for coupling the two referred domains and in Chapter 7 a comparison of these methods was performed. In this chapter, a parametric study will be conducted, having one input parameter changed at a time, in order to study the influence of each parameter in the aeroelastic behavior of the wing.

8.1 Reference Case Dynamic Computations

To test the program and perform aeroelastic analyses, the same wing from Chapter 7 serves as input here. The CFD grid was chosen considering two goals: to reduce the time needed for each time step and to have a level of discretization good enough to compute accurate results. Mesh sizes of 20x10, 40x20, 60x30 and 120x60 panels were tested. It was concluded that the solution converged using the grid 60x30 being, however, quite expensive. For the sake of efficiency and without losing significant information, the mesh size was reduced to 40x20 panels. Moreover, several time steps were tried, being 0.1 s the option selected as it saves more computational time without losing information.

Additionally, the CSS3 algorithm is applied, using 15 subcycles. The results from this computation are given in Figure 8.1, which represent the variation of the vertical displacement of the wing tip node, the torsional rotation of the same node and the lift coefficient with the time. A total time of 5 s is computed in this analysis.

The vertical movement of the wing tip is plotted in Figure 8.1(a). Like it was expected, the period and frequency of the vertical movement is constant during all computation. However, the increase of the wing maximal displacement shows clearly that the free stream velocity is already higher than the flutter velocity.

The same unstable behavior naturally occurs in the evolution of the rotation with time, which is confirmed by Figure 8.1(b). On the other hand, the frequency is higher than in the previous case. This behavior of the torsional rotation is characteristic of the beam element type used in the structural model,

as it was seen in Chapter 4. However, the values obtained are very low. In fact, the maximum absolute value obtained is $9.2 \cdot 10^{-4}$ *rad*, which roughly means $0.05°$, so it does not directly influence the bending movement and the flutter velocity.

Figure 8.1(c) shows the evolution of the lift coefficient with the time. After the initial steady solution, the variation is not significant. However, it is possible to see the small oscillations caused by the wing movement, which varies with approximately the same frequency as the nodal rotation as they are dependent on each other.

Moreover, a modal analysis was performed in order to characterize the structural behavior of the reference case wing. As a result, the first 8 natural frequencies were extracted, which are listed in Table 8.1. Additionally, the respective mode shapes are plotted in Figure B.1, which can be found in Appendix B. It is concluded that the majority of them are relative to flapwise bending, with the first chordwise bending and torsion modes corresponding to the third and sixth structural modes of the wing, respectively.

Mode	**Frequency**
1^{st} flapwise bending	2.93 Hz
2^{nd} flapwise bending	18.39 Hz
1^{st} chordwise bending	25.01 Hz
3^{rd} flapwise bending	51.49 Hz
4^{th} flapwise bending	100.9 Hz
1^{st} torsion	116.9 Hz
2^{nd} chordwise bending	156.72 Hz
5^{th} flapwise bending	166.79 Hz

Table 8.1: Modal analysis results for the reference case wing.

8.2 Aeroelastic Computations

In the previous section, the dynamic aeroelastic behavior of a reference case (RC) wing was summarized. Herein, further computations will be done changing one input parameter at a time. This study will be focused on the bending movement of the wing as the high frequency of the torsion makes it difficult to compare. Moreover, since the torsion is very low, when flutter velocity is achieved, the wing would first break from the bending movement. Finally, the results will be plotted and compared to the reference case.

8.2.1 Free Stream Velocity

The study of the free stream velocity influence is important to know when the divergence/flutter velocity occurs. As it was seen, the RC is already beyond it. Three more velocities were tested: 40, 60 and 100 m/s. Figure 8.2 shows the wing tip node behavior.

The graph for the 40 m/s has practically zero damping while the graph for 60 m/s has an higher amplitude and, although it may be difficult to see in the figure, the movement is already divergent.

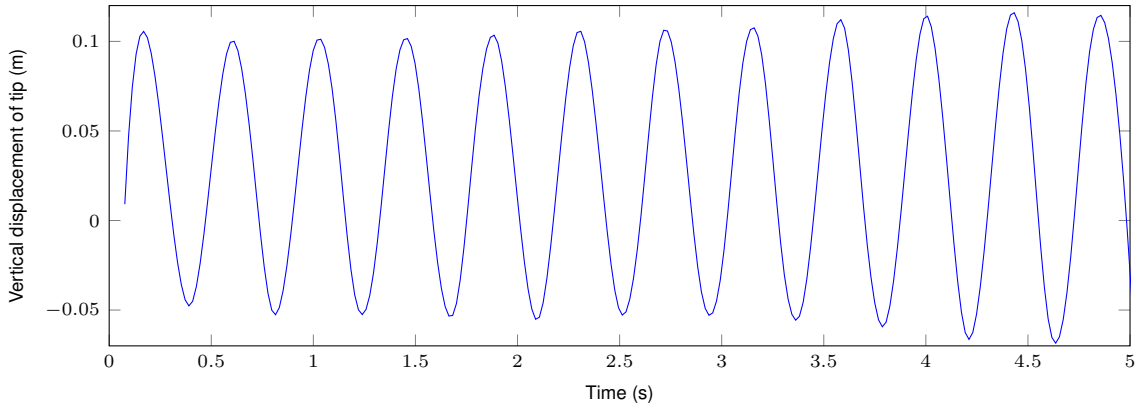

(a) Vertical displacement of wing tip node.

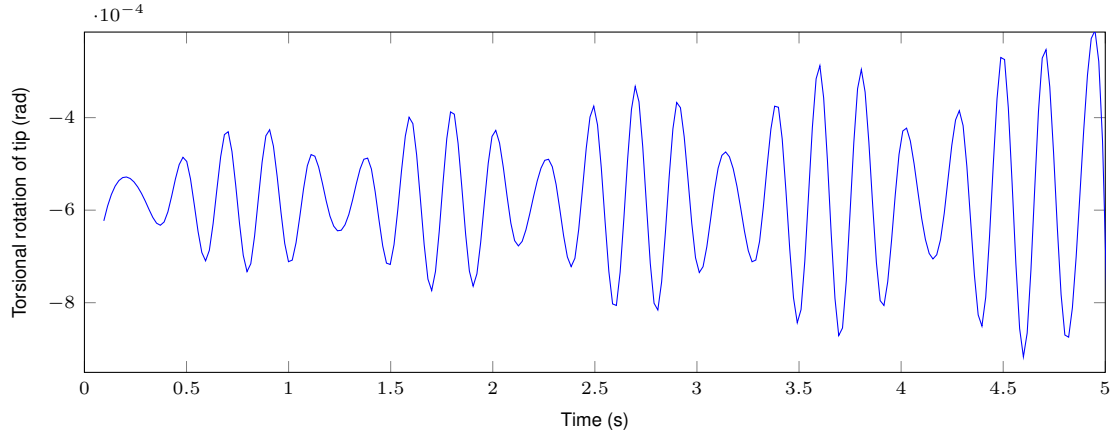

(b) Torsional rotation of wing tip node (negative rotation corresponds to wing nose-up).

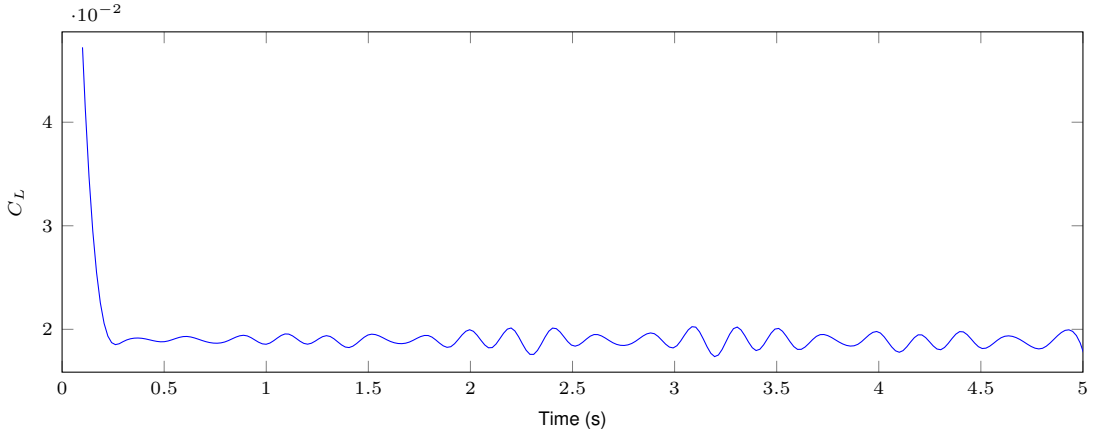

(c) Wing lift coefficient.

Figure 8.1: Aeroelastic results for the input values from Section 7.2.

Finally, with the 100 m/s the movement is completely divergent with the highest amplitudes.

In order to determine when the wing surpasses the divergence or flutter velocity, the damping ratio ζ was estimated, yielding positive damping for convergent solutions (stable), and negative damping for divergent solutions (unstable). The damping ratio can be derived from a quantity known as the

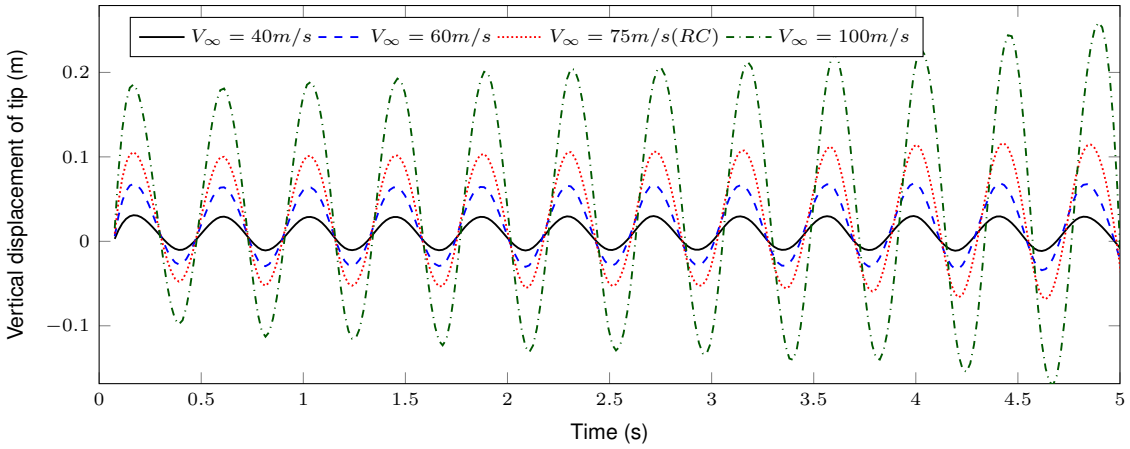

Figure 8.2: Influence of the free stream velocity in the aeroelastic wing behavior.

logarithmic decrement [11]

$$\delta_n = \frac{1}{n} ln \left(\frac{X_i}{X_{i+n}} \right) = \frac{2\pi\zeta}{\sqrt{1-\zeta^2}} \tag{8.1}$$

where X_i is the peak amplitude at a certain instant of time and X_{i+n} is the peak amplitude taken after n complete cycles of vibration.

Figure 8.3 shows the damping estimation as function of free-stream velocity regarding the vertical displacement and torsion. The interpolation line between the test points closest to zero damping is highlighted in black. It is concluded that torsional divergence occurs first at 42 m/s while the divergence speed for the wing bending movement occurs at 50 m/s. As a result, the aeroelastic phenomenon captured corresponds to torsional divergence.

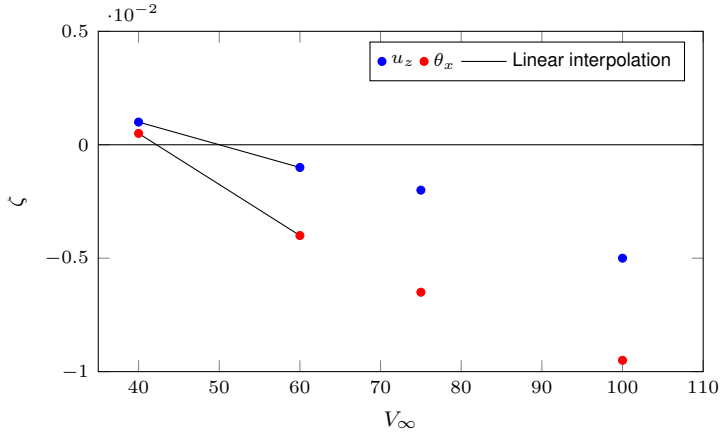

Figure 8.3: Damping factor as function of free-stream velocity for aeroelastic bending movement and torsion of the wing.

8.2.2 Sweep Angle

A swept wing is usually used in airplanes for many reasons, mainly to reduce the effective velocity and avoid shock waves in transonic flights, decreasing the drag in the process [41]. In this study, two swept wings were tested: a sweptback and a sweptforward wing, both with a sweep angle of $10°$.

As it can be seen from Figure 8.4, the bending movement has a slightly lower frequency and amplitude for the sweptback wing. Moreover, the amplitude upper and lower limits differ. With the sweptback wing, the bending movement has a lower upper limit but an higher lower limit compared to the reference case. However, the amplitude is decreasing in time, which indicates that the aeroelastic behavior is stable.

The sweptforward wing has a very different behavior. Not only the amplitude of the movement is much higher but it is also completely unstable. This is why the sweptforward wing is very rarely used in airplanes.

In fact, as demonstrated in [42], when a sweptback wing is subjected to bending the wing twists in such a way that the tip twists downwards (downwash), reducing the local angle of attack and offloading the tip. The reverse occurs in a sweptforward wing, as it twists in such a way increasing the angle of attack at the tip (upwash), thereby increasing the tip loading and further increasing the twist until the wing eventually fails. This aeroelastic behavior is clearly seen in Figure 8.4.

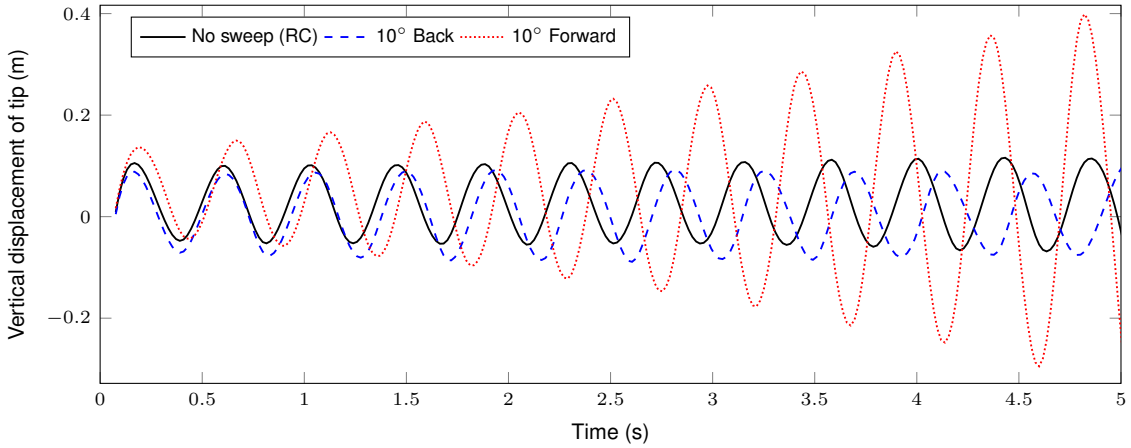

Figure 8.4: Influence of the sweep angle in the aeroelastic wing behavior.

8.2.3 Dihedral Angle

The dihedral angle is the upward angle from horizontal of the wings of an airplane. The ”anhedral” angle is the name given to negative dihedral angle, *i.e.*, when there is a downward angle from horizontal of the wings. The dihedral angle is very often used in airplanes because it has a stability effect on the rolling moment of the aircraft.

In this study, two tests were performed: one with a positive dihedral angle of 5° and one with a negative dihedral angle, or ”anhedral angle”, of -5°. The graphs are plotted in Figure 8.5.

It can be concluded that the bending movement is stabilizing with the positive dihedral angle, which is expected. However, the opposite occurs with the negative angle, where the movement is quite divergent. This is why a negative dihedral angle is seldom used in airplanes.

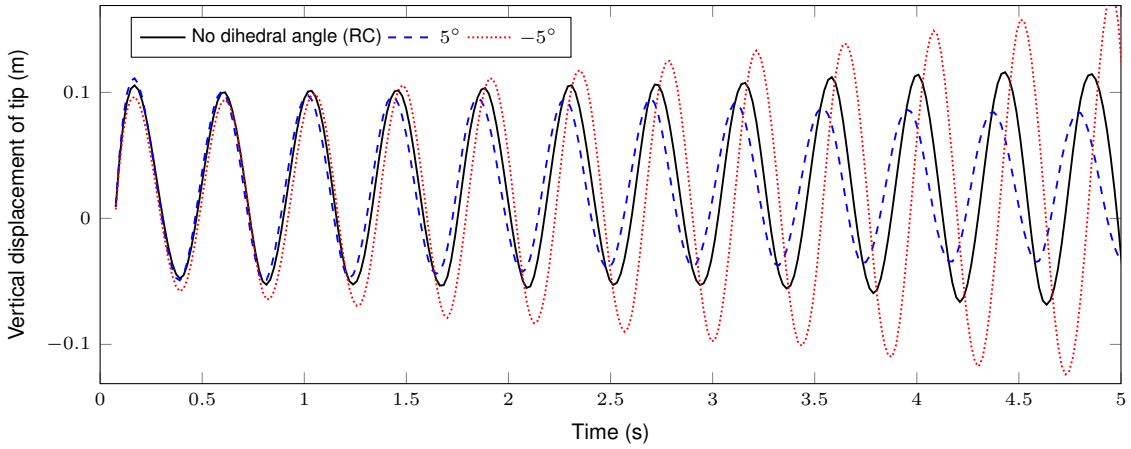

Figure 8.5: Influence of the dihedral angle in the aeroelastic wing behavior.

8.2.4 Taper Ratio

The taper ratio is denoted as the ratio between the wing tip and root chords. One of the key design drivers for the selection of the taper ratio is to minimize the amount of lift-induced drag, since it approximates a trapezoidal wing as an elliptic wing, which gives the minimum drag [41].

In this test, two computations were performed: with 0.3 and 0.7 taper ratio. Figure 8.6 summarizes the results. It can be concluded that diminishing the taper ratio increases the amplitude of the movement as well as the frequency. In fact, a wing with taper has less surface area than a wing with no taper and so the volume is lower too. This means that, assuming a constant material density, the weight of the wing decreases with taper.

This variation in weight influences the structural mass matrix M defined in Eq. (4.23) and so the inertial forces. A wing with less weight has weaker inertial forces causing the amplitude of the movement to be larger. This effect is similar to what is observed when the material density is changed, as it will be seen later.

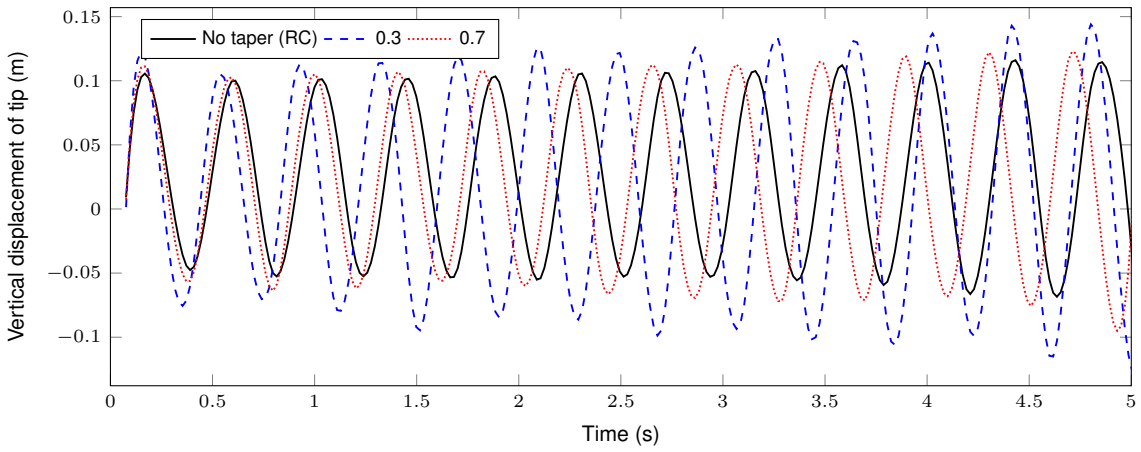

Figure 8.6: Influence of the taper ratio in the aeroelastic wing behavior.

8.2.5 Twist Angle

The twist angle is an aerodynamic feature used in aircraft wings to adjust the lift distribution along the wing. Its main purpose is to ensure the wing tip is the last part of the wing surface to stall, twisting it a small amount downwards (downwash) such that the effective angle of attack is always lower at the wing tip than at the root, meaning the root will stall before the tip.

In this test, the wing is linearly twisted from the root to the tip. Three computations were performed: with -2°, 2° and 5° maximum twist angle (at the tip). Here, a negative value means decreasing the wing incidence (downwash). The results are plotted in Figure 8.7.

It is concluded that the negative value of the twist angle stabilized the bending movement, compared to the reference case. This is physically correct since the total lift force acting on the wing surface is lower as the effective angle of attack decreased. On the other hand, for positive values of the twist angle (upwash), the wing incidence increased and so do the effective angle of attack. Consequently, the lift force is higher too which makes the bending movement oscillating more. It is clear that the amplitude of the movement is proportional to the twist angle. However, the frequency is the same for all cases tested. This fact is also valid for the wing torsion. However, the mean value changes with each test case because a permanent twist angle is applied.

8.2.6 Spar Location

In this test, the location of the two wing spars is changed. Three computations were performed, with spars at 0.45 and 0.55 chords, which means closer to each other at the center of the airfoil; 0.1 and 0.3 chords, which means close to the leading edge and, finally, 0.7 and 0.9 chords, which means close to the trailing edge.

From Figure 8.8, it is concluded that the first two cases mentioned do not influence the bending movement, which is very similar comparing to the reference case. This similar behavior is expected because the elastic center (shear center of the airfoil) does not vary significantly between the two cases and the reference case.

However, this does not happen with the spars located at 0.7 and 0.9 chords. In this case, the elastic center is further moved from the aerodynamic center, causing torsional divergence and, consequently, also bending divergence.

8.2.7 Thickness of Spars and Skin

In this case, the thickness of the wing spars and skin is changed. First, two more computations were performed besides the reference case, varying the thickness of the spars while maintaining constant the other parameters, with 0.05 m and 0.1 m. The results are plotted in Figure 8.9. It is clear that the amplitude of the movement is decreasing with the thickness as well as the frequency. That is physically correct, since the cross-sectional area is higher and, consequently, the total rigidity of the wing is greater.

The same conclusion can be applied to the other case, where the skin thickness is changed. Two computations were performed: 0.001 m and 0.01 m. Since the reference case wing is already beyond

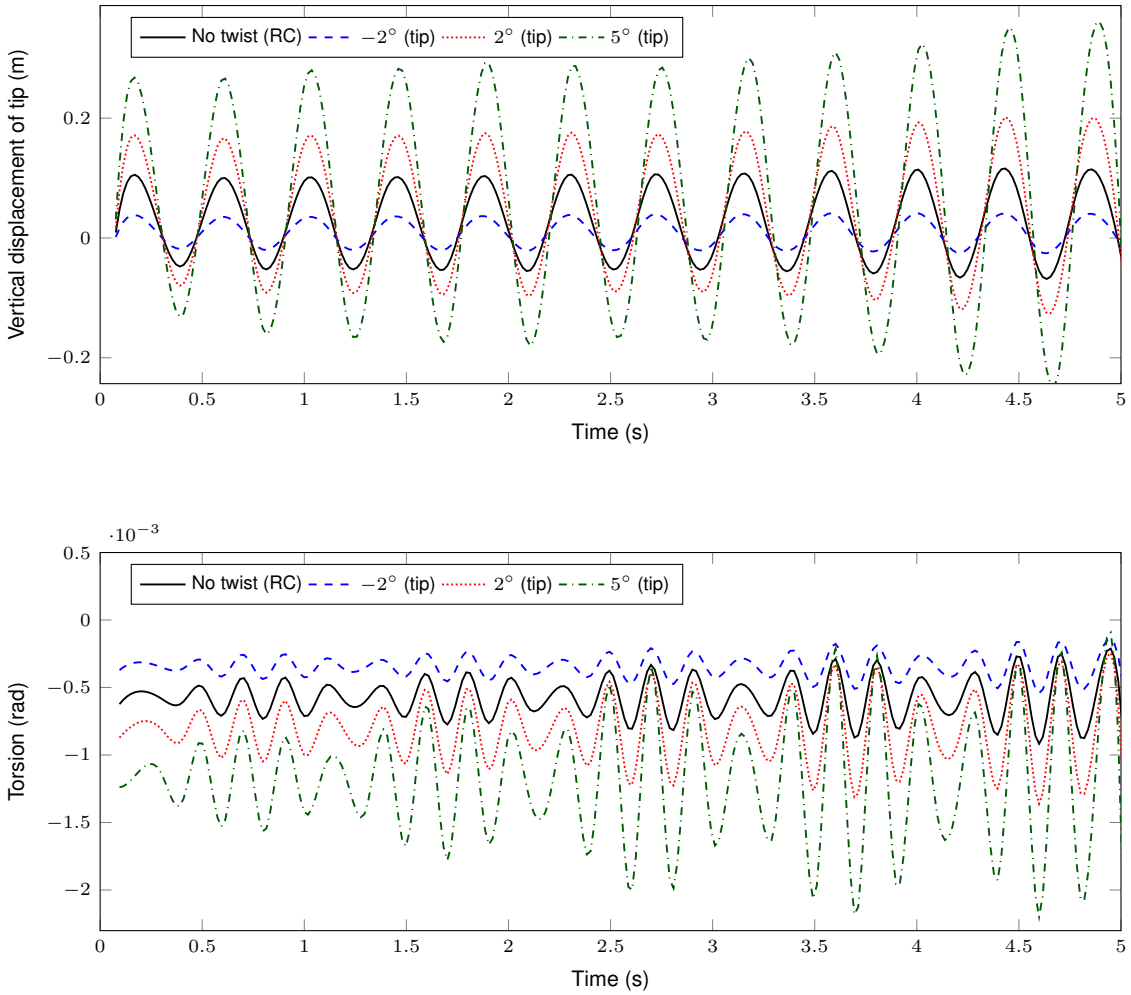

Figure 8.7: Influence of the twist angle in the aeroelastic wing behavior.

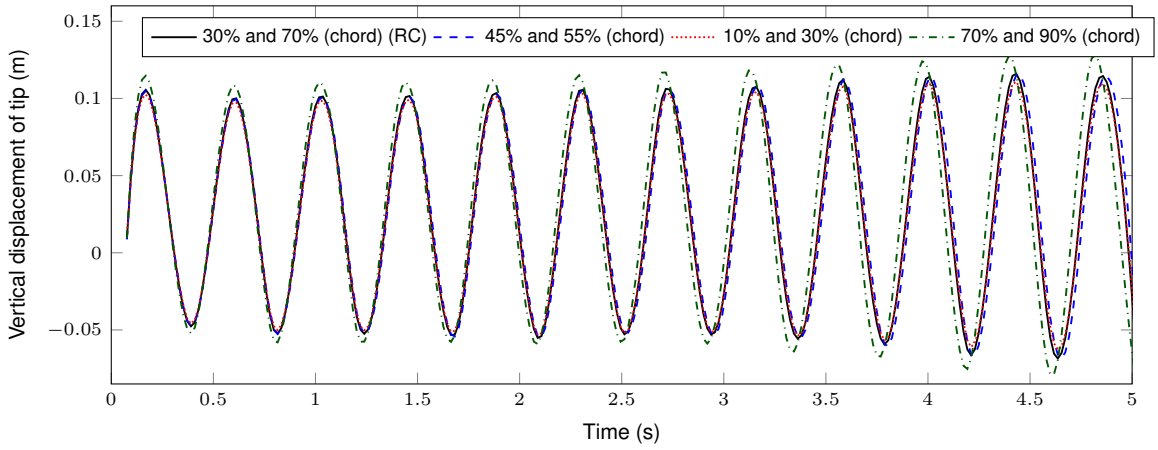

Figure 8.8: Influence of the spars location in the aeroelastic wing behavior.

the flutter velocity, decreasing the thickness of the skin to 0.001 m only aggravates it, as it is shown in Figure 8.10. However, the variation in thickness is much smaller than the previous case while the movement is much more unstable. This behavior is naturally explained by the absence of some of the

typical structural elements of the wing, namely the stringers which support the thin layer of skin, avoiding its deformation. In order to compensate this limitation, exaggerated skin thickness must be used.

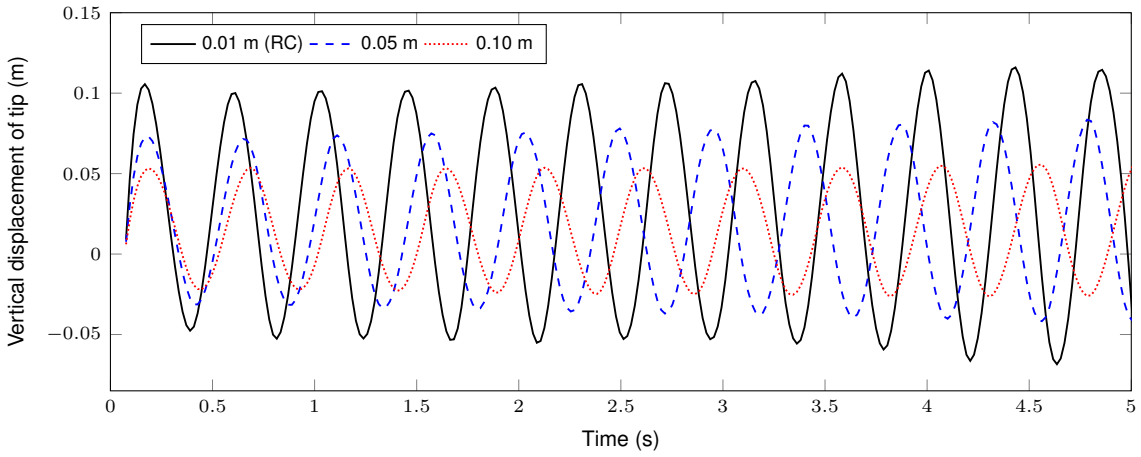

Figure 8.9: Influence of the thickness of spars in the aeroelastic wing behavior.

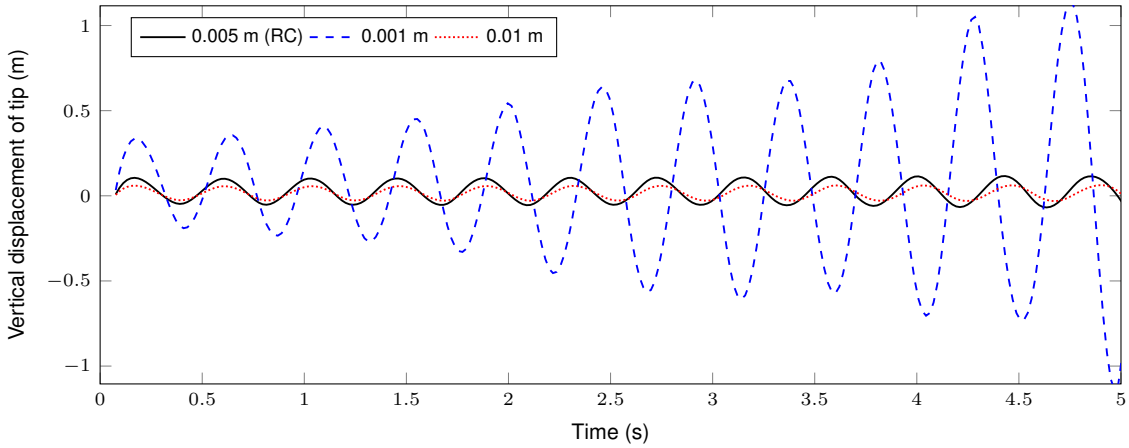

Figure 8.10: Influence of the thickness of skin in the aeroelastic wing behavior.

8.2.8 Material Density

In the next two studies, material properties will be tested. Here, the influence of the material density is investigated (assuming the wing is only composed of a single material). The density has an influence on the structural mass matrix M defined in Eq. (4.23). This matrix influences the inertial forces, so that the higher the density, the higher the inertial forces.

Since the goal is to study the influence, unrealistic materials will be used. Besides the reference case, two more tests were performed: using 800 kg/m^3 and 9000 kg/m^3. Figure 8.11 shows the results.

One can arrive at two main conclusions. The first is that the frequency of the movement is affected by the density. In fact, the higher the density, the lower the frequency. The second is that reducing density also helps the wing to diverge, since the upper limits increase in comparison with the reference case. Such is the case of the 800 kg/m^3 graph. On the contrary, higher density means more weight and more

inertia causing the amplitude of the movement to be smaller. This can be observed in the 9000 kg/m^3 graph.

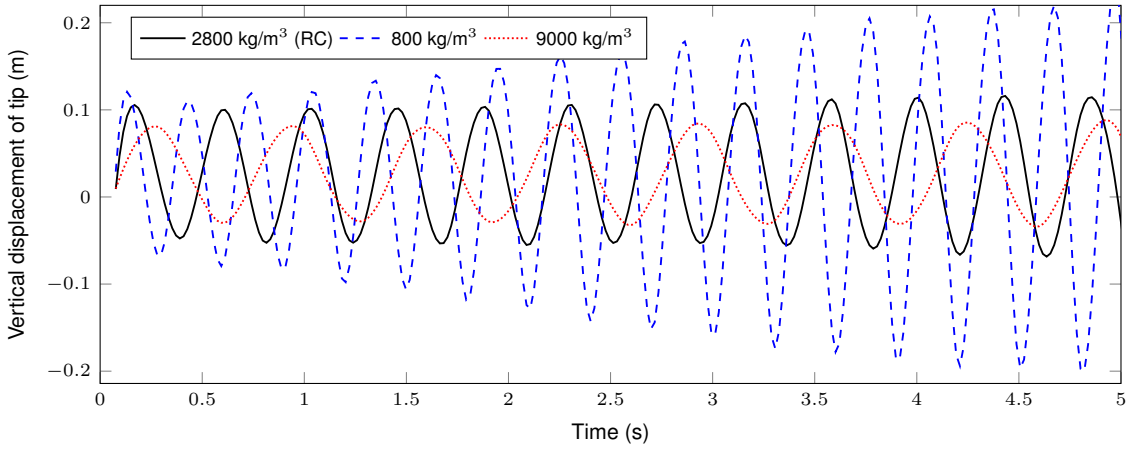

Figure 8.11: Influence of the material density in the aeroelastic wing behavior.

8.2.9 Material Young Modulus

This study concerns the material Young modulus E. This parameter is presented in the structural stiffness matrix K defined in Eq. (4.19). The stiffness of the material increases with E while the elasticity diminishes.

Besides the reference case, two more tests were performed: using 50 GPa and 100 GPa. The results are presented in Figure 8.12.

It can be seen that increasing the Young modulus decreases the amplitudes of the movement while increasing the frequency. Such happens with 100 GPa, which is expected since the stiffness is higher. However, the change in stiffness is not sufficient to prevent divergence, since the amplitude is increasing with time. On the other hand, with 50 GPa the material becomes more elastic and so the amplitudes are higher and the frequency is lower, which is physically correct.

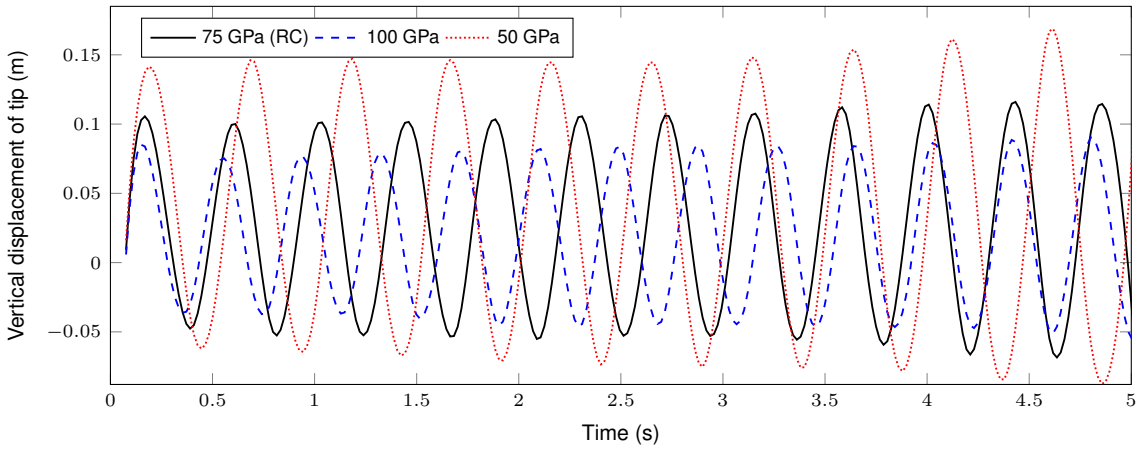

Figure 8.12: Influence of the material Young modulus in the aeroelastic wing behavior.

8.2.10 Material Shear Modulus

The last study concerns the material shear modulus G. Likewise the Young modulus, this parameter is presented in the stiffness matrix K. It influences the stiffness of the torsional rotation, which increases with G.

Two cases were tested: using 60 GPa and 10 GPa. The results are presented in Figure 8.13. It can be seen that the difference between the reference case and using 60 GPa is negligible, mainly because the torsion is already very low in the reference case, as it is shown in Figure 8.1(b). Therefore, an increase of torsional stiffness only further contributes to the reduction of torsion. However, it is possible to see the slightly increase of amplitude using 10 GPa due to the decrease of torsional stiffness.

The graph relative to torsion shows a completely different behavior. It can be seen that using 10 GPa turns the movement quite divergent compared to the other test cases. This is naturally explained as the torsional stiffness of the wing is lower. Moreover, the graph clarifies that torsional divergence is the main cause of aeroelastic instability.

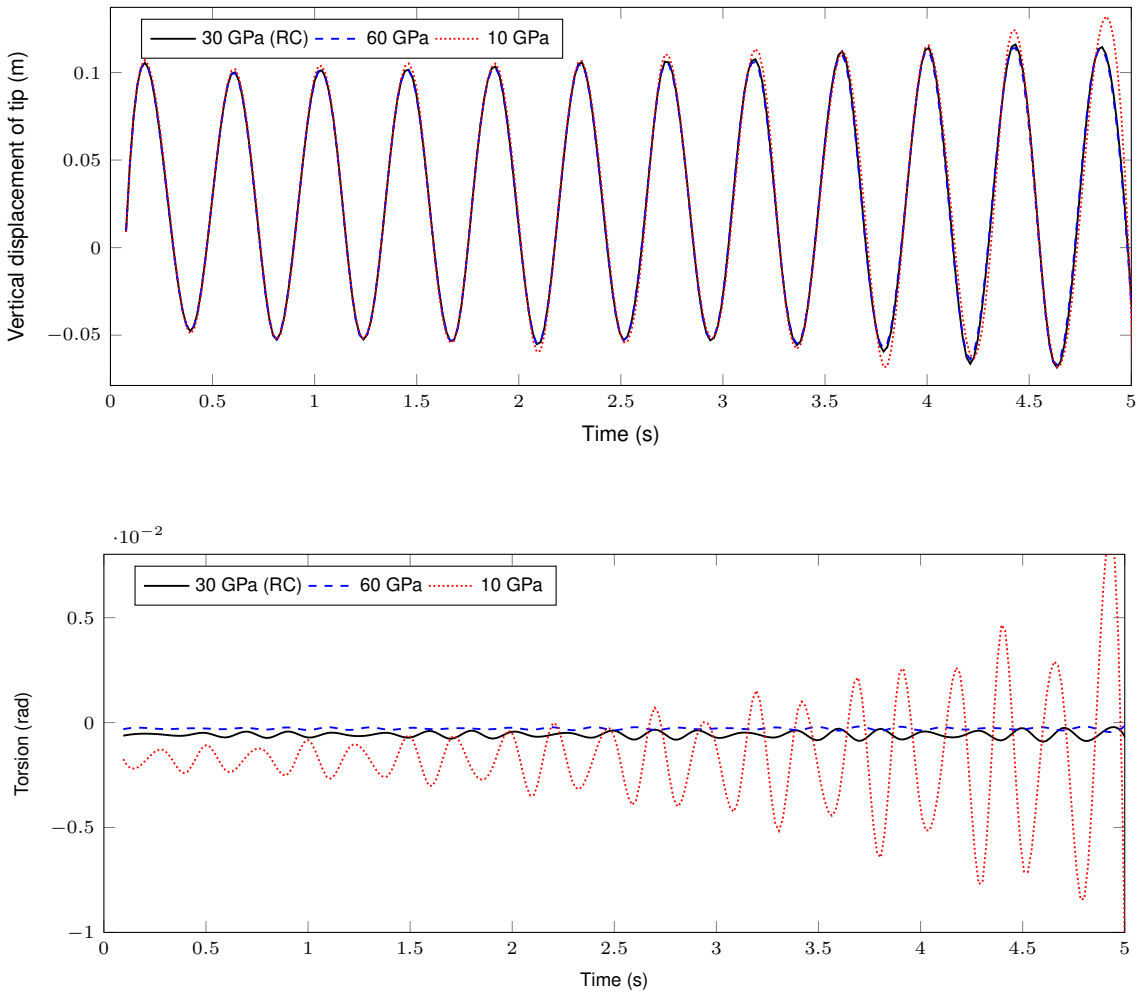

Figure 8.13: Influence of the material shear modulus in the aeroelastic wing behavior.

8.3 Summary of Results

In this section, the main results of the aeroelastic parametric study will be presented, focusing on the effect of the parameters studied on the amplitude and frequency of the wing vertical flapping motion. Table 8.2 summarizes the results. Overall, the study revealed results which are in very good agreement to the theoretical influences of the parameters studied.

Increase in	**Amplitude**	**Frequency**
Free-stream velocity	Increases	Does not change
Sweep angle (back)	Slightly decreases	Decreases
Sweep angle (forward)	Increases	Increases
Dihedral angle	Decreases	Slightly increases
(Decrease in) *Taper ratio*	Increases	Increases
Twist angle	Increases	Decreases
Spars thickness	Decreases	Decreases
Skin thickness	Decreases	Slightly increases
Material density	Decreases	Decreases
Material Young modulus	Decreases	Increases
Material shear modulus	Slightly decreases	Does not change

Table 8.2: Effect of the parameters studied on the amplitude and frequency of the wing flapping motion.

Chapter 9

Aero-Structural Optimization of Aircraft Wing

The final goal of this work is to perform an aero-structural optimization study of an aircraft wing. To achieve this, a simple case is selected focusing on the optimization of the geometric parameters of the wing, as well as its internal structure, based on aeroelastic static results. In a static aeroelastic problem, one eliminates the inertial forces, which shall cause the wing to converge to a stable position if the divergence velocity is not exceeded. In the next section, the optimization tool will be chosen and the optimization problem will be formulated. In the end of the chapter, the results from the optimization study will be presented and discussed.

9.1 Optimization Theory Overview

In optimization, several algorithms exist to find a $\vec{x}$ that minimizes or maximizes a function f, whether it is a linear or nonlinear problem, constrained or unconstrained. However, a common approach is the use of a *line search* strategy [43], which first finds a descent direction along which the objective function f will be reduced and then computes a step size that determines how far $\vec{x}$ should move along that direction.

The descent direction can be computed by several methods, being the *gradient descent* one of them [43]. With this method, steps proportional to the negative of the gradient of the objective function at the current point are taken to find a local minimum. The gradient is defined by

$$\nabla \vec{f} = \left(\frac{\partial f}{\partial x_1}, ..., \frac{\partial f}{\partial x_n} \right) , \tag{9.1}$$

where the subscript n refers to the number of variables. To compute the gradient, finite differences are commonly used, such as the first-order forward difference scheme

$$\frac{\partial f}{\partial x_j} \simeq \frac{f(\vec{x} + \Delta x_j) - f(\vec{x})}{\Delta x_j} \quad j = 1, ..., n \, . \tag{9.2}$$

This implies further n function evaluations for the estimation of the gradient. An example of a unconstrained gradient-based method that uses a line search is given as follows:

- Set iteration count $i = 0$ and make an initial guess $\vec{x}_0$ for the minimum;
- Compute a descent direction, *e.g.*, $-\nabla\vec{f}$;
- Choose α^* to minimize $f(\vec{x} - \alpha\nabla\vec{f})$, where α is a scalar;
- Update $\vec{x}_{i+1} = \vec{x}_i + \alpha^*\nabla\vec{f}$, and $i = i + 1$;
- Repeat the last three steps until $\| \nabla\vec{f}(x_i) \| < tolerance$.

For constrained optimization methods, details can be found in [43].

9.2 Optimization Problem

A function from Matlab® called *fmincon* [44] was selected to run the optimization problem, finding the minimum of a constrained multivariable function. The default options are unchanged except the stopping criterion, where the tolerance of the function value is changed from 1E-6 to 1E-3.

The function *fmincon* varies the geometric parameters of the wing, which are stored in a vector $\vec{x}$, in order to minimize the objective function $f(\vec{x})$, taken as the wing total mass. The problem is subjected to linear and nonlinear constraints. Mathematically, it is formulated as

$$\begin{aligned} &\underset{\vec{x}}{\text{minimize}} \quad f(\vec{x}) \\ &\text{subject to} \quad A \cdot \vec{x} \leq b, \quad c(\vec{x}) \leq 0, \quad ceq(\vec{x}) = 0\,, \end{aligned}$$

where A is a matrix, b is a vector and $c(\vec{x})$ and $ceq(\vec{x})$ are functions that return vectors, corresponding to the nonlinear constraints.

In this study, the reference case wing from Chapters 7 and 8 will also be used as the starting point. The design variables are: *taper ratio* λ, *sweep angle* Λ, *dihedral angle* Γ, *angle of attack* α, *twist angle at the tip* θ_{tip} (increasing linearly from the root to the tip), *position of spars relative to the chord* x_{spar}, *thickness of spars* t_{spars} and *thickness of wing skin* t_{skin}. Table 9.1 lists the lower and upper limits chosen for the design variables, as well as the respective initial values.

The remaining parameters are kept constant, namely the free stream velocity, air density, root chord, wing span and material properties (E,G and density), as provided in Chapter 7.

To close the problem, all that remains is the definition of the nonlinear constraints. Since this is an aero-structural problem, the 3D lift coefficient was fixed with a value of 0.04, chosen arbitrarily, while the maximum stress and tip deflection were constrained with an upper boundary. For the stress, the limit is the yield strength of the material, with a value of 270 MPa. The maximum deflection was limited to 10% of the wing semi-span.

Parameter	Lower bound	Upper bound	Initial Value
Taper Ratio	0.3	1	1
Sweep Angle	0°	10°	0°
Dihedral Angle	0°	10°	0°
Twist Angle at Wing Tip	0°	10°	0°
Angle of Attack	1°	10°	2°
Front Spar Location	10%	40%	30%
Rear Spar Location	50%	90%	70%
Spars Thicknesses	0.01 m	0.05 m	0.01 m
Skin Thickness	0.001 m	0.01 m	0.005 m

Table 9.1: Bounds of the design variables and initial values.

In the end, the problem is formulated as

$$\begin{aligned} &\underset{\vec{x}}{\text{minimize}} \quad f(\vec{x}) = WingMass \\ &\text{subject to} \quad C_L = 0.04, \quad \sigma_{VM} \leq 270MPa, \quad \delta_{tip} \leq 0.7m\,, \end{aligned}$$

where $\vec{x} = (\lambda, \Lambda, \Gamma, \alpha, \theta_{tip}, x_{spar,front}, x_{spar,rear}, t_{spars}, t_{skin})$.

9.3 Optimization Results

The optimization algorithm stops when a converged solution is obtained, which occurred after only 5 iterations. One iteration corresponds to 10 function evaluations to determine the gradient descent, as explained in Section 9.1. As a result, the function was called 50 times. Figure 9.1 illustrates the convergence of the objective function with each iteration, yielding a minimum value of 45.15 Kg.

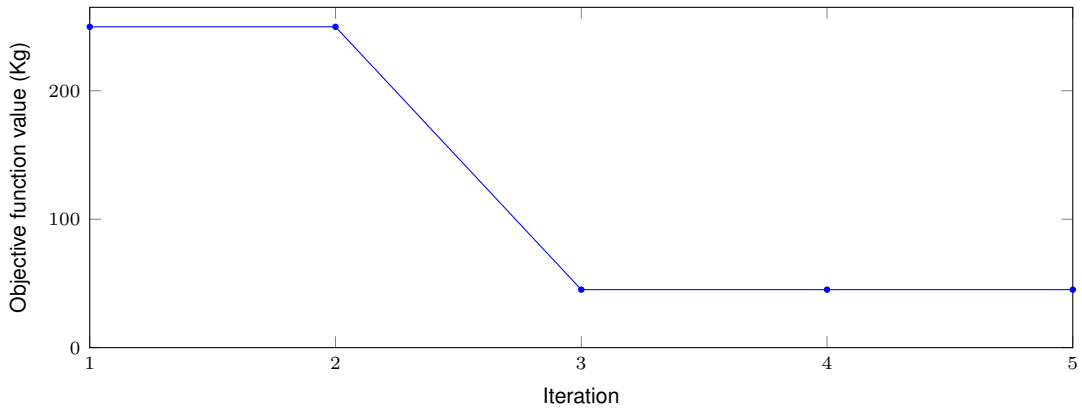

Figure 9.1: Objective function value convergence.

Illustrations of the wing shape and internal structure before and after optimization are shown in Figure 9.2.

The design variables obtained after the optimization process are listed in Table 9.2. In order to satisfy the constraint related to the lift coefficient, the wing angle of attack and twist angle increase, mainly because the taper ratio decreases and, consequently, the wing surface area does too. As a

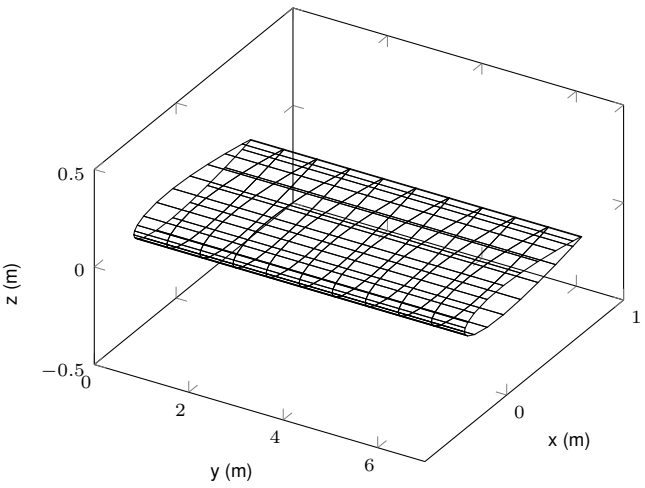

(a) Wing shape before optimization.

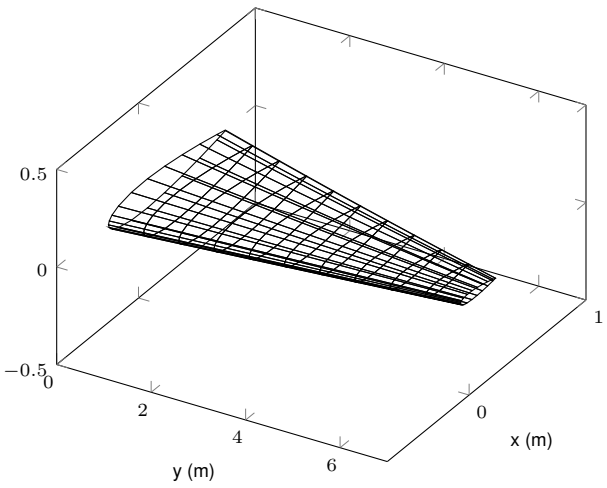

(b) Wing shape after optimization.

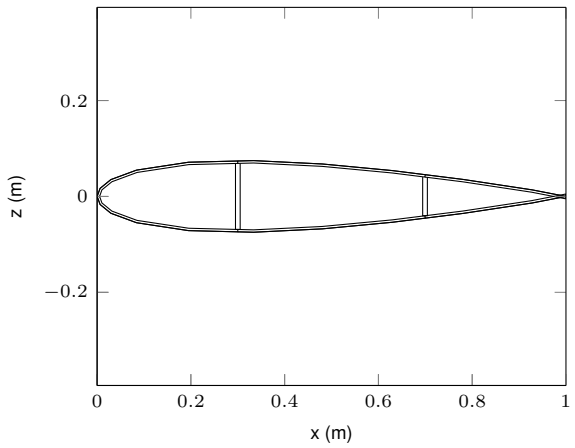

(a) Internal structure before optimization.

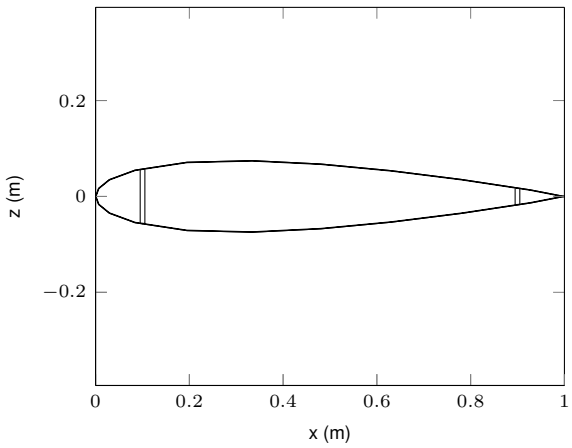

(b) Internal structure after optimization.

Figure 9.2: Evolution of the wing shape and internal structure during the optimization process.

result, the lift generated must be higher, which is provided by the change in those parameters.

Moreover, the sweep angle remains unchanged while the dihedral angle slightly raises. The variation is not significant because these parameters are mainly related to stability effects and not lift enhancement. Since the objective was to minimize the total mass, the taper ratio decreases while the thickness diminishes. Another interesting conclusion is related to the positioning of the spars. In fact, the optimized wing presents the maximum distance possible between the spars, *i.e.*, the wing box is larger. As a result, the spars height diminishes and, consequently, the wing mass is lower.

Finally, it is concluded that some of the optimal values are either in the predefined lower or upper bounds, as shown in Table 9.2. This may indicate that the solution is not properly constrained which is proven by the analysis of Figure 9.3.

In fact, in order to understand the impact of the change in parameters on the static results, a comparison is made between the initial and final configurations through the different plots. Although it is within the imposed boundaries, the deflection is much higher for the optimized wing. This behavior is natural since the structural rigidity of the wing is lower. Consequently, the maximum stress increases as the displacements are higher and the cross sectional area is lower.

Parameter	Before Optimization	After Optimization
Taper Ratio	1	0.3 (min)
Sweep Angle	0°	0° (min)
Dihedral Angle	0°	0.05°
Twist Angle at Wing Tip	0°	3°
Angle of Attack	2°	3.8°
Front Spar Location	30%	10% (min)
Rear Spar Location	70%	90% (max)
Spars Thicknesses	0.01 m	0.01 m (min)
Skin Thickness	0.005 m	0.001 (min)

Table 9.2: Design variables after optimization.

However, the solution is not tip deflection constrained nor stress constrained since the optimal values of these properties are much lower than the respective bounds:

$$\delta_{tip,optimal} = 0.23m < \delta_{tip,max} = 0.7m\,, \qquad \sigma_{optimal} = 72MPa << \sigma_{max} = 270MPa\,.$$

It is concluded that the wing is still very rigid and the optimal thicknesses, which are already in the lower bound limit, could be smaller since the objective is to reduce the wing mass. However, the bounds must be chosen carefully as a too low value could lead to a solution failing to meet other constraints. For example, zero thickness would lead not only to minimum mass but also to infinite stress, which is physically impossible. It should also be noticed that no buckling effects were considered in the analysis. Had this been done, possibly a different optimal thickness would also have resulted.

Finally, it is shown that C_L converges to the desired value, being the only constraint that is fully met.

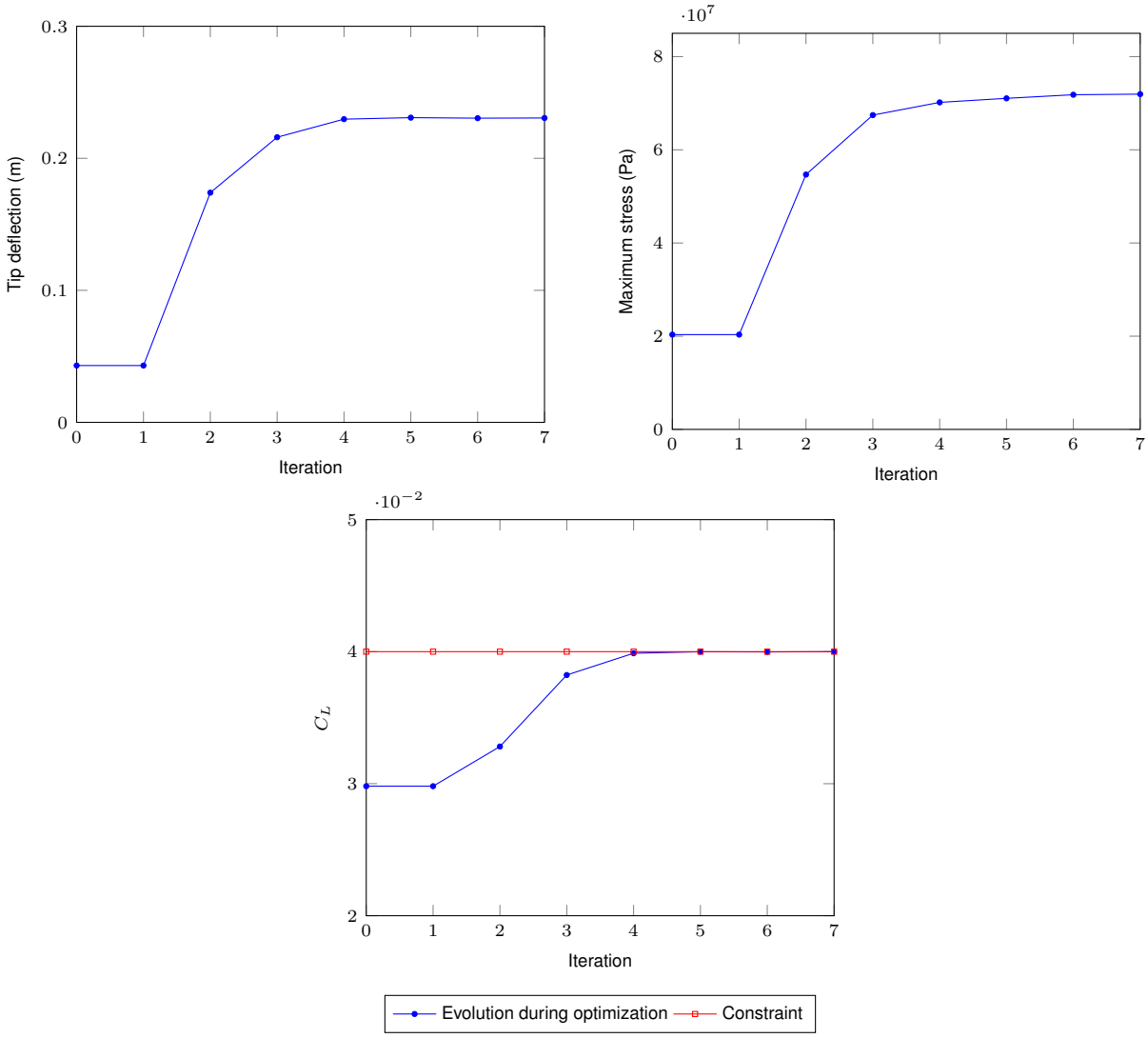

Figure 9.3: Aeroelastic static results of the reference case wing after optimization.

Chapter 10

Conclusions

10.1 Achievements

A computational tool was developed with the purpose of studying the aerolelastic behavior of a 3D aircraft wing. It comprises three main parts: the aerodynamic model developed by Cardeira [19], the structural model based on beam element formulation coded in Matlab® and a coupling procedure also developed in Matlab®.

The aerodynamics were modeled according to potential fluid theory in which the pressure forces were calculated based on the 3D geometry of the wing. The methodology of solution consisted in a panel method approach, whose steady results were compared with another panel method program presented in [21] and with experimental results. The results proved to be in agreement with each other.

The structural model consisted of a one-dimensional beam clamped at the aircraft fuselage, and representative of the wing elastic axis. It was fully developed in Matlab®, including the stiffness and mass matrices of the system. The commercial software ANSYS® APDL was used to verify the static and transient results, which revealed very similar results in both analysis. The Newmark method was employed to perform dynamic computations.

In order to account for the wing structural properties, the structural model requires the information of the material properties and the equivalent cross section properties, namely, the axial, bending and torsional rigidity. To do so, the wing is parametrized and the area moments of inertia relative to the elastic axis of each cross section are calculated.

The coupling of the fluid and structural models was a crucial part of this work. The equivalent beam was placed inside the wing, with the structural nodes located in the middle and at the sides of each ring of panels. This facilitated the transfer of the aerodynamic loads to the structural nodes using the D´Alambert‘s Principle. Moreover, a linear extrapolation procedure was employed to transfer the displacements of the beam model to the original fluid grid, assuming a rigid link connection between the structural nodes and the fluid grid points.

Several coupling algorithms were taken from the literature and presented, before being implemented and tested. The main difference between them resides in the information received by the fluid solver

from the structural solver, which can be exact but late or predicted but at the right time. Moreover, some possible enhancements were tested such as subiterations and subcycles. After studying the effect of these algorithms on the aeroelastic results of a reference case wing, it was concluded that the use of subcyles has a major impact on the amplitude of the movement but does not change its stability while the use of subiterations do not have any significant impact. Furthermore, when using a structural predictor, the movement becomes divergent.

Having decided which coupling algorithm to use, the aeroelastic framework was created. It starts with a steady solution for the values input. Then, it generates the fluid and structural meshes. After the first structural solution, a time cycle starts according to the coupling algorithm chosen.

After defining a reference group of input, a dynamic aeroelastic computation was performed. The results obtained were used as the reference case for a parametric study. The first parameter to vary was the free stream velocity, which showed that it is possible to calculate an approximate critical velocity. Moreover, it was concluded that torsional divergence is the main cause of aeroelastic instability. The other tests revealed results which were physically correct.

Finally, a simple aero-structural optimization case study was performed. The objective was to minimize the wing mass while constraining the tip deflection and maximum stress with a fixed value for the lift coefficient. The results were expected since the total area of the wing cross-sections have lowered, thus reducing the volume and, consequently, the total mass. Moreover, all the constraints were fulfilled and the goal of the optimization was met.

10.2 Future Work

The beam representation for a wing structure can be valuable for early phases of aircraft design. In later stages, however, the complexities of aircraft components are difficult to model with a beam representation. A great improvement is the coupling of this model with compatible shell elements to allow for accurate modeling of the outer skin of a semi-monocoque structure. Thus, the use of shell elements to model the panels and beam elements to model the wing spars and booms would allow for much more realism.

Another very important step would be to construct a wing model to perform tests in a wind tunnel to validate the results computed with this framework, which could only be validated with static results.

Finally, the optimization problem addressed in this work only concerned static aeroelastic results. Further optimization problems can be tackled such as the flutter speed maximization of an aircraft wing with constraints in weight.

Bibliography

[1] I. E. Garrick and W. H. Reed III. Historical development of aircraft flutter. *Journal of Aircraft*, 18(11): 897–912, Nov. 1981. DOI: 10.2514/3.57579.

[2] D. H. Hodges and G. A. Pierce. *Introduction to Structural Dynamics and Aeroelasticity*. Cambridge University Press, New York, USA, 2nd edition, 2011. ISBN: 9781107617094.

[3] T. A. Weisshaar. Static and dynamic aeroelasticity. *Encyclopedia of Aerospace Engineering*, 2010. DOI: 10.1002/9780470686652.eae149.

[4] M. W. Kehoe. A historical overview of flight flutter testing. *NASA-TM-4720*, Oct. 1995.

[5] C. E. S. Cesnik, P. J. Senatore, W. Su, E. M. Atkins, and C. Shearer. X-hale: A very flexible unmanned aerial vehicle for nonlinear aeroelastic tests. *AIAA Journal*, 50(12):2820–2833, Dec. 2012. DOI: 10.2514/1.J051392.

[6] http://www.nasa.gov/centers/armstrong/news/FactSheets/FS-068-DFRC.html, accessed on June 2015.

[7] T. H. G. Megson. *Aircraft Structures for Engineering Students*. Elsevier, 4th edition, 2007. ISBN: 0080969054.

[8] R. Clark, D. Cox, H. C. Curtiss Jr., J. W. Edwards, K. C. Hall, D. A. Peters, R. Scanlan, E. Simiu, F. Sisto, and T. W. Strganac. *A Modern Course in Aeroelasticity*, volume 116 of *Solid Mechanics and its Applications*. Kluwer Academic Publishers, 4th edition, 2005. ISBN: 9781402020391.

[9] A. R. Collar. The first fifty years of aeroelasticity. *Aerospace*, 5(2):12–20, Feb. 1978.

[10] C. Panda and V. S. R. P. Aeroelasticity - in general and flutter phenomenon. *ICETET*, pages 81–85, Dec. 2009. DOI: 10.1109/ICETET.2009.23.

[11] S. S. Rao. *Mechanical Vibrations*. Prentice Hall, 5th edition, 2011. ISBN: 9780132128193.

[12] E. Albano and W. P. Rodden. A doublet-lattice method for calculating the lift distributions on oscillating surfaces in subsonic flows. *AIAA Journal*, 7(2):279–285, Feb. 1969.

[13] R. M. Botez, A. Doin, D. E. Biskri, I. Cotoi, D. Hamza, and P. Parvu. Method for flutter aeroservoelastic open loop analysis. *Canadian aeronautics and space journal*, 49(4):179–190, Dec. 2003. DOI: 10.5589/q03-016.

[14] J. Qiu and Q. Sun. Flutter solution by use of eigenvalues and eigenvectors of a complex general matrix. *Modern Applied Science*, 3(10), Oct. 2009. DOI: 10.5539/mas.v3n10p42.

[15] J. D. Anderson, J. Degroote, G. Degrez, E. Dick, R. Grundmann, and J. Vierandeels. *Computational Fluid Dynamics An Introduction*. Springer, 3rd edition, 2009. ISBN: 9783540850557.

[16] I. Kroo. *AA 241b Aircraft Design: Synthesis and Analysis*. Course Notes. Stanford University, USA, 2004.

[17] J. Katz and A. Plotkin. *Low-Speed Aerodynamics*. Cambridge University Press, New York, 2nd edition, 2001. ISBN: 9780521662192.

[18] C. Hirsch. *Numerical Computation of Internal and External Flows*, volume 1 of *Fundamentals of Computational Fluid Dynamics*. Elsevier, New York, 2nd edition, 2007. ISBN: 0750665947.

[19] A. S. Cardeira. Aeroelastic analysis of aircraft wings. *Instituto Superior Técnico (IST)*, Dec. 2014. MSc dissertation.

[20] *MATLAB® Primer*. The MathWorks, Inc., 25th edition, Sept. 2015.

[21] J. M. R. D. C. Baltazar. On the modelling of the potential flow about wings and marine propellers using a boundary element method. *Instituto Superior Técnico (IST)*, 2008. PhD dissertation.

[22] J. N. Reddy. *An Introduction To The Finite Element Method*. McGraw-Hill Series in Mechanical Engineering. McGraw-Hill, 3rd edition, 2006. ISBN: 0072466855.

[23] ANSYS,Inc. *Theory Reference for the Mechanical APDL and Mechanical Applications*. SAS IP,Inc., release 12.0 edition, 2009.

[24] A. T. Beck and C. R. A. da Silva Jr. Timoshenko versus euler beam theory: Pitfalls of a deterministic approach. *Structural Safety*, 33(1):19–25, Jan. 2011. DOI: 10.1016/j.strusafe.2010.04.006.

[25] R. D. Cook, D. S. Malkus, M. E. Plesha, and R. J. Witt. *Concepts and Applications of Finite Element Analysis*. John Wiley & Sons. Inc, 4th edition, 2002. ISBN: 0471356050.

[26] R. D. Cook. *Finite Element Modeling for Stress Analysis*. John Wiley & Sons, Ltd., 1st edition, 1995. ISBN: 0471107743.

[27] Y. W. Kwon and H. Bang. *The Finite Element Method using MATLAB*. CRC Mechanical Engineering Series. CRC Press, USA, 1st edition, 1997. ISBN: 0849300967.

[28] K.-J. Bathe. *Finite Element Procedures*. Prentice Hall, USA, 1st edition, 1996. ISBN: 0133014584.

[29] M. J. Patil, D. H. Hodges, and C. E. S. Cesnik. Nonlinear aeroelasticity and flight dynamics of high-altitude long-endurance aircraft. *Journal of Aircraft*, 38(1):88–94, 2001. DOI: 10.2514/2.2738.

[30] L. Wang, X. Liu, L. Guo, N. Renevier, and M. Stables. A mathematical model for calculating cross-sectional properties of modern wind turbine composite blades. *Renewable Energy*, 64:52–60, Apr. 2014. DOI: 10.1016/j.renene.2013.10.046.

[31] F. P. Beer, E. R. Johnston Jr., J. T. DeWolf, and D. F. Mazurek. *Mechanics of Materials*. McGraw-Hill, 6th edition, 2012. ISBN: 9780073380285.

[32] Y. Bazilevs, K. Takizawa, and T. E. Tezduyar. *Computational Fluid-Structure Interaction: Methods and Applications*. Wiley Series in Computational Mechanics. John Wiley & Sons, Ltd., UK, 1st edition, 2013. ISBN: 9780470978771.

[33] C. Farhat and M. Lesoinne. Two efficient staggered algorithms for the serial and parallel solution of three–dimensional nonlinear transient aeroelastic problems. *Computer Methods in Applied Mechanics and Engineering*, 182(3-4):499–515, 2000. DOI: 10.1016/S0045-7825(99)00206-6.

[34] R. Kamakoti and W. Shyy. Fluid-structure interaction for aeroelastic applications. *Progress in Aerospace Sciences*, 40(8):535–558, 2004. DOI: 10.1016/j.paerosci.2005.01.001.

[35] S. Piperno. *Simulation numérique de phénomènes d'interaction fluide-structure*. Mathematics, Ecole des Ponts ParisTech, France, 1995. PhD dissertation.

[36] M. Lesoinne and C. Farhat. Geometric conservation laws for flow problems with moving boundaries, and deformable meshes and their impact on aeroelastic computations. *Computer Methods in Applied Mechanics and Engineering*, 134(1-2):71–90, 1996. DOI: 10.1016/0045-7825(96)01028-6.

[37] M. Lesoinne and C. Farhat. Higher-order subiteration-free staggered algorithm for nonlinear transient aeroelastic problems. *AIAA Journal*, 36(9):1754–1757, 1998. DOI: 10.2514/2.7555.

[38] S. Piperno and C. Farhat. Partitioned procedures for the transient solution of coupled aeroelas- tic problems – part ii: energy transfer analysis and three-dimensional applications. *Computer Methods in Applied Mechanics and Engineering*, 190(24-25):3147–3170, 2001. DOI: 10.1016/S0045-7825(00)00386-8.

[39] D. Dorde. Generalized lagrange-d'alembert principle. *Publications de l'Institut Mathematique*, 91 (105):49–58, 2012. DOI: 10.2298/PIM1205049D.

[40] M. J. Patil and D. H. Hodges. On the importance of aerodynamic and structural geometrical nonlinearities in aeroelastic behavior of high-aspect-ratio wings. *Journal of Fluid and Structures*, 19(7): 905–915, Aug. 2004. DOI: 10.1016/j.jfluidstructs.2004.04.012.

[41] T. C. Corke. *Design of Aircraft*. Prentice Hall, 1st edition, Nov. 2002. ISBN: 0130892343.

[42] R. Whitford. *Design for Air Combat*. Jane's Publishing Inc., New York, USA, 1st edition, 1987. ISBN: 0710604262.

[43] J. A. Snyman. *Practical Mathematical Optimization: An Introduction to Basic Optimization Theory and Classical and New Gradient-Based Algorithms*, volume 97 of *Applied Optimization*. Springer, New York, USA, 2005. ISBN: 038729824X.

[44] *fmincon*. The Mathworks, Inc. http://www.mathworks.com/help/optim/ug/fmincon.html, accessed on August 2015.

Appendix A

Input Parameters Description

A.1 Wing Geometric Data

Table A.1 describes the required input data to obtain the wing external configuration.

Parameter	Description	Units
alpha	Wing angle of attack. This represents the orientation of the free stream velocity with relation to the global coordinate system. A positive value produces two positive components of the velocity pointing in the direction of the *x* and *z* axes.	$^\circ$
b	Full wing span, measured from the left wing's tip to right wing's tip.	m
croot	Chord length at the root. Combined with *ctip* to create an uniform taper of the wing.	m
ctip	Chord length at the tip. Combined with *croot* to create a constant taper angle.	m
xtip	Displacement of wing tip in the *x* direction of the global coordinate system. Used to create a constant sweep angle.	m
ztip	Displacement of wing tip in the *z* direction of the global coordinate system. Used to create a constant dihedral angle.	m
aerotwist	Vector of data containing the aerodynamic pre-twist of each cross section ($\theta_{pretwist}$ in Eq. (4.29)). A positive value produces a positive right-handed rotation about the elastic axis (the x-axis of the beam coordinate system).	$^\circ$

Table A.1: Wing geometric parameters.

A.2 Airfoil Shape Data

Table A.2 describes the required input parameters to obtain the airfoil shape.

A.3 Material Properties Data

Table A.3 describes the required material properties.

Parameter	Description
afFile	The name of the file that contains the coordinates of the airfoil's nodes. Two separate files exist with the same name, one for the fluid solver and one for the structural solver. In the first, the node ordering begins at the first node just under the trailing edge, moves over the lower surface, reaches the leading edge, moves over the upper surface, and terminates at the last node just above the trailing edge, which is open. In the second, the node ordering begins at the leading edge, moves over the upper surface, reaches the trailing edge, moves over the lower surface, and terminates at the last node just below the leading edge. In this case, the airfoil is closed.
Xnode	This column of data defines the x-coordinate of the airfoil shape with respect to the airfoil reference coordinate system. This coordinate is normalized by the chord length, having a maximum permissible value of 1.
Ynode	This column of data defines the y-coordinate of the airfoil shape with respect to the airfoil reference coordinate system. This coordinate is normalized by the chord length, having a maximum permissible value of 1.

Table A.2: Airfoil shape input parameters.

Parameter	Description	Units
MatID	Material identification number.	—
E	Young's modulus of the material.	Pa
G	Shear modulus of the material.	Pa
nu	Poisson's ratio of the material.	—
rho	Density of the material.	kg/m^3

Table A.3: Material properties parameters.

A.4 Internal Structure Data

Table A.4 describes the required input data to parametrize the internal structure of the wing.

Parameter	Description
thck_top	The thickness of the top surface of the wing. Units [m].
thck_bot	The thickness of the bottom surface of the wing. Units [m].
thck_web	A vector containing the thicknesses of the shear webs (spars) of the wing. Units [m].
mat_id_xxx	Material identification number, this number assigns a set of isotropic material properties to the specified "xxx" sector ("top", "bot" and "web") of the wing. This material identification number corresponds to the materials in the materials input data, described in the following section.
num_webs	The total number of shear webs (spars) within the wing. Each web is defined along a straight line between its inboard and outboard ends, and perpendicular to the chord line at each section. At least one shear web must be present.
inbStn	This vector contains the number of the wing cross section at which the inboard end of the spar is located.
inbStn	This vector contains the number of the wing cross section at which the outboard end of the spar is located.
inbChloc	This vector contains the chordwise location of the web at the inboard section. It is measured from the leading edge and is normalized by the chord length.
oubChloc	This vector contains the chordwise location of the web at the outboard section. It is measured from the leading edge and is normalized by the chord length.

Table A.4: Internal structure input parameters.

Appendix B

Reference Case Wing Modal Analysis

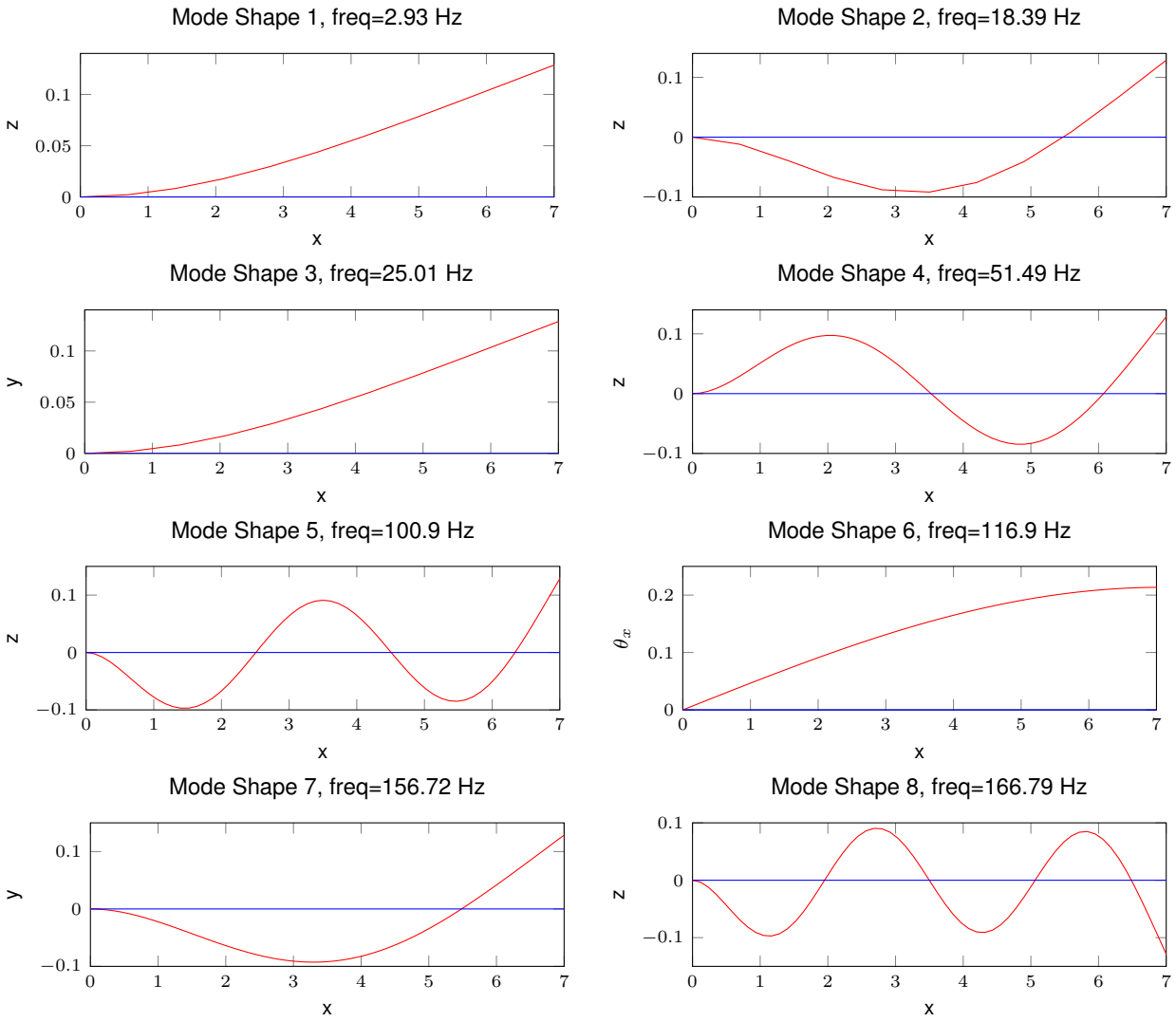

Figure B.1: Mode shapes for the reference case wing.